Multiscale Modeling and Analysis of Microtubule Self-Assembly Dynamics

A DISSERTATION
SUBMITTED TO THE FACULTY OF THE GRADUATE SCHOOL
OF THE UNIVERSITY OF MINNESOTA
BY

Brian Thomas Castle

IN PARTIAL FULFILLMENT OF THE REQUIREMENTS
FOR THE DEGREE OF
DOCTOR OF PHILOSOPHY

Adviser: David J. Odde

August 2014

Acknowledgements

I would like to thank my adviser, David J. Odde, for having the courage and patience to take on a student without an engineering background and for his continued support and encouragement throughout my graduate career. The opportunities he provided and entrusted in me have been invaluable. I cannot express enough appreciation for his infectious enthusiasm for science.

I also want to thank current and former Odde Lab members for their support, in particular, Dominique Seetapun whose mentorship provided the foundation for my graduate career and Joe Powers whose technical discussions and insight helped inform and challenge my thinking along the way.

Finally, thank you to my friends and family for your faith and support. No matter how big or how small, I am forever grateful for integral role you played in the completion of this work.

This dissertation is dedicated to my parents, Anne and Tom, whose unabated love and encouragement made completion of this work possible.

Abstract

Microtubules are dynamic biopolymers that self-assemble from individual subunits of αβ-tubulin. Self-assembly dynamics are characterized by stochastic switching between extended phases of growth and shortening, termed dynamic instability. Cellular processes, including the chromosome segregation during mitosis and the proper partitioning of intracellular proteins, are dependent on the dynamic nature of microtubule assembly, which facilitates rapid reorganization and efficient exploration of cellular volume. Microtubule-targeting chemotherapeutic agents, used to treat a wide range of cancer types, bind directly to tubulin subunits and suppress dynamic instability, ultimately impeding the capacity to complete cellular processes. Microscale length changes observed during dynamic instability are the net-effect of the addition and loss of individual subunits, dictated by the interdimer molecular interactions. Therefore, a multiscale approach is necessary to extrapolate submolecular level effects of microtubule-targeting agents to dynamic instability.

The work presented in this dissertation integrates multiscale computational modeling and experimental observations with the goal of better understanding the functional mechanisms of microtubule-targeting agents. First, we develop a computational model for the association and dissociation of tubulin subunits, in which the interdimer interaction potentials are specifically simulated. Simulation results indicate that the local polymer end structure sterically inhibits subunit association as much as an order of magnitude. Additionally, the model informs how microtubule-targeting agents could alter assembly dynamics through the properties of the interdimer interactions. Second, the mechanisms of kinetic stabilization by microtubule-targeting agents are tested and constrained by combining predictions from a computational model for microtubule self-assembly and experimental observations in mammalian cells. We find that assembly- and disassembly-promoting agents induce kinetic stabilization via separate mechanisms. One is a true kinetic stabilization, in which the kinetic rates of subunit addition and loss are

reduced 10- to 100-fold, while the other is a pseudo-kinetic stabilization, dependent upon mass action of tubulin subunits between polymer and solution. Overall, this work advances our knowledge of the basic physical principles underlying multistranded polymer self-assembly and can inform the future design and development of more effective and tolerable microtubule-targeting drugs.

Table of Contents

List of Tables

List of Figures

List of Abbreviations

EB1	End binding protein 1
EGFP	Green fluorescent protein
FRAP	Fluorescence recovery after photobleaching
GDP	Guanosine diphosphate
GTP	Guanosine triphosphate
GMPCPP	Guanylyl-(α,β)-methylene-diphosphate
MAP	Microtubule-associated protein
MMC	Metropolis Monte Carlo
MT	Microtubule
PF	Protofilament
SEM	Standard error of the mean
Tub	Tubulin

CHAPTER 1

General Introduction

1.1 Microtubule structure and assembly dynamics

Microtubules are dynamic intracellular polymers that serve as essential mediators of cellular processes such as cell division, intracellular transport, as well as cell polarization and migration. Individual subunits within the microtubule polymer, heterodimers of α- and β-tubulin, stack end-to-end in linear protofilaments, which interact laterally to form a cylindrical hollow tube. Self-assembly occurs via the addition and loss of subunits at the microtubule plus-end (β-tubulin facing out) in a dynamic process termed dynamic instability, which is characterized by the stochastic switching between extended periods of growth and shortening [1]. Microtubule catastrophe is defined as the switch from growth to shortening, while rescue is the reverse back to growth. Dynamic instability is a non-equilibrium process, driven by GTP hydrolysis [2]. Initially tubulin subunits have GTP bound to both α- and β-tubulin monomers. As subunits bind to and are subsequently buried within the microtubule lattice, GTP is hydrolyzed to GDP at the exchangeable GTP binding site on β-tubulin (E-site). E-site GDP is exchanged after dissociation, but remains bound while the subunit is in polymer. GDP-tubulin is less stable within the microtubule lattice, presumably due to weaker intersubunit interactions. Thus, the assembly state, growing or shortening, of a microtubule corresponds to the presence or absence, respectively, of a stabilizing cap of GTP-tubulin at the plus-end [3].

In addition to the nucleotide state, structural elements also correlate with growth and shortening. During growth, a subset of protofilaments extend out from the complete tube in gently outward-curling extensions [4], referred to as tip taper, in which protofilaments are gradually lost out to the end [5, 6]. The evolution of tip

taper, as subunits are added and lost at the end, correlates with and leads to history-dependent catastrophe [6–8]. In shortening microtubules, individual protofilaments are observed to peel away from the microtubule lattice in rams-horn structures [4, 9, 10]. This observation led to the hypothesis that the energy of GTP hydrolysis is stored in the lattice as mechanical strain, due to constraining GDP-tubulin away from its preferred curled orientation in order to comply with the straight conformation of the microtubule lattice [2, 3]. This strain will perturb the interdimer interactions, causing GDP-tubulin to be less stable and thus rapidly disassemble.

Due to the cylindrical nature of microtubule structure, αβ-tubulin subunits interact both laterally and longitudinally with adjacent subunits. In a B-lattice (that most commonly observed), the majority of lateral contacts are between homologous subunits, i.e. α-α and β-β, except at the seam where α-β contacts are made. Intersubunit interactions are non-covalent, primarily hydrophobic, with some electrostatic contributions to lateral interactions. A flexible loop between S7 and H9 on β-tubulin, referred to as the M-loop, interacts with loop H1-S2 and helix H3 on the adjacent subunit to make up the majority of the lateral contact [11, 12]. Three, primarily hydrophobic, zones surrounding the E-site establish the longitudinal interdimer contact. Because GTP-tubulin is exposed at the β-tubulin end, hydrolysis is assumed to be polymerization driven, only occurring after an additional subunit binds longitudinally [11, 13].

A wide range of intracellular microtubule-associated proteins (MAPs) have been shown to bind to the microtubule lattice and alter assembly dynamics (reviewed in 14). These include proteins that affect both growth and shortening, such as XMAP215 [15, 16] and tau [17], as well as those that promote catastrophe, such as end-binding proteins (EBs) [16], kinesin motors [7]. For the most part, MAPs enhance microtubule dynamics and likely explain the observation of increased rates *in vivo* compared to *in vitro*. In contrast, microtubule-targeting drugs, a diverse group of compounds binding directly to tubulin and used in various

chemotherapeutic regimens, attenuate dynamic instability [18]. As both MAPs and microtubule-targeting agents bind directly to tubulin heterodimers, their effects on polymer assembly are necessarily due to primary effects on the interdimer interactions.

1.2 Microtubule-targeting chemotherapeutic agents

Microtubule-targeting agents, which include both natural compounds and synthetic derivatives, have been a prominent and successful treatment option for various types of cancer since the original clinical approval of Taxol™ (paclitaxel) in 1992. This success stems from the essential role of microtubules in cellular processes, such as division, polarization, and migration, which are hyperactive in cancer cells [18]. Additionally, microtubule-targeting agents have been used in drug eluting stents to prevent restenosis and their efficacy in promoting axon regeneration to reduce spinal cord injury [19, 20] as well as potential for the treatment of neurodegenerative diseases [21] has been explored.

As dynamic microtubules function in both mitotic and interphase cells, the side effects of microtubule-targeting agents are relatively frequent and often dose limiting. Most commonly, peripheral neuropathies occur after treatment with microtubule-targeting agents [22, 23], indicating nerve cells are particularly susceptible. This is most likely explained by the abundance of tubulin in neurons as well as the importance of microtubules in establishing and maintaining neuronal processes and connections. Additional side effects of bone marrow suppression and flu-like symptoms have also been noted [24].

Microtubule-targeting agents bind directly to individual αβ-tubulin heterodimers at three primary sites, which correlate with their effect on polymer assembly. For the most part, disassembly-promoters bind to either the colchicine site at the intradimer interface between α- and β-tubulin monomers [25] or the vinca domain at the terminal end of β-tubulin near the E-site [26]. Microtubule assembly-promoters bind to the taxane pocket, adjacent to the M-loop on β-tubulin [11, 27].

This categorical assignment is a bit misleading, however, as the effectiveness of all microtubule-targeting agents ultimately depends on the capability to inhibit microtubule dynamic instability, thereby eliminating cells' capacity to complete essential processes. The loss of dynamic instability, referred to as "kinetic stabilization," is a culmination of the primary effects on individual subunit kinetics and thermodynamics at the molecular level.

Despite wide clinical use and years of study, not only do the molecular mechanisms of kinetic stabilization remain unclear and contentious, but additionally the proposed mechanisms have not been shown to in fact inhibit microtubule dynamic instability. The work presented here takes a multi-scale approach to study microtubule assembly dynamics with the over-arching goal of better understanding the molecular mechanism of kinetic stabilization implemented by microtubule-targeting chemotherapeutic drugs. Ideally, the knowledge gained will not only inform the basic biophysics of self-assembly dynamics but also the design and development of chemotherapeutic agents with higher efficacy and greater tolerance.

1.3 Models of microtubule assembly dynamics

Computational modeling is a useful tool for analyzing results and predictions as well as hypothesis testing in cell biology, where systems are often complex. By integrating hypotheses and assumptions, models not only aid in understanding a set of experimental results, but can also be used to predict and design future experiments that will result in the most significant conclusions.

Thus far, computational models of tubulin and microtubule dynamics have ranged from the atomistic level, molecular dynamics simulations of single tubulin subunits [28–32], to single microtubule level addition-loss of individual subunits [33–38], to cell level dynamic instability of a microtubule population [39, 40]. Molecular dynamics simulations have provided insight into how residues involved in establishing lateral and longitudinal contacts are altered in the presence of the microtubule-targeting agent paclitaxel [28], as well as different nucleotides (GTP,

GDP-P_i, and GDP) [29, 31]. Computational models of individual subunit addition and loss have informed estimates of the GTP cap size [36, 41, 42], the mechanisms of catastrophe and rescue [6, 35], as well as estimates of the strength of interdimer contacts that are consistent with experimental observations of dynamic instability [33, 34]. At each increasing level of scale, assumptions are made to coarse-grain aspects of the underlying dynamics that may not be practical for studying the process in question. Because of this, it is often difficult to understand how the results and predictions at one scale translate to another.

In Chapter 2, a new model for tubulin subunit association and dissociation is described, where the translational and rotational dynamics, along with the interaction potentials of individual subunits are explicitly simulated. This model provides a bridge between atomistic and simple addition-loss computational methods in linear polymer self-assembly. The model described provides a framework to study how the effects on interdimer interactions induced by microtubule-targeting agents will alter the kinetics and thermodynamics of subunit addition and loss. Additionally, the model provides insight into the implications of microtubule tip structure on the association and dissociation of tubulin subunits binding to the microtubule plus-end.

Most recently, computational modeling of microtubule assembly dynamics have shown that the relevant timescale for addition and loss of individual subunits is on the order of milliseconds [5], more than an order of magnitude faster than previously estimated by classic polymer assembly theory [4, 17, 43–46]. Therefore, the majority of our current knowledge of microtubule assembly dynamics has been limited to secondary dynamics averaged over thousands of relevant addition-loss events. This conclusion is based on the high variability of microtubule growth observed experimentally, which cannot be explained by previous estimates of the kinetic rates. Further it showed that assembly variability is indicative of underlying rate constants and can predict how microtubule assembly will respond when the respective rates are affected by microtubule-targeting agents and microtubule-

associated proteins (MAPs). This insight to the millisecond-scale dynamics of microtubules was a major revision within the field, and its implications in live cells as well as the mechanisms of microtubule-targeting drugs remains to be explored.

In Chapter 3, a model for microtubule assembly, at the level of individual subunit addition and loss, is used to investigate the mechanisms of microtubule-targeting agents, specifically how they lead to apparent kinetic stabilization of microtubules. The model employed in this study has been shown to reproduce microtubule growth and shortening rates [33], tip structures [6, 34], as well as the rapid nanoscale assembly dynamics observed *in vitro* [5, 41]. Therefore, it accurately represents multiple aspects of microtubule dynamic instability that are most likely influenced by microtubule-targeting agents. By better characterizing the theoretical requirements for dynamic instability, we can gain insight into how microtubule-targeting agents eliminate it, promoting kinetic stabilization. Integration of model predictions with *in vivo* experimental results in the presence of an assembly-promoter (paclitaxel) and a disassembly-promoter (vinblastine) indicates that there are two mechanisms by which kinetic stabilization is attained.

1.4 Quantitative analysis of microtubule dynamics and end structure

The kinetics of subunit addition and loss at the microtubule plus-end dictate the resulting length displacements during assembly as well as influence individual protofilament length variability [5, 41]. Microtubule tip structure is additionally influenced by the relative strengths of the lateral and longitudinal interactions [34]. Further, resulting tip structures feedback to influence subunit dissociation rates as well as microtubule catastrophe [5, 6]. Therefore, the incremental microtubule length displacements and tip structure, as well as the correlation of the two together, provide insight into the underlying kinetics and thermodynamics of individual tubulin subunits and will be integral in understanding the mechanisms of microtubule-targeting agents.

Light microscopy has been, and continues to be, the dominant approach in observing single microtubule assembly dynamics. Transmitted light microscopy, combined with video processing to enhance image contrast, facilitated the earliest estimates of dynamic instability parameters as well as estimates of the kinetic rates of tubulin subunit addition and loss [44, 47]. Since then, the development of sensitive digital cameras as well as fluorescent fusion proteins has made fluorescence microscopy the preferred approach for both purified *in vitro* assays and in live cells. Dynamic microtubule ends were initially tracked manually, where the tip position is estimated by eye. Estimates of tracking accuracy by this method are ~150-160nm [48, 49], much larger than the 8nm of a single tubulin subunit. *In vitro* optical tweezers methods, in which a microtubule conjugated to an optical bead grows against a microfabricated barrier, provide high spatial and temporal resolution [41, 50], however, are technically difficult and not applicable to living cells. Cryo-electron microscopy has been the primary approach utilized to observe the structure of growing and shortening microtubules [4, 9, 10], however, direct comparison of assembly dynamics and structure is not feasible by this approach.

Recently, the development of a semi-automated algorithm for tracking the ends of fluorescently tagged microtubules was shown to attain single time point accuracy of 10-12nm *in vitro* and ~36nm *in vivo*, for images collected at around 1Hz [5, 51, 52]. Via fitting an error function to the fluorescence intensity along the microtubule axis, it is possible to simultaneously collect information about the microtubule tip position and tip structure [51] and resulting tip quantifications correlate with observations by electron microscopy [6]. Combining this experimental approach with computational simulations provides a powerful method for quantitatively comparing model predictions to experimental estimates of microtubule assembly dynamics and tip structure. In Chapter 3, this approach is utilized to test and constrain the mechanisms of microtubule-targeting agents *in vivo*.

CHAPTER 2

Brownian dynamics of subunit addition-loss kinetics and thermodynamics in linear polymer self-assembly

(Reprinted with permission from *Biophysical Journal* 105(11), 2013)

2.1 Chapter Abstract

The structure and free energy of multi-stranded linear polymer ends evolve as individual subunits are added and lost. Thus, the energetic state of the polymer end is not constant, as assembly theory has assumed. Here we utilize a Brownian dynamics approach to simulate the addition and loss of individual subunits at the polymer tip. Using the microtubule as a primary example, we examined how the structure of the polymer tip dictates the rate at which units are added to and lost from individual protofilaments. We find that freely diffusing subunits arrive less frequently to lagging protofilaments but bind more efficiently, such that there is no kinetic difference between leading and lagging protofilaments within a tapered tip. However, local structure at the nanoscale has up to an order of magnitude effect on the rate of addition. Thus, the kinetic on-rate constant, integrated across the microtubule tip ($k_{on,MT}$), is an ensemble average of the varying individual protofilament on-rate constants ($k_{on,PF}$). Our findings have implications for both catastrophe and rescue of the dynamic microtubule end, and provide a sub-nanoscale framework for understanding the mechanism of action of microtubule-associate proteins and microtubule-directed drugs. While we utilize the specific example of the microtubule here, the findings are applicable to multi-stranded polymers generally.

2.2 Introduction

Linear biological polymers typically consist of homogenous globular protein subunits that interact non-covalently to form the functional structure. Examples of linear polymers are diverse and include members of the cytoskeleton, such as microtubules and actin filaments, as well as viruses, sickle-hemoglobin, and paired helical filaments. Because most interactions are non-covalent, both assembly and disassembly are reversible reactions that can be readily controlled and adapted. The adaptability of linear polymers such as microtubules and F-actin enables the congression and subsequent separation of chromosomes during mitosis as well as allows migratory cells to rapidly reorganize cellular protrusions in response to extracellular signals. Because of the importance of the linear polymer assembly dynamics in various cellular processes, they have been studied extensively for several decades both experimentally and theoretically.

Assembly theory for linear polymers assumes that the subunit association and dissociation rates are constant and equal for each strand [43]. This theory has been corroborated experimentally, fitting with the observed concentration dependent net-assembly rates for multi-stranded polymers such as F-actin [53], GTP-tubulin [1, 44], and GMPCPP-tubulin [15, 45], enabling estimates of the underlying kinetic rate constants. This model for assembly inherently assumes that the dynamic end of the polymer is energetically constant. However, the structure and free energy of the end evolve as a consequence of the formation and loss of lateral interactions as individual subunits are gained and lost from the end [54]. In the simplest form, single-stranded linear polymers have a single longitudinal interaction, however, the increasing complexity of multi-stranded polymers introduces lateral interactions between neighboring subunits (Figure 2.1A). Thus, despite fitting with experimental results, the assumptions of basic assembly theory break down for more complex multi-stranded polymers. This was recently shown in microtubule self-assembly where the off-rate ($k_{off,MT}$) increases as the majority of protofilament ends shift from more stable configurations to less stable configurations at higher free

tubulin concentrations [5]. Not only did these results have significant consequences for how we view microtubule self-assembly, but also demonstrate that kinetics vary as the structure of the microtubule tip evolves. Thus, the dissociation rate of tubulin subunits is not constant, as theory has assumed.

Hill indicated that both the on and off-rate will depend on the number of lateral interactions, however, concluded that the full effect would be on the off-rate for a diffusion-limited process [54]. In agreement, the majority of theoretical models for microtubule self-assembly have assumed a single on-rate constant ($k_{on,MT}$) for the microtubule end [33, 34, 36–38]. Gardner et al. [5], however, found that an on-rate penalty ($k_{on,PF2} = k_{on,PF}/\delta$, where $\delta = 15$) to protofilaments with two neighboring protofilaments of greater length, although not necessary to qualitatively match tip taper trends with free tubulin concentration, was necessary to quantitatively match the model-predicted protofilament length variance to that estimated experimentally. Without this penalty, the model predicted a protofilament length variance that is smaller than experimentally observed, meaning all protofilaments are of about equal length. This suggests that the evolving tip structure and free energy may affect the on-rate constant in addition to the off-rate and that kinetic or thermodynamic inequality at the microtubule end may be necessary to produce the experimentally observed structures [4, 51]. More generally, multistranded self-assembled polymers could, in principle, have different on-rate constants for each protofilament, however we currently lack the theoretical underpinnings for on-rate heterogeneity, or whether it is expected to even exist.

To explain the specific case of microtubule tip structure and self-assembly, Gardner et al. imposed an on-rate penalty only to protofilaments with two neighboring protofilaments of greater length and ignored any penalty imposed by a single neighboring protofilament. Even so, a single neighbor may be sufficient to hinder subunit incorporation into the lattice. As the microtubule grows, the tip becomes increasingly tapered [4, 6], in which the one-neighbor case will be the most frequent. Thus, a one-neighbor penalty could significantly influence net

assembly and the resulting structure of the microtubule tip, as well as influence assembly in multi-stranded linear polymers generally. Gardner et al. assumed the presence of neighboring protofilaments is unfavorable due to the steric hindrance of aligning incoming units with the orientation of adjacent protofilaments, however, the presence of neighboring protofilaments could also be favorable due to the additional free energy of forming lateral bonds. Thus, the net-effect of laterally interacting protofilaments at the end of linear polymers is not clear.

In addition to local effects of neighboring protofilaments, "global" structure or the distribution of protofilament lengths at the end of the microtubule could influence the kinetics of individual protofilaments, independent of the local conditions. Individual protofilaments vary in length within a microtubule, this is often referred to as tip "taper" or "raggedness," and often range up to several hundred nanometers both *in vitro* [4] and *in vivo* [51]. The tip structures in many cases appear much like the tip of a syringe needle (i.e. like a cylinder cut obliquely, see e.g. Chretien et al. Figure 4). The extended leading protofilaments potentially block freely diffusing subunits from reaching shorter lagging protofilaments, thus the rate by which free subunits arrive to a potential binding site could depend upon its global position within the microtubule tip structure.

To investigate the impact of polymer end structure on kinetics and thermodynamics of linear polymer self-assembly generally, we created a Brownian dynamics computational model for the non-covalent interactions of subunits with the polymer tip. This allowed us to simulate the association and dissociation of individual subunits, using microtubule assembly as a central focus. We found that due to counteracting effects, "global" structure of the extending tip does not affect the association rate to lagging protofilaments compared to leading protofilaments, assuming there are no lateral neighbors. However, local presence of either one or two neighboring protofilaments inhibits the association despite the presence of short-range favorable interactions. These results demonstrate that the association rate constant for the microtubule ($k_{\mathrm{on,MT}}$) should be considered an ensemble average

of the individual nanoscale rate constants of individual protofilaments ($k_{on,PF}$), which are dependent on the number of lateral interactions at the polymer end and evolve with the gain and loss of individual subunits. Additionally, our model serves as a framework to study the specific mechanisms by which microtubule-associated proteins and microtubule-targeting drugs affect the microscale microtubule dynamics through alteration of the underlying kinetics and thermodynamics. To our knowledge, this is the first intermediate scale simulation of subunit association and dissociation in linear filament self-assembly where the translational and rotational dynamics of subunits are explicitly simulated along with the interaction potentials between subunits. This modeling approach, based on the method articulated by Northrup and Erickson [55], provides a bridge from atomistic methods [28–32] and simple addition-loss methods [33–37, 40].

2.3 Model description and justification

Our model was based on the Brownian dynamics approach described by Northrup and Erickson [55] for estimating kinetic association rate constants, with the following modifications: 1) non-spherical subunit structure, 2) interaction with a self-assembled polymer lattice, and 3) separate near- and far-field simulations to isolate effects on either diffusion-limited arrivals or binding. Additionally, we implement a modified Metropolis Monte Carlo [56] algorithm for Brownian dynamics in the presence of an external force. All simulations were carried out with custom code written in MATLAB (The Mathworks Inc., Natick MA). To test the model predictions, we implemented two specific linear self-assembled polymer structures: microtubules and actin filaments. Simulated structures and interactions are described below. For a detailed description of the simulation procedure, see section 2.3.4.

2.3.1 Microtubule simulation structures

The microtubule structure was modeled as a B-lattice, consisting of 13 protofilaments and a helical pitch of 1½ dimers per turn (Figure 2.1A). Individual tubulin subunits were modeled as super-ellipsoids, obtained by rotating the Lamé curve

$$\left|\frac{x}{a}\right|^n + \left|\frac{y}{b}\right|^n = 1, \tag{2.1}$$

with a = 2 nm, b = 4 nm, and n = 5, about the vertical axis (Figure 2.1B). For a blunt tip, each protofilament consisted of 100 dimers to capture any potential long-range effects and to create variable tip structures through the removal of dimers from the lattice. To create a tapered tip, the first protofilament was 100 dimers in length and dimer number decreased linearly between protofilaments one and ten, which was of equal length to protofilaments 11-13 (Figure 2.1C). Protofilament 11 was then used as the protofilament of interest for simulations of lagging protofilaments to insure that immediately adjacent protofilaments were of equal length. Lag distance was defined as the center-to-center distance between the subunit of interest and either the most distal subunit (when lagging, positive lag distance) or the closest subunit on a separate protofilament (when leading, negative lag distance). In simulations where the protofilaments adjacent to the protofilament of interest were of greater length (lateral neighbors), protofilament seven of a blunt end was used and subunits were then added to one or both of protofilaments six and eight to create the one and two neighbor cases, respectively. We define the tolerance of lateral neighbors as the minimum distance (surface-to-surface) between adjacent subunits within the microtubule lattice (Figure 2.1B). Modifying the radius of the microtubule and keeping the dimensions of individual subunits constant adjusted tolerance.

2.3.2 Longitudinal and lateral interactions between subunits

To represent the longitudinal bonds between freely diffusing subunits and the protofilament of interest, we used three zones based on the high-resolution description of tubulin subunits within the microtubule lattice [11] (Figure 2.1B). Three zones is the minimum number necessary for correct rotational orientation to allow for lateral interactions and is the number of contacts that best matched experimental estimates of kinetic association rates according to [55]. The three zones (*A, B,* and *C*) were placed non-collinearly in a plane (i.e. in a triangle), tangential to the end of the subunit, normal to and centered on the subunit long axis on both the α- and β-tubulin ends of the dimer (Figure 2.1B). Zones were paired, and mutually exclusive, such that zone *A* of α-tubulin could only bind with zone *A* of β-tubulin on the subunit of interest. Zones were rotated about the vertical (long) axis so that their position relative to the inside or outside of the microtubule lattice was independent of protofilament number (e.g. Zone *A*, red, is always located near the inside face of the microtubule, as in Figure 2.1C).

Two zones, one α and one β, were used to model the lateral bonds between subunits (Figure 2.1B), which was sufficient to ensure that subunits were aligned vertically with neighboring protofilaments. Similar to longitudinal bonds, lateral zones were paired and mutually exclusive. Because of the helical and cylindrical shape of the microtubule lattice, lateral zones were offset from center on either side of the tubulin subunit and rotated inward toward the microtubule lumen (Figure 2.1B). Accounting for both the helical pitch and cylindrical shape of the microtubule lattice minimized the distance between lateral zones when a subunit was bound within the lattice.

Bonds were modeled as Hookean springs of zero rest length with a well depth equal to the total bond energy for an individual zone (Figure 2.1D). Thus, the energy at each time point was the difference between the total potential energy and the displacement of stretching the spring, given by the harmonic potential

$$U_{\mathrm{i}}(t_{\mathrm{j}}) = \frac{1}{2} k_{\mathrm{bond,i}} (r_{\mathrm{i}}(t_{\mathrm{j}}))^2 + U_{\mathrm{bond,i}}, \tag{2.2}$$

where r_{i} is the distance between paired zones and $k_{\mathrm{bond,i}}$ is the spring constant of an individual interaction zone. Individual zones were modeled as springs in parallel and the total bond potential energy was evenly distributed across all zones, such that $k_{\mathrm{bond,i}} = k_{\mathrm{bond}}/q$ and $U_{\mathrm{bond,i}} = U_{\mathrm{bond}}/q$ (where $q = 3$ for the longitudinal bond and $q = 2$ for lateral bond). We assumed k_{long} was equal to that previously estimated for the longitudinal bond modeled as a harmonic potential ($k_{\mathrm{long}} \approx 900$ pN/nm) [34]. We initially established bounds for the total longitudinal bond potential energy (U_{long}) (see section 2.3.9), but later found that $U_{\mathrm{long}} = -20.4\ k_{\mathrm{B}}T$ resulted in $\Delta G^{0}_{\mathrm{long}} = -6.8\ k_{\mathrm{B}}T$ (see section 2.4.5), consistent with that previously estimated for the longitudinal bond free energy [33]. Therefore, this value of U_{long} was used for the longitudinal bond in all simulations unless otherwise noted.

Several studies have noted that the intrinsic bond energy of the lateral bond is weaker (more positive) than the longitudinal bond by ~12-16 $k_{\mathrm{B}}T$ [30, 33, 57]. To account for this difference, we assumed that the total bond energy for the lateral bond was one third that of the longitudinal bond ($U_{\mathrm{lat}} = -20.4/3\ k_{\mathrm{B}}T = -6.8\ k_{\mathrm{B}}T$), thus weakening the lateral bond by ~14 $k_{\mathrm{B}}T$. Additionally, the spring constant of the lateral bond was three-times softer than the longitudinal bond ($k_{\mathrm{lat}} = k_{\mathrm{long}}/3$) to account for the flexible M-loop involved in the lateral contact between tubulin subunits [11]. Softening the lateral bond also made the binding radius (r_{B}) equal for both the longitudinal and lateral bond. A bond was considered broken when the strain of stretching was greater than the total bond energy. This separation distance (where $U_{\mathrm{i}}(t_{\mathrm{j}}) = 0$) was defined as the binding radius (r_{B}) and given by

$$r_{\mathrm{B}} = \left(\frac{-2U_{\mathrm{bond,i}}}{k_{\mathrm{bond,i}}} \right)^{1/2}. \tag{2.3}$$

Based on the bond strengths and stiffness values indicated above, $r_{\mathrm{B}} = 0.43$ nm. Individual zones were considered bound when their separation distance was less

than the binding radius (Figure 2.1D) and only those zones that were bound contributed to the total energy at a given time point according to

$$U(t_j) = \sum_{i=1}^{N} U_i(t_j), \tag{2.4}$$

where N is the number of zones within r_B (the longitudinal and lateral zones both contribute to the value of N, such that max(N) = 3, 5, or 7 with zero, one, or two lateral bonds). A subunit was considered completely bound when all three zones constituting the longitudinal bond were within r_B (N = 3 for longitudinal bond).

2.3.3 Actin filaments

To simulate actin (instead of tubulin), we assumed G-actin monomers were super-ellipsoids with dimensions of 4 x 4 x 6.7 nm (a = 2 nm and b = 3.35 nm in equation 2.1), comparable to [58], and that the protofilaments of F-actin were offset by 2.8 nm [59]. Protofilaments were 100 subunits in length, and then subunits were added to the leading protofilament in order to increase the lag distance of the lagging protofilament. We found a total bond energy of U_{long} = -19.2 k_BT best fit estimates of the standard Gibbs free energy for the longitudinal bond [60]. Additionally, we adjusted the stiffness of the longitudinal bond based on previous estimates for ATP-actin (k_{long} = 165 k_BT/nm^2 ≈ 700 pN/nm) [58]. Modifying the total bond energy and bond stiffness only slightly changed the binding radius (r_B = 0.46 nm) compared to tubulin. To include the diagonal bonds between actin monomers, we used a single interaction zone per diagonal bond with U_{diag} = -6.4 k_BT and k_{diag} = k_{long}.

2.3.4 Simulation procedure

For all simulations we implemented the following procedure:

1. Initialize microtubule structure, as well as the starting position and orientation of the freely diffusing unit.
2. Translate and rotate the free unit.

3. Implement Metropolis Monte Carlo criterion based on the current and projected energetic states.
4. Check ending criteria for the given simulation (binding state or separation). If satisfied, continue to step 5 otherwise return to step 2.
5. Calculate the rate.

At each time step, subunits experienced a translational-rotational displacement described by

$$\mathbf{v} = (\Delta x_1', \Delta x_2', \Delta x_3', \phi_1, \phi_2, \phi_3), \tag{2.5}$$

where $\Delta x_1'$, $\Delta x_2'$, and $\Delta x_3'$ are translational displacements of the centroid position in the subunit body frame and ϕ_1, ϕ_2, and ϕ_3 are rotations of the body frame axes about the lab frame axes. Each translational displacement was sampled from a Gaussian distribution that obeys

$$\left\langle (\Delta x_k')^2 \right\rangle = 2D\Delta t \tag{2.6}$$

where D is the translational diffusion coefficient parallel ($D_{\parallel}$, for k=1) or perpendicular ($D_{\perp}$, for k=2,3) to the long axis of an ellipsoid [61] and Δt is the current time step. Similar distributions were used to generate rotational displacements with D replaced by the respective rotational diffusion coefficient for axial (D_a, for k=1) or non-axial rotation (D_r, for k=2,3). Centroid displacements in the body frame were translated to the lab frame as described by [62]. At each time point

$$\begin{bmatrix} \Delta x_1 \\ \Delta x_2 \\ \Delta x_3 \end{bmatrix} = \mathbf{M}(t_j) \cdot \begin{bmatrix} \Delta x_1' \\ \Delta x_2' \\ \Delta x_3' \end{bmatrix}, \tag{2.7}$$

where $\mathbf{M}(t_j)$ is a three-dimensional rotation matrix that defines the rotation of the body frame axes about each individual axis of the lab frame at the current time step. The matrix $\mathbf{M}(t_j)$ is updated after each accepted step using the random rotational displacements according to

$$\mathbf{M}(t_{j+1}) = \mathbf{M}(t_j) \cdot \mathbf{R}(\phi_1, \phi_2, \phi_3) = \mathbf{M}(t_j) \cdot \mathbf{R}_3 \cdot \mathbf{R}_2 \cdot \mathbf{R}_1, \tag{2.8}$$

where $\mathbf{R}_1$, $\mathbf{R}_2$, and $\mathbf{R}_3$ are the respective rotation matrices about each lab frame axis, for example

$$\mathbf{R}_1 = \begin{bmatrix} 1 & 0 & 0 \\ 0 & \cos(\phi_1) & -\sin(\phi_1) \\ 0 & \sin(\phi_1) & \cos(\phi_1) \end{bmatrix}. \tag{2.9}$$

To minimize the number of steps when a free unit was not near the microtubule lattice, we used a variable time step that was based on the separation distance between paired binding zones. At each time point, the time step was calculated from

$$\Delta t = \frac{1}{6D_{\|}} \left(\frac{d}{\lambda} \right)^2, \tag{2.10}$$

such that the root-mean-squared displacement for a given time step was less than the distance between interacting zones. In equation 2.10 above, d is defined as the minimum separation distance between corresponding interaction zones (d = min[$r_1(t_j)$, $r_2(t_j)$, $r_3(t_j)$]) unless $d < r_B$, then $d = r_B$, such that the min(Δt) > 1 ps. We used the diffusion coefficient along the long axis of the super-ellipsoid ($D_{\|}$) in equation 2.10, as this was the larger of the two translational diffusion coefficients in the body frame. An adjustable constant, λ, is used to scale the size and number of steps taken during the simulation. When subunits were far away from the lattice (> 100 nm) λ = 5, otherwise λ = 10 for all simulations. Using these values of λ ensured that energy changes of bound zones were relatively small (average $|\Delta U| <$ 1.0 $k_B T$) while still minimizing simulation time.

Before advancing to the next time point, attempted steps were either allowed or disallowed through implementation of Metropolis Monte Carlo [56], where P_{step} = min[1,exp(-$\Delta U/k_B T$)]. Here favorable steps ($\Delta U \leq 0$) are always allowed and unfavorable steps ($\Delta U > 0$) are accepted according to Boltzmann's law. When a freely diffusing subunit spatially overlaps the microtubule lattice, we assumed that

$\Delta U = \infty$ (such that $P_{step} = 0$) to implement hard sphere rejection criteria. In the case of a rejected step, time is advanced by Δt but the position and orientation of the diffusing unit does not change from the previous time point. While the implementation of a variable time step and sampling moves from a Gaussian random variable were modifications to previous versions of the Metropolis algorithm for protein dynamics [63, 64], we found that this algorithm converged to theoretical expectation both in the presence and absence of an external force (see section 2.3.8) while enabling faster simulation.

2.3.5 Estimating on-rate constants

To isolate potential effects on both diffusion-limited arrivals to the microtubule lattice and binding, we split simulations into two parts, far- and near-field. Rates for each simulation scale were calculated according to [55] as

$$k = \frac{k_D(R_{start})\beta}{1-(1-\beta)k_D(R_{start})/k_D(R_{end})}, \tag{2.11}$$

where $k_D(R)$ is the diffusion-limited rate of arrival to a center-to-center distance of R defined by

$$k_D(R) = 4\pi D_{avg} R \tag{2.12}$$

Here, D_{avg} is the average diffusion coefficient in three body axes of the ellipsoid from

$$D_{avg} = (2D_{\perp} + D_{\parallel})/3 \tag{2.13}$$

In far-field simulations (diffusion-limited arrivals), freely diffusing subunits are initiated by placement on a spherical surface of radius R_{start} = 400 nm and with a random orientation. Subunits are allowed to diffuse until reaching either R_{end} = 3200 nm (i.e. they diffused far away from the binding site and were highly unlikely to bind) or a center-to-center distance of 10 nm from the subunit of interest within the microtubule lattice (i.e. they diffused close to the binding site and were potentially capable of binding). Here, β in equation 2.11 is the fraction of diffusing units that reach 10 nm center-to-center before reaching R_{end}. Therefore, k is the

diffusion-limited arrival rate to a center-to-center distance of 10 nm ($k_D(R = 10$ nm)). The centroid positions of units that reach 10 nm are subsequently used as the starting positions to initiate the corresponding near-field simulations. In the near-field simulations R_{end} = 400 nm (value of R_{start} for far-field) and $k_D(R_{start})$ in equation 2.11 is replaced by the estimated value of $k_D(R = 10$ nm) from the corresponding far-field simulations. For near-field simulations, β is the fraction of subunits that completely bind, or meet the criteria that all individual zones (either longitudinal, lateral, or both) are within the binding radius ($r_i <= r_B$ for all values of i). equation 2.11 then gives the estimated association rate constant ($k_{on,PF}$) for binding to the protofilament of interest. For each binding site condition, we ran a total of 500,000 far-field and 200,000 near-field simulations, which required about 50 CPU hours/processor.

2.3.6 Defining a distance criterion for unbinding events

Defining when a subunit is unbound is not as straightforward as defining when it is bound. As seen in Figure 2.2A, freely diffusing subunits break all zone contacts ($N = 0$, $r_i > r_B$ for all i) multiple times before finally diffusing away from the microtubule lattice. This is because when a free unit first breaks all contacts, it is still highly correlated with its bound orientation, making the probability of rebinding very high. It is difficult to reason that this is a true unbinding event because the majority will immediately rebind (Figure 2.2). Thus, to more appropriately define an unbinding event we used a separation distance criterion, similar to [65], where the unbinding radius (R_U) is greater than the binding radius (r_B) (Note: we can not directly compare r_B and R_U, as r_B is an edge-to-edge distance and R_U is center-to-center). To determine this distance, we simulated completely bound subunits until they reached varying center-to-center separation distances (R) from their binding partner. The resulting centroid positions and subunit orientations were then used to initiate subsequent binding simulations to estimate the probability of rebinding. We define R_U as the distance where a free unit has a low probability

($p < 0.01$) of rebinding before diffusing away, R_U = 11 nm center-to-center in this case (Figure 2.2B). Using our distance criterion for unbinding, the distribution of unbinding times fits well with the expected single exponential ($p = 0.82$, Kolmogorov-Smirnov test) for a first-order rate (Figure 2.2C). Therefore, we reason that this distance criterion is a reasonable way to practically define when a freely diffusing subunit is unbound within the simulation.

We did not simulate complete unbinding events in the very stable condition where a subunit has a longitudinal bond and two lateral bonds, due to the expected duration of the interaction (from [33], $k_{off} = 0.05\ s^{-1}$ for $k_{on,PF} = 4\ \mu M^{-1}s^{-1}$). Alternatively, we set a limit for the unbinding time, τ, and looked at the number of successful unbinding events in that amount of time. The number of successes will obey a binomial distribution, with probability of success $p = k/n$ where k is the number of successes and n is the total number of simulations. Since the unbinding time is exponentially distributed (Figure 2.2C), the probability that an event occurs in $T <= \tau$ is $p = 1\text{-}e^{-\lambda\tau}$. From this we obtain $k/n = 1\text{-}e^{-\lambda\tau}$ and thus can estimate the rate, λ, from the number of successes and the cut-off time. Setting a limit of τ =1ms, we found that zero subunits successfully unbound for conditions with one longitudinal and two lateral bonds for both tubulin and actin. Therefore we set an upper limit on the off-rate by finding the maximum value of λ, such that the probability of observing zero success in n trials for the binomial $B(n, p = 1\text{-}e^{-\lambda\tau})$ was greater than 0.05.

2.3.7 Simulation of microtubule net assembly

Net assembly of individual microtubules was simulated according to [33] at 6.5 μM free tubulin concentration for three penalty conditions: without penalties, two-neighbor penalty only [5], and model estimated penalties for one and two lateral neighbors. Simulations in each condition were run for a total of 60 s of real-time and the resulting tip structures from the last 30s were examined at 1s intervals. A total of 16 runs were performed, resulting in 496 structures per condition. The

zero-neighbor on-rate constant ($k_{on,PF}$) was scaled in simulations with penalties such that the average microtubule on-rate constant ($k_{on,MT}$) was equal for all simulations. Additionally, we increased the strength of the longitudinal bond in simulations with penalties (more negative ΔG^0_{long}; -0.4 k_BT or -1.0 k_BT for simulations with only two-neighbor and with both penalties, respectively) such that the net assembly rate was equal in each condition. Resulting structures from each simulation condition were ordered by the standard deviation of protofilament lengths, then the lower and upper 10% were considered to be blunt and tapered for that condition, respectively. This parsing of the tip structures was performed for each condition individually in order to compare the fraction of protofilaments with zero, one, or two lateral neighbors in the blunt and tapered tips across simulation conditions.

2.3.8 Comparing the modified Metropolis Monte Carlo to previous methods

In the presence of an external force, our simulation approach is based on the Metropolis Monte Carlo [56] (MMC) method for protein dynamics. The MMC method is a solution for the diffusive Fokker-Plank equation

$$\frac{\partial p(x,t)}{\partial t} = D\frac{\partial^2 p(x,t)}{\partial x^2} - \frac{1}{\gamma}\frac{\partial}{\partial x}[F(x)p(x,t)] \qquad (2.14)$$

when molecule steps are sampled from a uniform distribution [$-r$,r], where r is small and held constant throughout the simulation [63, 64]. We implemented the following two modifications, which serve to improve algorithm efficiency without a substantial cost in accuracy (documented below): 1) steps were sampled from a Gaussian distribution instead of a uniform distribution, and 2) the time step varies throughout the simulation such that time steps are larger when the diffusing tubulin subunit is far from the binding site on the microtubule. Since our algorithm has been modified from the original MMC, we simulated a number of asymptotic cases that have analytical solutions to equation 2.14 to confirm that our modified MMC yields the correct solutions [63, 64].

Assuming a delta function initial condition $p(x,t = 0) = \delta(x\text{-}x_0)$ at $x_0 = 0$, solutions to equation 2.14 are well defined in both the presence and absence of an external force, and in each case converge to a Gaussian distribution

$$p(x,t) = \frac{1}{\sqrt{2\pi\sigma^2}} \exp\left[-\frac{(x-\mu)^2}{2\sigma^2}\right]. \tag{2.15}$$

In the absence of force, $\mu = 0$ and $\sigma^2 = 2Dt$, where D is the diffusion coefficient. In the presence of a constant external force, F, the force causes the molecule to move with constant velocity $v = F/\gamma$, where γ is the drag coefficient. This drift velocity is superimposed on the diffusive motion such that only the mean is affected and is given by $\mu = vt = (F/\gamma)t$. To test whether our simulation obeyed equation 2.14, we used our modified MMC to simulate molecular diffusion in one dimension with $D = D_{avg}$ (from equation 2.13) in the absence and presence of a constant external force F = 2 pN (Figure 2.3A and B). As shown in Figure 2.3A and B, our simulation results fit well with theoretical expectation (from equation 2.15) at multiple time scales and were comparable to those using previous MMC methods.

Since we assume the interaction potential between binding partners is harmonic, we further sought to examine whether our modified MMC algorithm agreed with expectation for diffusion in a harmonic potential, $U(x) = \frac{1}{2}kx^2$ where k is the spring constant. Assuming a delta function initial condition, as above, molecular motion obeys an Ornstein-Uhlenbeck process [66], in which the analytical solution to equation 2.14 is

$$p(x,t) = \left(\frac{k}{2\pi k_B T(1-\exp[-(2k/\gamma)t])}\right)^{1/2} \exp\left[-\left(\frac{k}{2k_B T}\right)\frac{\left(x - x_0\exp[-(k/\gamma)t]\right)^2}{\left(1-\exp[-(2k/\gamma)t]\right)}\right] \tag{2.16}$$

As shown in Figure 2.3B and C our modified MMC algorithm agrees with equation 2.16 in both cases where $x_0 = 0$ and $x_0 = 0.2$ nm using $k = k_{long,i}$. Comparing equation 2.16 to equation 2.15 we can see that in a harmonic potential the resulting distribution is also Gaussian, where the mean and variance are both a function of time

$$\mu(t) = x_0 \exp[-(k/\gamma)t] \tag{2.17}$$

$$\sigma^2(t) = \left(\frac{k_B T}{k}\right)\left(1 - \exp[-(2k/\gamma)t]\right) \tag{2.18}$$

As $t \to \infty$, equation 2.16 is equivalent to Boltzmann's law ($p \sim e^{-U/k_B T}$) for a harmonic with $U(x) = ½kx^2$

$$p(x, t \to \infty) = \left(\frac{k}{2\pi k_B T}\right)^{1/2} \exp\left[-\left(\frac{k}{2k_B T}\right)x^2\right]. \tag{2.19}$$

At steady-state, $\mu(t \to \infty) = 0$ and $\sigma^2(t \to \infty) = k_B T/k$, which is consistent with equipartition of energy. The mean and variance of particle position converge to steady-state with time constant $\tau = \gamma/k$ and $\tau = \gamma/(2k)$ for the mean and variance, respectively. By estimating the mean and variance of molecule positions as a function of time for the case where x_0 = 0.2 nm, we found that our modified MMC algorithm approached steady-state on the correct time scale (Figure 2.3D and E). As our algorithm agrees with theoretical expectation in various conditions of diffusion in the absence and presence of force and in steady-state and in unsteady-state, we conclude that it is a good approximation to the equations of diffusive motion.

While our results do not differ from previous methods, our modified MMC approach has several advantages over the previous methods. First, in sampling from a uniform distribution, multiple moves are required before the distribution converges to a Gaussian (via the central limit theorem), compared to our approach where moves for every time step are Gaussian distributed. Therefore, at short time scales (i.e. after few steps) our modified MMC should more accurately predict the expected molecule distribution. Other Brownian dynamics methods have sampled moves from a Gaussian, but assume that the force is constant for each step and therefore is implemented as a drift term [67]. Under the simulation conditions used here, we found that results using this method did not differ from our modified MMC (< 5% difference). The assumption that force is constant, however, would break

down for steep interaction potentials (i.e. stiff bonds), possibly resulting in quicker transitions to steady-state (equation 2.17 and 2.18) or quicker escape time from the potential well (unbinding). Additionally, when simulating few diffusing molecules of interest, our algorithm allows the mean squared step size to be scaled to the relative separation between molecules (equation 2.10), so that computational time is not wasted taking small steps ([-*r*,*r*]) while molecules are far away from their binding partner.

2.3.9 Establishing upper and lower bounds for the total longitudinal bond energy

Due to the way that we have modeled bond zone interactions, negative displacements away from the potential minimum ($x = 0$), which result in overlap of super-ellipsoid surfaces, are not allowed. Therefore, we can think of each bound zone as a thermally driven spring where only positive displacements are allowed. The intrinsic bond energy will be related to the total longitudinal bond energy (potential energy well-depth) by

$$U_{\text{long}} = \Delta G^0_{\text{B}} - 3U_{\text{i}}(\mu) \tag{2.20}$$

where $U_{\text{i}}(\mu)$ is the individual spring potential at the mean position, μ, and $\Delta G^0{}_{\text{B}}$ is the intrinsic bond strength of the longitudinal bond. If we consider the standard free energy of the longitudinal bond, $\Delta G^0{}_{\text{long}}$, as the difference between the favorable $\Delta G^0{}_{\text{B}}$ and unfavorable entropic penalty of binding, $\Delta G^0{}_{\text{S}}$, then we can substitute for $\Delta G^0{}_{\text{B}}$ in equation 2.20 to get

$$U_{\text{long}} = \Delta G^0_{\text{long}} - \Delta G^0_{\text{S}} - 3U_{\text{i}}(\mu) \tag{2.21}$$

The mean position of the constrained, thermally driven spring is

$$\mu = \int_0^\infty x \cdot f(x) \cdot dx = \frac{2}{\sqrt{2\pi\sigma^2}} \int_0^\infty x \cdot e^{-x^2/2\sigma^2} dx \,, \tag{2.22}$$

where the factor of two in the numerator is used to scale the area under the curve to unity. Integration of equation 2.22 results in a mean position of

$$\mu = \frac{2\sigma}{\sqrt{2\pi}} \tag{2.23}$$

If we assume that spring displacements have three degrees of freedom, then from equipartition of energy we get $\sigma^2 = 3k_BT/k_{long,i}$. Inserting this into equation 2.23, results in a mean position of

$$\mu = \left(\frac{6k_BT}{\pi k_{long,i}} \right)^{1/2} \tag{2.24}$$

and the energy at this position is

$$U_i(\mu) = \frac{1}{2} k_{long,i} \left(\frac{6k_BT}{\pi k_{long,i}} \right) = \frac{3k_BT}{\pi}. \tag{2.25}$$

Therefore, we assume an unfavorable contribution to U_{bond} of ~1 k_BT per interaction zone. Estimates of ΔG^0_S range from about 10-12 k_BT [57, 60, 68], therefore using ΔG^0_{long} = -6.8 k_BT from [33] we predict that U_{long} = -21.8-19.8 k_BT. As discussed in section 2.4.4, we find that U_{long} = -20.4 k_BT results in ΔG^0_{long} = -6.8 k_BT.

2.4 Results and Discussion

2.4.1 Global position has no net effect on kinetics

We anticipated two potential effects of global and local tip conditions, either reducing the rate at which freely diffusing tubulin subunits arrive (through diffusion) to a surface some short distance away from the protofilament of interest or inhibiting the subsequent binding. To isolate these two potential effects, we split our simulation into two parts (see section 2.3.5), first simulating the diffusion-limited arrival rate to a surface a short distance from the bound subunit of interest ($k_D(R)$, where R = 10 nm center-to-center; Figure 2.4A), and second, simulating the subsequent binding of units that arrived at this surface. As shown in Figure 2.4B, freely diffusing subunits approach lagging protofilaments at a slower rate compared to leading protofilaments. The arrival rate to leading protofilaments rapidly approaches the predicted Smoluchowski rate (equation 2.12), while the arrival rate

to lagging protofilaments is ~twofold slower. Interestingly, once a protofilament is leading or lagging by a certain distance (on the order of a single subunit layer), there is relatively little change in the rate (Figure 2.4B). The greatest change in rate occurs around zero lag, indicating that only small differences in the relative length of individual protofilaments are necessary to reduce the arrival frequency of freely diffusing subunits. This suggests that global structure would have similar implications in other multi-stranded polymers that exhibit less variation in protofilament lengths, such as F-actin.

To more specifically examine the cause of reduced arrivals to lagging protofilaments, we looked at the positions of arriving units (that reach the 10 nm center-to-center distance) relative to the subunit of interest within the microtubule lattice (Figure 2.4C and D). While there was no apparent spatial bias in the reduction of arrivals above or below the subunit of interest, we found that fewer subunits arrive to lagging protofilaments from the direction of the inside (lumen) of the microtubule compared to leading protofilaments (Figure 2.4D). This supports our original hypothesis that longer protofilaments shield lagging protofilaments, but the fact that the observed effect starts around ± 90° longitude further suggests that the observed effect is in part due to the neighboring protofilaments of nearly equal length. If adjacent protofilaments were the only effect on diffusion-limited arrivals, we expect there would be no difference between protofilaments 2-11 in a blunt tip, as the local conditions are equivalent for each. As seen in Figure 2.4B, however, protofilaments 2-11 (lag distance ~0-8 nm) exhibit the greatest absolute rate of change in arrival rate. These results together indicate that the global structure mainly reduces arrivals to lagging protofilaments by blocking the angles from which freely diffusing subunits can approach the binding site.

If the efficiency of binding is independent of the global tip structure, then our estimated on-rate constant for lagging protofilaments should be lower than that for leading protofilaments. As shown in Figure 2.5A, however, binding efficiency is not independent of the global position and exhibits the opposite trend compared to

arrivals. This means that freely diffusing dimers, once they have gotten to within a few nanometers of the binding site, are more likely to bind to lagging protofilaments than leading protofilaments. The observed trend in binding efficiency effectively cancels out the trend in diffusion-limited arrivals, such that the on-rate constant is independent of the global position of the binding site within the microtubule tip (Figure 2.5B). The same trend in binding efficiency was observed when starting positions were artificially randomized along the 10 nm surface rather than sampled from the diffusive arrivals (Figure 2.6). Therefore, the observed trend in binding efficiency was not due to bias in the starting positions but rather due to an inherent property of lagging versus leading protofilaments.

The fact that the trend is observed for each degree of contact specificity (N = 1, 2, and 3) indicates that the global structure does not promote the transition to a higher degree of binding, but rather increases the chance that a single contact is established in the first place (Figure 2.5A). Note that the percentage of freely diffusing subunits that reach the N = 1 state is very small (2-3%), thus even though they arrive to a very short distance (10 nm surface) relative to the binding site, the vast majority of subunits diffuse away without ever interacting with the protofilament of interest. Subunits arriving above the binding site are more efficient for both leading and lagging protofilaments, however, those arriving from the direction of the microtubule lumen are about three times more efficient when binding to lagging versus leading (Figure 2.5C and D). Thus, even though fewer freely diffusing subunits reach lagging protofilaments from the direction of the inner part of the microtubule (Figure 2.4D), those units are more likely to interact with the protofilament of interest and eventually incorporate into the lattice. These results together suggest that the surrounding longer protofilaments in the lagging case keep free units from escaping, in the same manner that they blocked units from arriving in the first place, thus increasing the probability that the free unit establishes at least one interaction contact. Thus, the extending global tip structure is like a double-edged sword that simultaneously blocks subunit arrivals to and

departures from the vicinity of lagging protofilaments, such that leading and lagging protofilaments end up with essentially the same on-rate constant.

2.4.2 Local structure sterically inhibits subunit association

Although global structure did not affect subunit addition, we were interested to see whether local structure might, an effect invoked to quantitatively explain microtubule tip structure in a previous study [5]. In a multi-stranded self-assembled polymer, lateral interactions are formed and lost as a consequence of the gain and loss of individual subunits at the dynamic end of the microtubule, and thus the local conditions for a given protofilament will vary over time. For a multi-stranded polymer with at least three protofilaments, there are three conditions that an incoming subunit could encounter [54]. The protofilament of interest could have zero, one, or two neighboring protofilaments that are longer by at least one subunit. In contrast to global structures, the potential effects of local structures are more immediately apparent. For example, in the case with two adjacent longer protofilaments, an incoming unit would have less freedom of orientation due to the steric hindrance of the neighboring protofilaments. Based on these arguments, Gardner et al. implemented an on-rate penalty (15-fold decrease of the association rate constant, $k_{on,PF}$) to protofilaments with two neighboring protofilaments of greater length in order to replicate the experimentally observed protofilament length variance [5]. Here we sought to use our Brownian dynamics model to investigate whether a single neighboring protofilament of greater length could induce a similar penalty and to obtain a more rigorous estimate of what the two-neighbor penalty should be, if any.

We defined local tip structure as the relative lengths of an individual protofilament to its immediately adjacent neighboring protofilaments (Figure 2.1A). In our simulation, a blunt tip (zero lateral neighbors) assumes both neighboring protofilaments are the same length as the protofilament of interest. The one and two lateral neighbor cases are where one or two adjacent protofilaments, respectively,

are longer by at least a single dimer. As seen in Figure 2.7A, our estimated on-rate constant decreases progressively with the addition of one and two lateral neighbors. Thus, the on-rate constant for a protofilament in each condition will be penalized relative to the zero neighbor case. This observation was robust with respect to the details of the shape of the potential as well as the bond stiffness (see section 2.4.6, Figure 2.12). While we assume that all protofilaments are orientated parallel to the microtubule axis, the gentle outward curling of leading protofilaments in growing ends [4] is not likely to reduce the steric penalty since a single dimer layer is sufficient to impose the penalty. In contrast to global structures, these local structures have little effect (<20% between zero and two neighbors) on the arrival of freely diffusing subunits. Instead, the main effect of local structure is through inhibition of the eventual binding of subunits after they have approached the protofilament of interest (Figure 2.7B). This is consistent with a steric penalty, due to the constraint of orientation, imposed by the adjacent protofilaments.

If the penalty to the one and two-lateral neighbor case is indeed due to steric hindrance, then the more severe the orientation constraint, the greater the penalty should be. Therefore, we estimated the one and two-neighbor penalties for a range of tolerances in order to examine the constraint sensitivity of each penalty (Figure 2.7C and D). Not surprisingly, the two-neighbor case is penalized to a greater extent compared to the one-neighbor case for all tolerances within the range we examined. The one-neighbor penalty is relatively independent of tolerance while the two-neighbor penalty becomes more severe at lower tolerances. If we assume that the tolerance range for a microtubule is within the lateral interaction distance defined by [11] (< 4 Å), then protofilaments with one or two lateral neighbors will have ~2- or ~10-times, respectively, slower on-rate constants than those without neighbors. While our estimated on-rate constant for the blunt case is greater than previous estimates, the one neighbor case is within error of previous estimates (see [5] for summary). It is interesting to note that a binding site with a single lateral neighbor will be common within a tapered tip, thus the average association constant

($k_{on,MT}$) estimated from our model is within the range of previous estimates by both experimental and computational approaches [5].

As subunits get close to the binding position, it is possible that the lateral bond will reduce the steric penalty by providing additional favorable free energy, particularly in the presence of two lateral protofilaments. To examine whether this is expected to be a significant effect, we added the lateral bond consisting of two zones (one for α and β-tubulin each) on both sides of the αβ-tubulin subunit (Figure 2.1B). We decreased both the total bond energy and the spring constant of the lateral bond threefold compared to the longitudinal bond (see section 2.3.2). Doing so resulted in the lateral bond being ~14 k_BT weaker than the longitudinal (consistent with published estimates [30, 33, 57]) and made the binding radius (r_B) equal for both the longitudinal and lateral bond, giving the lateral bond the best chance to reduce the on-rate penalty. Even so, the lateral bond did not significantly reduce the severity of the one and two-neighbor penalties for the majority of tolerances examined (Figure 2.7C and D). Because the lateral bond is so weak compared to the longitudinal, the interaction is not sufficient to facilitate the establishment of a longitudinal interaction. This suggests that the longitudinal bond is necessary for a subunit to incorporate into the microtubule lattice (the relative strengths of the lateral and longitudinal bond is discussed further below).

The fact that even one neighbor is sufficient to inhibit the association of incoming subunits suggests that a similar effect will occur in all multi-stranded polymers. Even in a two-stranded polymer, such as F-actin, one protofilament will be longer than the other, resulting in multiple local structure conditions for incoming subunits (Figure 2.1A). In order to assess the generality of structurally induced kinetic penalties in linear polymer assembly, we simulated G-actin monomer subunit binding to the leading and lagging protofilament of a two-protofilament polymer. In simulating actin instead of tubulin, we shortened the long axis of the super-ellipsoid used to define a subunit and adjusted the total bond interaction energies (U_{bond}) and bond stiffness (k_{bond}) to better match previous

estimates for actin (see section 2.3.3). As seen in Figure 2.7E, the estimated on-rate constant is reduced by ~1.5-fold for the lagging protofilament compared to leading protofilament. Similar to tubulin, the addition of diagonal bonds did not reduce the steric penalty imposed by the leading protofilament. The effect of one-neighbor is not as strong for F-actin compared to the microtubule, however, our results show that neighboring protofilaments sterically hinder addition to lagging protofilaments even in the simple case of a two-stranded polymer.

2.4.3 Kinetic penalties influence polymer tip structures

Despite the one-neighbor on-rate constant being only a factor of two slower compared to zero-neighbors, it can potentially have a significant effect on net assembly if it occurs frequently. To investigate the consequence of our predicted on-rate penalties, we examined the resulting microtubule tip structure from simulations of individual microtubule net assembly according to [33], without penalties, with only a two-neighbor penalty [5], and with our model predicted penalties for both one and two lateral neighbors (from Figure 2.7C and D). Without penalties, individual protofilaments remain of about equal length and tip structures do not achieve the same extension compared to simulations with penalties (Figure 2.8A and B). A two-neighbor penalty is sufficient to achieve experimentally observed tapers [4], however, typically results in a single protofilament that lags many dimer layers behind the others, which remain of about equal length (Figure 2.8A and C). It is unlikely that this single trailing protofilament would be resolved by experimental methods and thus would appear as a relatively blunt tip since the fraction of zero and one-neighbors is comparable to the non-penalized case (Figure 2.8C). Our estimate of the two-neighbor penalty is comparable to that required for quantitative agreement with the protofilament standard deviation in GMPCCP microtubules [5]. Addition of the one neighbor penalty, however, resulted in a gradual loss of protofilaments out to the microtubule end, more closely resembling those structures observed by electron microscopy [4, 6, 9] (Figure 2.8A).

Additionally, the one-neighbor penalty shifted the majority of protofilaments from zero neighbors to one and two neighbors in tapered tips compared to blunt (Figure 2.8D). As the microtubule on-rate constant is determined by the fraction of protofilaments in each condition, tapered tips will have a slower on-rate constant than blunt tips in this case. In fact, we found the average on-rate constant ($k_{on,MT}$) for the microtubule end decreased ~22% in tapered tips compared to blunt in the case with one- and two-neighbor penalties, however, the on-rate constant decreased only ~7% in the case of a two-neighbor penalty only. Thus, on-rate penalties dictate the resulting tip structure, which will feed back to influence association and promote further tapering of the tip.

The observed kinetic inequality between protofilaments due to the local structure provides a potential explanation for the observed history dependence of both catastrophe [6–8] and rescue [69]. While it has been shown that gradual tapering of the microtubule tip leads to a higher probability of catastrophe with microtubule age [6], it is not clear how tip taper promotes catastrophe. A potential explanation is that increased taper will correspondingly increase the off-rate ($k_{off,MT}$) due to the loss of stabilizing lateral bonds [5], thus reducing the net assembly rate. If tip taper only increases $k_{off,MT}$, however, it would be difficult to lose a large GTP-cap at higher tubulin concentrations and as estimated *in vivo* [42]. Our results here suggest that, in addition to affecting the off-rate, increasing tip taper will result in a decrease of the average on-rate constant for the microtubule ($k_{on,MT}$). Thus, the net addition of subunits will potentially decrease to a greater extent and be more variable in time. As the net assembly rate is the small difference between a large on- and off-rate [5], changes in both $k_{on,MT}$ and $k_{off,MT}$ could switch the microtubule from a state of net assembly to net disassembly. Thus, a tapered tip will have a net assembly rate that is lower than a blunt tip. We suggest that, rather than there being a series of specific events leading to catastrophe (as indicated by [7, 8, 70]), gradual tapering of the microtubule tip [6], on average, transitions it to a state of net disassembly, resulting in the loss of the GTP-cap and catastrophe. It may be

challenging to experimentally detect this transition, however, as individual tips are highly dynamic [5, 6] and variable [4]. In contrast to growth, as a microtubule shortens the tip will evolve towards a blunt structure because of the stability of subunits with two lateral bonds within the microtubule lattice compared to those with one or zero. The transition toward a blunt tip will result in an increase in the net assembly rate, allowing the microtubule to re-establish its GTP-cap and rescue as a result. Thus, the feedback relationship of $k_{on,MT}$, $k_{off,MT}$ and tip structure can explain history dependent catastrophe and rescue through the gradual transition between microtubule tip states biased toward net assembly or disassembly.

2.4.4 Influence of hydrodynamic interactions on stereospecific binding in linear polymers

As two Brownian particles approach each other or as a particle approaches a wall, the solvent between them must be forced out, resulting in an increased drag force upon approach [71]. In the absence of inter-particle interaction potential, these hydrodynamic interactions reduce the diffusion-limited rate of encounters by ~30% [72, 73]. In the presence of an interaction potential, hydrodynamic interactions induce correlation between the movements of nearby molecules, increasing the translational diffusion coefficient while reducing rotational diffusion [67]. Thus, it seems that it might be important to include these interactions in any kinetic simulation. In the model described here, freely diffusing subunits bind to sites at the end of the microtubule lattice, which can be thought of as immobile compared to the freely diffusing subunit. Hydrodynamic interactions between the free subunit and the lattice, therefore, will be similar to a particle approaching a wall as described by [71]. In this case, hydrodynamic interactions result in a distance dependent effect on the fluid viscosity, η. Therefore, we sought to examine the expected effects of fluid viscosity on the resulting kinetic rate constants.

When considering stereospecific-binding interactions, one must consider both the rate at which molecules collide as well as whether they are properly aligned

upon collision. If not initially aligned properly, binding partners can explore additional configurations through rotational diffusion during a single encounter, thereby promoting binding [55]. Thus, the efficiency of binding will be dependent on the duration of the encounter and the extent of rotational diffusion during a single encounter

$$\phi = \frac{\left\langle \Delta\theta^2 \right\rangle^{1/2}}{2\pi} = \frac{(2D_r\tau_E)^{1/2}}{2\pi} \tag{2.26}$$

$$\tau_E = \frac{\delta^2}{6D_t} \tag{2.27}$$

where ϕ is the binding efficiency, δ is the encounter distance, and D_r and D_t are the rotational and translational diffusion coefficients, respectively. Using our model parameters in equations 2.26-2.27, assuming $D_t = D_{avg}$ and $\delta = 2r_B$, we estimate ϕ = 0.025, which is nearly identical to that resulting for $N = 1$ (purely diffusive motion) in our simulation (Figure 2.5A). Predicting how the binding efficiency will scale with viscosity, η, we see

$$\phi = \frac{(2D_r\tau_E)^{1/2}}{2\pi} \propto \left(\frac{D_r}{D_t}\right)^{1/2} \propto \left(\frac{\frac{1}{\eta}}{\frac{1}{\eta}}\right)^{1/2} \tag{2.28}$$

Increased viscosity results in a longer encounter but also slows rotational diffusion, and therefore the binding efficiency does not depend upon the viscosity. Assuming the association rate constant is the diffusion-limited collision rate (Smoluchowski rate from equation 2.12) scaled by the binding efficiency

$$k_{on} = \phi k_D \propto (\text{const.})\frac{1}{\eta} \tag{2.29}$$

Thus, the net-effect of hydrodynamic interactions on the rate constant will be equivalent to reduction in diffusion-limited collisions due to distance dependent changes in the viscosity. As noted above, this is predicted to be ~30% reduction for two-spheres [72, 73]. Therefore, we predict that incorporating hydrodynamic interactions will reduce the estimated values for the on-rate constant, however, will

not influence the binding efficiency of individual subunits. As the effects of global and local structures at the end of the microtubule are due to the binding efficiency (Figure 2.5 and 2.7) and not due to the translational diffusional approach to a position close to the binding site (i.e. 10 nm in the present study), we have ignored explicit inclusion of hydrodynamic interactions in the results presented here. Instead, the simulation results can be corrected by ~30% to provide more accurate estimates of association rate constants.

2.4.5 Simulating subunit dissociation closes the thermodynamic loop

Since the local tip structure affected the association rate constant, we were interested to assess whether it also affects the dissociation rate constant. For a bimolecular reaction, the standard Gibbs free energy of association (ΔG^0) is related to the ratio of the association and dissociation rate constants by

$$\Delta G^0 = -k_B T \ln(k_{on} / k_{off}), \tag{2.30}$$

where k_{on} is defined to have units of $M^{-1}s^{-1}$ and k_{off} to have units of s^{-1}. Due to the nature of our simulation, we separated the standard Gibbs free energy into two contributions: the intrinsic bond energy (ΔG^0_B), a large negative value assumed here to mainly be the hydrophobic interactions between tubulin subunits in the specific case of the microtubule, and an entropic penalty of binding (ΔG^0_S), a positive value due to the loss of translational and rotational freedom upon binding [57, 60, 68, 74] such that

$$\Delta G^0 = \Delta G^0_B + \Delta G^0_S . \tag{2.31}$$

As we have already simulated the association of freely diffusing subunits, we can obtain a complete thermodynamic picture of αβ-tubulin subunits at the dynamic end of microtubules by simulating their subsequent unbinding. We defined the time to unbind as the amount of time that passed between when a subunit is completely

bound to when it returns to a center-to-center separation distance where the probability of rebinding is < 0.01 (R_U = 11 nm, see section 2.3.6).

As noted above (see section 2.3.9), U_{bond} is not equivalent to ΔG^0_B, since for $\Delta G^0_B = U_{bond}$ all interacting zones have to be perfectly aligned ($r_i = 0$ for all i). This is rarely the case as one zone's energy decreases at the cost of another zone as the subunit rotates about its center. Instead, we consider U_{bond} to be an adjustable parameter that will set the intrinsic bond energy, but is not necessarily equal to it. To estimate ΔG^0_B from the simulation, we calculated the time averaged interaction energy while a subunit was within R_U, according to

$$\Delta G_B^0 = \frac{\sum_{i=1}^{m}\sum_{j=0}^{n-1} U\left(t_j\right)\cdot\left(t_{j+1}-t_j\right)}{\sum_{i=1}^{m} t_n(i)}, \qquad (2.32)$$

where m is the total number of unbinding events simulated and n is the number of steps taken before unbinding for a given unbinding event.

To check that our simulations agreed with theoretical thermodynamic expectations, we estimated $k_{on,PF}$, k_{off}, and ΔG^0_B for values of U_{long} within the range estimated for the longitudinal bond (see section 2.3.9). From these estimates, we could then estimate ΔG^0 by equation 2.30 and ΔG^0_S from equation 2.31. As shown in Figure 2.9, both $k_{on,PF}$ and k_{off} are dependent on the value of the total bond energy (U_{long}). From this we found that U_{long} = -20.4 k_BT resulted in $\Delta G^0_{long} \approx$ -6.8 k_BT, as estimated previously for the longitudinal bond [33] (Figure 2.9C). The intrinsic bond energy (ΔG^0_B) becomes more favorable with decreasing values of U_{long}, approaching its value but never equal to it. Our estimated values for ΔG^0_B within this range of U_{long} are comparable to previous estimates for the intrinsic energy of the longitudinal bond [33, 57]. Interestingly, ΔG^0_{long} is greater than ΔG^0_B for all values of U_{bond} (Figure 2.9C). This is due to the loss of translational and rotational freedom introduced by the implementation of Boltzmann's law while the subunit is bound (see section 2.3.4). Thus, the entropic penalty of binding comes out naturally

from the simulation. In the range of values for U_{long} used here, our estimate of the entropic penalty of binding, $\Delta G^0_S \approx 10\ k_B T$, is comparable to previous estimates based on tubulin polymerization [57], actin fragmentation [60], as well as experimentally observed filament lengths [75] and is independent of the total bond energy. Thus, all three components of equation 2.31 can be extracted from the simulation for a given parameter set and, using our estimate of $U_{long} = -20.4\ k_B T$, are in agreement with previous estimates for tubulin-tubulin interactions.

A summary of complete kinetic and thermodynamic (estimated using Equations 2.30-2.32) results for varying local conditions is shown in Table 2.1 (see Table 2.2 for F-actin). Interestingly, the estimated entropic penalty of binding is nearly equal between the zero and one-neighbor condition (~1 $k_B T$ difference, which can mostly be attributed to the ~twofold steric penalty to the on-rate, ln(2) = 0.7 $k_B T$). This indicates that once a subunit is bound longitudinally it does not pay an additional entropic penalty by forming the lateral bond (consistent with the assumption in [33] that the entropic penalty is absorbed entirely by the longitudinal bond). Thus, lateral bonds have a significant stabilizing effect (~60-fold to > 300-fold longer subunit lifetime with one and two lateral bonds, respectively) by contributing favorably to the free energy of association. While we only set an upper limit for the off-rate for subunits with two lateral bonds (see section 2.3.6), this upper limit is still 5-fold lower than with one lateral bond, thus we expect the addition of the second lateral bond to further contribute favorably to the free energy.

The observed stabilizing effect of the lateral bond is dependent upon the longitudinal bond being established first. Lateral bonds, by themselves, are unfavorable because the entropic penalty of binding is greater than the intrinsic bond strength of the lateral bond, resulting in a very short-lived interaction (Table 2.3). The exceptionally short duration of lateral bonds in the absence of a longitudinal bond (~ 0.1 μs) explains why they were not able to overcome the steric penalty imposed on association by lateral neighbors (Figure 2.7). The reduction in free energy by one lateral bond (-3.6 $k_B T$) is less than previously estimated for the

lateral bond [33], however, it would become more negative for decreasing total bond energies (U_{lat}). Therefore, we do not consider this to be an estimate of ΔG^0_{lat}, but rather a value determined by the total interaction energy used in the simulation, i.e. U_{lat} could be adjusted downward to obtain previously estimated values of ΔG^0_{lat}. Even so, the total bond energy would still be on the order of the entropic penalty. Thus, we conclude that subunits adding to the microtubule lattice require the stronger longitudinal bond to incorporate into the lattice.

The necessity of the longitudinal bond is in qualitative agreement with the suggestion that "cracks" between protofilaments may be present within the lattice due a delay in lateral bond formation after a subunit binds [35], however, we argue that quantitatively they would be extremely short lived as we find lateral bonds form rapidly after the longitudinal bond (7.0 ± 0.7 ns for one and 9.0 ± 0.8 ns for two lateral bonds, mean ± SEM) in our model. The necessity of the longitudinal bond further suggests that additions with either a single or two lateral bonds but no longitudinal bond, resulting in a lattice defect, would be very rare due to their extremely short duration. Thus, the strength difference between the longitudinal and lateral bonds may be an evolutionary advantage to reduce the frequency of lattice defects and resulting structural weakness.

2.4.6 Sensitivity of model predictions to the interaction potential

To explore whether or not our results were specific to the specific shape of the harmonic potential of interaction, we simulated subunit binding and unbinding using a Lennard-Jones (LJ) interaction potential where the interaction energy for an individual zone was given by

$$U_i(t_j) = -U_{long,i}\left[\left(\frac{r_m}{r_m + r_i(t_j)}\right)^{12} - 2\left(\frac{r_m}{r_m + r_i(t_j)}\right)^{6}\right] \text{ for } r_i(t_j) > 0 \qquad (2.33)$$

Here r_m is the distance at which $U_i = U_{long,i}$ and $r_m = 2^{1/6}\sigma$, where σ is a shape parameter that defines the slope of the function for a given value of $U_{long,i}$, similar to the harmonic spring constant. We added r_m to the denominator since r_i is the

distance between two points on the surface of the subunits. This ensured that $U_i = U_{long,i}$ when $r_i = 0$. The repulsive portion of the LJ potential for $r_i < r_m$ was maintained by hard-sphere rejection. For simulations using a LJ potential, we defined r_B as the point where the slope, or equivalently the inter-particle force, was at its maximum value.

As shown in Figure 2.11, the predicted kinetic and thermodynamic trends for LJ are similar to those predicted using a harmonic potential (Figure 2.9 and 2.10). Stronger bonds (more negative U_{long}) resulted in higher $k_{on,PF}$, lower k_{off}, and thus a more favorable interaction (more negative ΔG^0_{long}). The same trend was observed for softer bonds (more positive shape parameter, σ). Unlike the harmonic potential, we found the estimated entropic penalty of binding (ΔG^0_S) was sensitive to the total bond energy of the LJ. This is because for constant σ, the slope of the LJ potential becomes steeper for more negative values of U_{long}. In contrast, the slope of the harmonic potential is only sensitive to the bond stiffness, k_{long}. Thus, more negative values of U_{long} in the LJ potential also effectively stiffen the bond. When considering this, the trend in ΔG^0_S with regards to bond stiffness is equivalent to that observed for a harmonic potential. In the absence of lateral neighbors, we found that using $U_{long} = -30\ k_BT$ and $\sigma = 0.6$ nm resulted in $\Delta G^0_{long} \approx -6.8\ k_BT$, and therefore used these values in all subsequent simulations. As shown in Figure 2.12, the estimated on-rate constant was slightly lower using a LJ potential for each local condition, however, the steric penalties imposed by local structure were the same as estimated for a harmonic.

In addition to the shape of the potential, it is possible that the parameters used to define the harmonic potential may reduce the steric penalty imposed by laterally adjacent protofilaments. In particular, increasing the bond stiffness would increase the inter-particle force and may help to align subunits in the one and two neighbor case. Alternatively, softer bonds may be able to interact for a longer period of time, while the subunit aligns with the neighboring protofilaments. Therefore, we estimated the penalties for varying longitudinal bond stiffness. While

the bond stiffness affected both the estimated on-rate constant and the off-rate constant (Figure 2.10), there was no significant effect on the penalties imposed by either one or two lateral neighbors (Figure 2.12C and D). These results indicate that the absolute value of the model estimated values depend upon the shape of the chosen potential as well as the parameters that describe it, however, the kinetic rate penalties as well as the kinetic and thermodynamic trends are robust and relatively insensitive to the particular mathematical form of the attractive potential.

2.4.7 A model to investigate the actions of microtubule-associated proteins and drugs

To our knowledge, the model described here is the first to bridge the gap between molecular dynamics level models [28–32] and dimer level stochastic microtubule models [33–37, 40]. Thus, the Brownian dynamics modeling approach we employed here provides a new method to analyze the effects of microtubule-associated proteins (MAPs) and microtubule-directed drugs for which the relative structure and interaction with the microtubule lattice is known. The simplest cases are interactions that modify one of the parameters included in our model, such as longitudinal or lateral bond energy or bond stiffness. For example, the majority of studies have found that paclitaxel decreases the rigidity of microtubules [76–80], except one which saw the opposite effect [81]. Because of its binding position close to the M-loop of the β-monomer, it has been suggested that paclitaxel may function to increase the strength of the lateral bond to overcome nucleotide-based structural changes of the tubulin dimer [11, 27]. Further, drug binding to the taxane-pocket of β-tubulin structures the M-loop closer to that of the bound state prior to incorporation into the lattice [82]. "Structuring" of the M-loop implies an increase in stiffness in the presence of paclitaxel, which agrees with molecular dynamics simulations which found the M-loop shows reduced root-mean-squared fluctuations in stable forms of tubulin [28, 29]. In addition to locally altering the lateral interactions, paclitaxel has long-range allosteric effects on the residues that

establish the longitudinal bond interface (T1-T5 and H11 loops) in β-tubulin, increasing the root-mean-squared fluctuations [28].

While it may not be clear which effect (lateral or longitudinal) of paclitaxel is more important for stabilization, it can be assumed that paclitaxel modifies the intrinsic rigidity of regions within the tubulin dimer involved in establishing inter-dimer interactions. Our model predicts that increased bond stiffness decreases the on-rate constant and increases the off-rate, meaning that softer bonds lead to a more favorable interaction (more negative ΔG^0_{long}; Figures 2.10 and 2.11). Despite influencing the on-rate constant, the bond stiffness had no effect on the steric penalties imposed by laterally neighboring protofilaments (Figure 2.12). Interestingly, the intrinsic bond strength estimated from the simulation (ΔG^0_B) is not sensitive to the bond stiffness. Therefore, the change in ΔG^0_{long} is due to the entropic penalty of binding (ΔG^0_S) (Figure 2.10). Because softer bonds do not constrain the translational and rotational freedom to the extent that stiffer bonds do, the entropic penalty of binding is reduced for softer longitudinal bonds.

These results indicate that the stabilizing modifications of paclitaxel are likely through the longitudinal rather than the lateral bond, as structuring of the M-loop itself will be unfavorable due to an increased entropic penalty. To combat this, however, rearrangement of the M-loop favorably positions several additional residues to form lateral contacts with the neighboring β-tubulin [82]. These counteracting effects of paclitaxel could potentially explain experimental results that paclitaxel has no net effect on the lateral interaction between protofilaments when deformed by osmotic stress [83]. Our model predicts that softening of the longitudinal bond should increase the association rate constant in the presence of paclitaxel (Figure 2.10A), and therefore should increase the polymerization rate. While this increase has not been observed experimentally, it may be difficult to detect as paclitaxel increases the amount of tubulin in polymer form at the expense of free tubulin in solution [84, 85]. A drop in the free concentration would

counteract any increase of the association rate constant such that the on rate (k_{on}^{*} = $k_{on,MT}$ [Tub]) might change only weakly in the presence of paclitaxel.

Our Brownian dynamics simulations emphasize the inefficiency of subunit addition, despite the presence of a favorable interaction potential [55]. Of those that reach R = 10 nm, only 0.5% ultimately bind (Figure 2.5A). Additionally, although a high percentage of free subunits get close to binding (N = 1), the vast majority ultimately diffuse away from the microtubule lattice before forming a more specific bond and incorporating into the lattice (~80%, Figure 2.5A). By increasing the probability that these "nearly bound" units ultimately bind, a MAP or microtubule-targeting drug could significantly affect the rate at which subunits incorporate into the lattice ($k_{on,PF}$). In fact, it was suggested that XMAP215 functions in this manner to increase the on-rate constant, by stabilizing an intermediate, diffusion-limited collision complex [15]. Any molecule that binds at the microtubule end will impose an unfavorable steric penalty, similar to that which we have shown here for one and two neighboring protofilaments. Thus, for a MAP to function as proposed for XMAP215, an additional favorable effect will have to overcome this steric effect. Additionally, the free subunit would have to associate very favorably with the MAP, because a relatively weak bond, such as the inter-dimer lateral bond, does not affect the on-rate constant (Figure 2.7). Incorporating an interaction similar to that described for XMAP215 into our model could give estimates for the minimum bond strength necessary to increase the on-rate. Alternatively, if a MAP strengthens (makes more negative) the intrinsic bond free energy or decreases the longitudinal bond rigidity it would be predicted to increase the on-rate constant by our model (Figures 2.9-2.11).

2.5 Conclusions

We have developed the most detailed kinetic and thermodynamic computational model to date for the association and dissociation of individual tubulin subunits at the microtubule plus-end, and find that it is consistent with both

experimental observations and theoretical predictions for tubulin-tubulin interactions. This model demonstrates that the on-rate for individual strands in multi-stranded polymers are independent of the global position, however, local structure imposes a steric penalty on association. Thus, the microscopic on-rate constant will be an average of the individual nanoscale protofilament on-rate constants and therefore will vary in time as subunits are gained and lost at the dynamic end. These findings are robust with regard to molecular structure and the precise shape of the inter-particle potential. Therefore, we believe similar effects will arise in not only other linear polymers, but also any system where local steric constraints are placed on binding. The simulation results suggest a feedback mechanism that slows subunit net addition as the microtubule tip tapers, which would promote history-dependent catastrophe and the possibility of more efficient search-and-capture by microtubule plus-ends *in vivo* [86]. Additionally, the approach that we employ here provides a new model with which to theoretically investigate, at a sub-nanometer length scale and ps to ms time scale, the actions of MAPs and microtubule-targeting drugs on tubulin kinetics and thermodynamics.

2.6 Acknowledgements

The authors would like to thank Dr. David Sept, Dr. Brannon McCullough, and Joseph Powers for helpful discussions. Simulations were carried out in part through use of computing resources at the University of Minnesota Supercomputing Institute. This work was supported by R01-GM-71522 and R01-GM-76177 to DJO.

2.7 Tables and Figures

TABLE 2.1 Summary of simulation results with zero, one, and two lateral bonds in addition to the longitudinal bond

	Longitudinal Bond Only	**Longitudinal and Lateral Bond**	
Model-estimated parameters	0 Lateral Neighbors	1 Lateral Neighbor	2 Lateral Neighbors
$k_{on,\mathrm{PF}}$ ($\mu M^{-1}s^{-1}PF^{-1}$)	12.7	7.4	1.7
k_{off} (s^{-1})	15 x 10^3	250	< 50
ΔG^0_{B} ($k_{\mathrm{B}}T$)	-17.7	-22.6	-28.5
ΔG^0 ($k_{\mathrm{B}}T$)	-6.7	-10.3	< -10.4
ΔG^0_{S} ($k_{\mathrm{B}}T$)	+11.0	+12.3	< +18.0

TABLE 2.2 Model estimated kinetics and thermodynamics for F-actin.

Model-estimated parameters	Leading PF 0 LN	Lagging PF ½ LN	Lagging PF 1 LN
$k_{on,\mathrm{PF}}$ ($\mu M^{-1}s^{-1}PF^{-1}$)	13.7	10.7	9.4
k_{off} (s^{-1})	35 x 10^3	320	< 42
ΔG^0_{B} ($k_{\mathrm{B}}T$)	-16.1	-21.5	-28.5
ΔG^0 ($k_{\mathrm{B}}T$)	-6.0	-10.4	< -12.3
ΔG^0_{S} ($k_{\mathrm{B}}T$)	+10.1	+11.1	< +16.2

TABLE 2.3 Summary of simulation results with lateral bond only

	Lateral Bond Only, no Longitudinal Bond	
Model-estimated parameters	1 Lateral Neighbor	2 Lateral Neighbors
$k_{on,\mathrm{PF}}$ ($\mu M^{-1}s^{-1}PF^{-1}$)	0.15	0.10
k_{off} (s^{-1})	10^7	7 x 10^6
ΔG^0_{B} ($k_{\mathrm{B}}T$)	-0.44	-3.4
ΔG^0 ($k_{\mathrm{B}}T$)	+4.4	+4.3
ΔG^0_{S} ($k_{\mathrm{B}}T$)	+4.8	+7.7

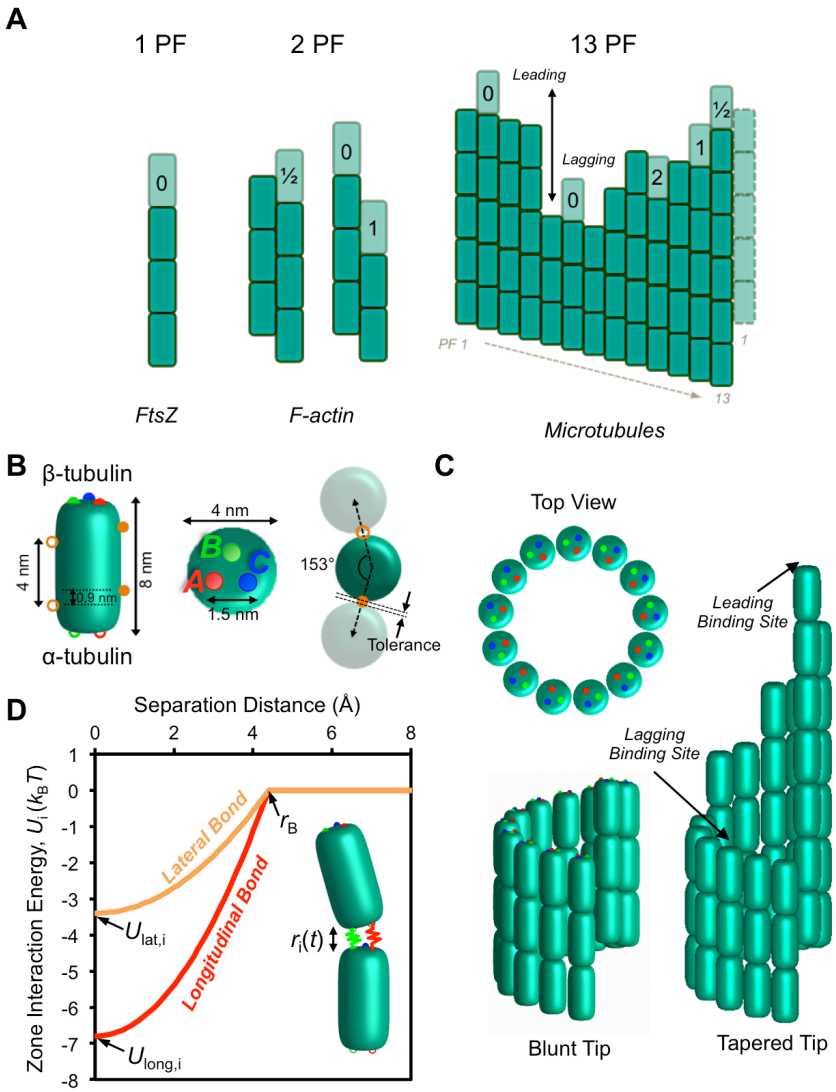

FIGURE 2.1 Simulated structures and interactions in linear polymer self-assembly
A) Examples of single and multi-stranded linear polymers are shown. The number of possible configurations increases with complexity. Darker subunits are bound, while lighter subunits represent potential binding sites for incoming subunits. The number of laterally interacting subunits is indicated for each binding site. B) Diagram of an αβ-tubulin subunit assumed within the model. Zones constituting the longitudinal bond are colored red (zone A), green (zone B), and blue (zone C). Lateral zones (α and β-tubulin) are shown in orange. Closed and open circles represent β- and α-tubulin, respectively, and indicate the paired binding partners on separate subunits (i.e. open green associates with closed green on a separate subunit). C) Diagram of the microtubule lattice as constructed within the simulation. Tapered example (right) is 4 dimer layers. D) Interaction energy as a function of separation distance is shown for a single longitudinal (red, one of three zones) and lateral bond (orange, one of two zones) zone. Interaction energy increases as a Hookean spring within the binding radius (r_B).

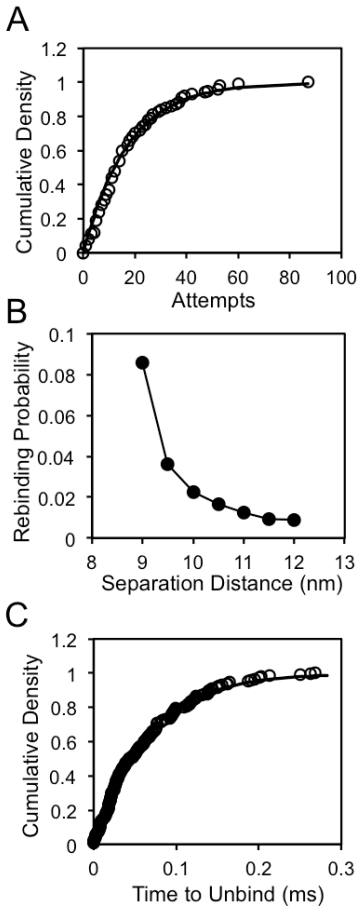

FIGURE 2.2 Defining a distance criterion for unbinding
A) Cumulative density function of the number of times that bound subunits reach the $N = 0$ (all zones separated by greater than the binding radius) state prior to diffusing to a center-to-center distance of $R = 11$ nm. The line is best fit of a geometric distribution (Kolmogorov-Smirnov test, $p > 0.05$), with mean $\mu = 17.7$. The fit of the geometric distribution indicates that a subunit has an escape probability of 0.06 ($P = 1/\mu$) or 94% chance of rebinding each occurrence of $N = 0$. B) The probability that a subunit completely rebinds ($N = 3$) before diffusing away to a 400 nm center-to center distance as a function of the subunit separation distance. Because diffusing subunits maintain rotational correlation between $N = 0$ and the unbinding distance, units are more likely to rebind compared to a random orientation. The probability decreases the further a subunit is allowed to separate from the protofilament of interest. We defined the unbinding distance by the separation where the probability of rebinding decayed to < 0.01, which was around 11 nm. As the minimum attainable center-to-center distance of bound units is 8 nm, units diffuse ~3 nm before being considered unbound. C) Cumulative density function of the times from the point of first complete binding ($N = 3$) to return to a separation of $R = 11$ nm. Using this distance criterion for unbinding, the unbinding times fit with the expected exponential distribution, fit line, (Kolmogorov-Smirnov test, $p = 0.82$) for a first-order rate.

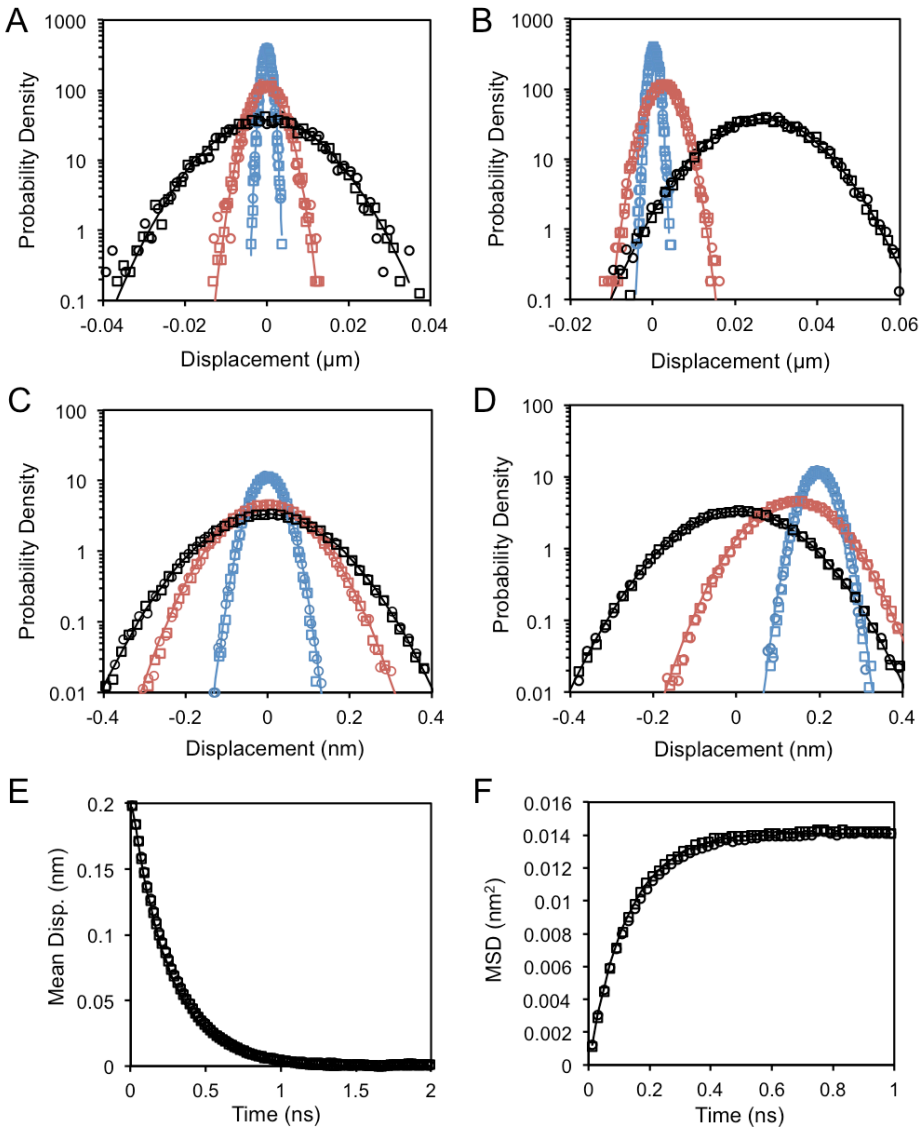

FIGURE 2.3 Comparing the modified Metropolis Monte Carlo to previous methods Results of modified MMC algorithm are represented by circles, while previous MMC methods are squares and theoretical expectation is solid lines. A-B) Resulting probability distributions in the absence (A) and presence (B) of a constant external force at 10 ns (blue), 100 ns (red) and 1 μs (black). In each run $x_0 = 0$. C-D) Probability distributions for diffusion in a harmonic potential where $x_0 = 0$ (C) or $x_0 = 0.2$ nm (D). Distributions were sampled after 10 ps (blue), 100 ps (red), and 1 ns (black). E-F) Starting from $x_0 = 0.2$ nm, the mean displacement (from $x = 0$, E) and the mean-squared displacement (F) were calculated at regular intervals in order to estimate the transition to the predicted steady-state distribution. Theoretical expectation (solid lines) was calculated from equation 2.15 (A and B), equation 2.16 (C and D), equation 2.17 (E), or equation 2.18 (F).

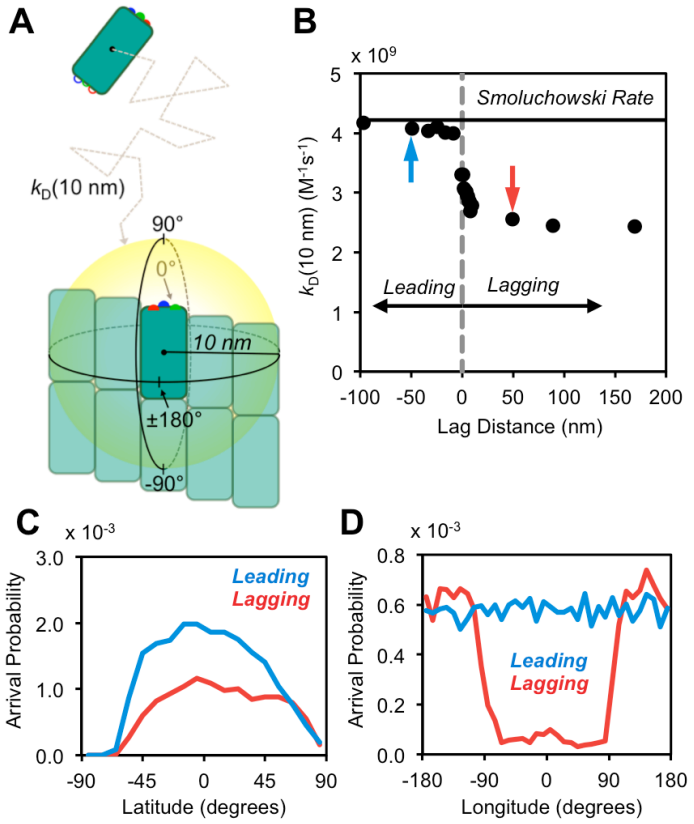

FIGURE 2.4 Diffusion-limited arrivals to leading and lagging protofilaments
A) Freely diffusing subunits arrive to a spherical surface (R = 10 nm, yellow) centered on the leading subunit of the protofilament of interest. Darker subunits identify potential binding partners (subunits of interest), while lighter subunits show the immediately surrounding microtubule lattice. B) Diffusion-limited arrivals to protofilaments at varying global positions within the microtubule tip. Solid black line shows the theoretical Smoluchowski limit to the yellow sphere shown in (A) ($4\pi D_{avg}R$). Gray vertical line marks zero lag. Blue and red arrows indicate the leading (blue) and lagging (red) cases shown in (C) and (D). C-D) Probability that a freely diffusing subunit (starting from R = 400 nm) reaches the 10 nm surface at a given position relative to the subunit of interest within the microtubule lattice.

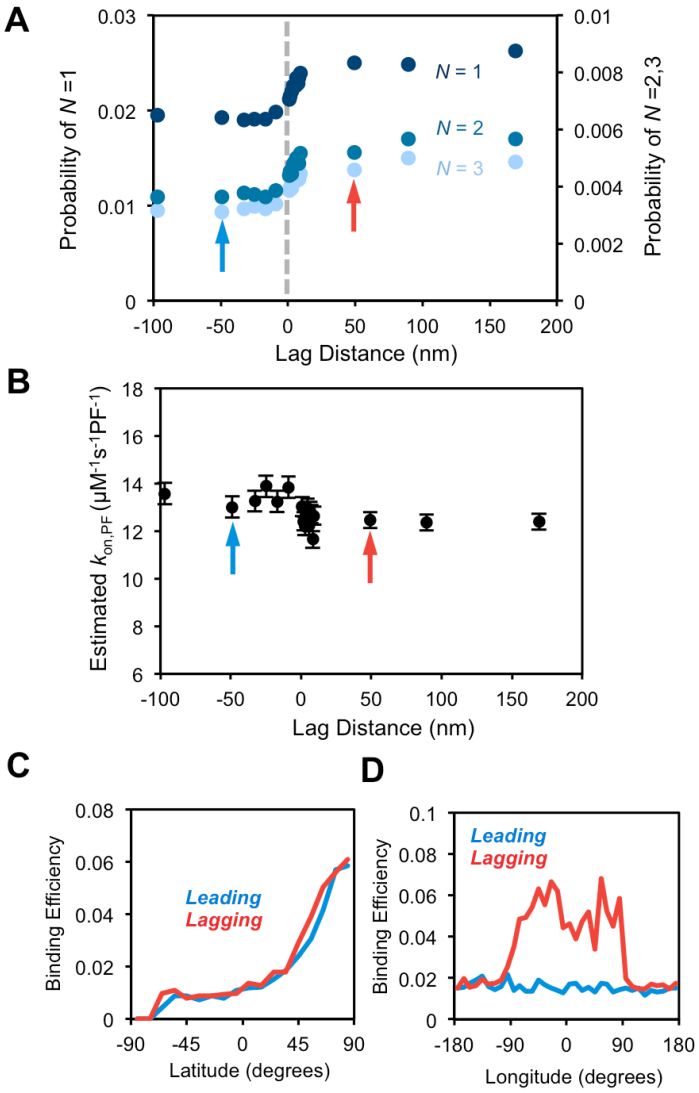

FIGURE 2.5 Binding efficiencies and estimated on-rate constants for varying global positions

A) The probability that subunits satisfy $N = 1$ (dark blue dots), $N = 2$ (blue dots) or $N = 3$ (light blue dots) longitudinal zones within r_B before diffusing to 400 nm center-to-center distance. Gray line marks zero lag. B) Estimated on-rate constants of completely bound subunits ($N = 3$) for a variety of global positions. In (A) and (B) the arrows indicate the leading (blue) and lagging (red) cases analyzed in (C) and (D). Error bars are SEM. (C-D) Binding efficiencies of all arrival positions are shown. Efficiency is the number of subunits per position that eventually bind before diffusing to 400 nm center-to-center distance divided by the total number of simulations initiated at that position.

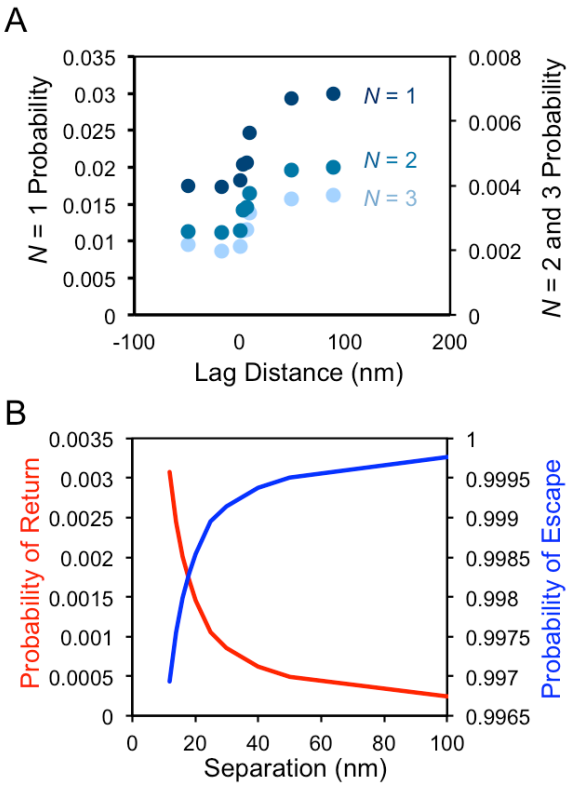

FIGURE 2.6 Analyzing the effects of global tip structure
A) Probabilities of reaching N = 1, 2, or 3 zones within the binding radius for binding simulations where the centroid starting position was randomly selected from points along a sphere with radius R =10 nm, centered at the centroid of the subunit of interest in the microtubule lattice. Randomization eliminated any potential spatial bias in the positions of diffusive arrivals. Similar to the trend seen for non-randomized starting positions, free subunits bind more efficiently to lagging protofilaments compared to leading. B) The probability of escaping (diffusing away before binding, blue line) and the probability of return (to R = 10 nm separation, red line) as a function of center-to-center separation distance. The probability of escape rapidly increases with separation distance within the range equal to the diameter of the microtubule (~25 nm), suggesting that the longer protofilaments could enhance binding to lagging protofilaments by inhibiting escape.

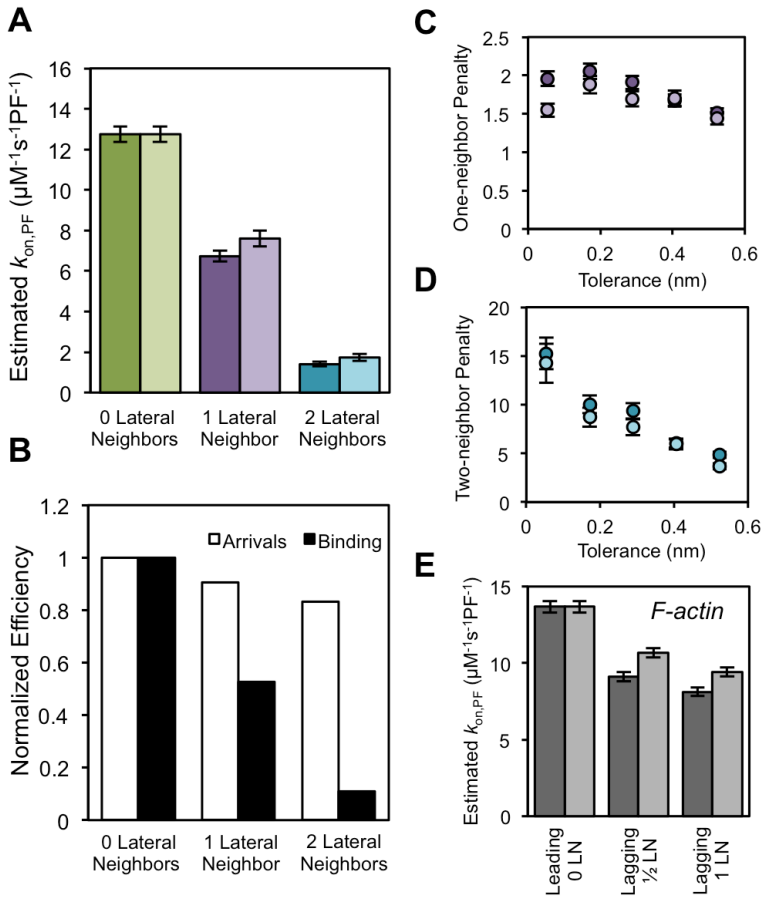

FIGURE 2.7 Dependence of on-rate constants on local tip structure
A) Estimated on-rate constants of freely diffusing subunits for all possible local configurations are shown. Rates for simulations with (lighter) and without (darker) the lateral bond result in equivalent estimates of the on-rate constant. B) Efficiency of diffusive arrivals to 10 nm center-to-center distance and subsequent binding are shown. Each is normalized to the respective zero neighbor case. (C-D) On-rate penalties (fold decrease from the zero neighbor case) for the single (C) and two (D) neighbor cases with (lighter) and without (darker) lateral bonds. Penalties were estimated across a range of tolerances, where tolerance is defined as the minimum distance between adjacent protofilaments within the microtubule lattice. E) Estimated on-rate constants of G-actin binding to the leading and lagging protofilament are shown (lateral neighbor numbers are illustrated in Figure 2.1A) for simulations with (lighter) and without (darker) the diagonal bonds. All error bars are SEM.

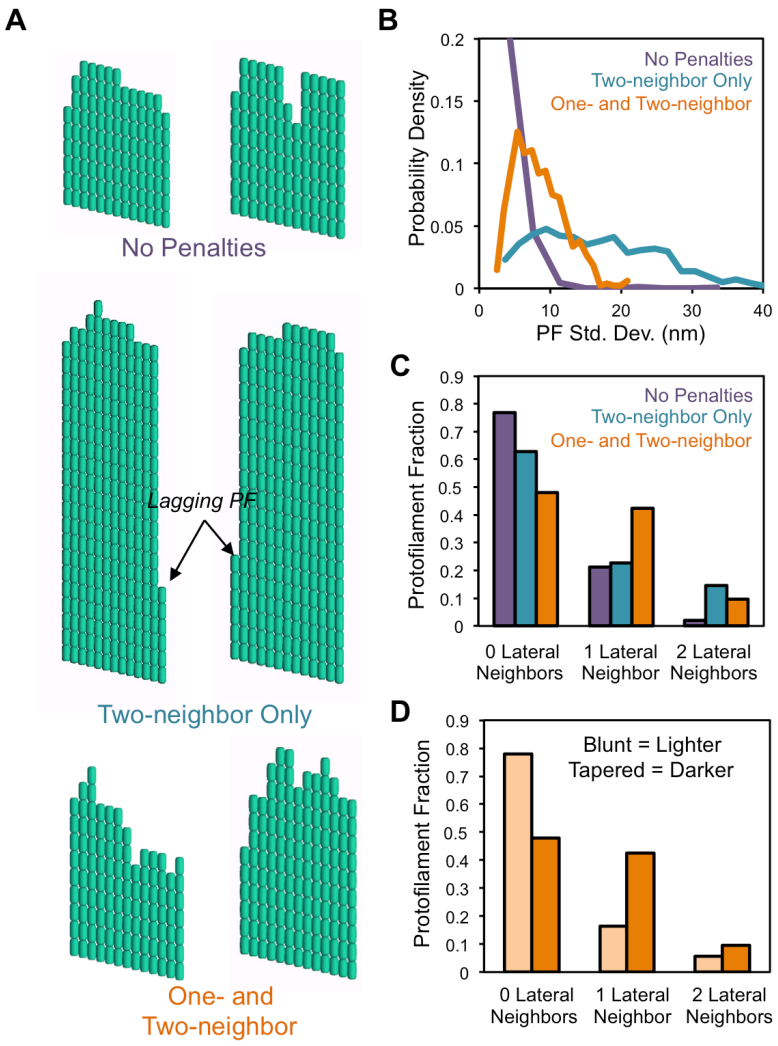

FIGURE 2.8 On-rate penalties influence the resulting microtubule tip structure
A) Examples of tapered microtubule end structures (displayed as two-dimensional sheets) from each of the three simulation conditions with no on-rate penalties (top), a single penalty to protofilaments with two-lateral neighbors (middle), and model predicted penalties to protofilaments with both one and two-lateral neighbors (bottom). B) The probability density of protofilament length standard deviations for tips in each simulation condition is shown. (C-D) The fraction of protofilaments with zero, one, or two lateral neighbors in (C) tapered tips from all three cases and (D) blunt (lighter) or tapered (darker) tips from simulations with one- and two-neighbor penalties.

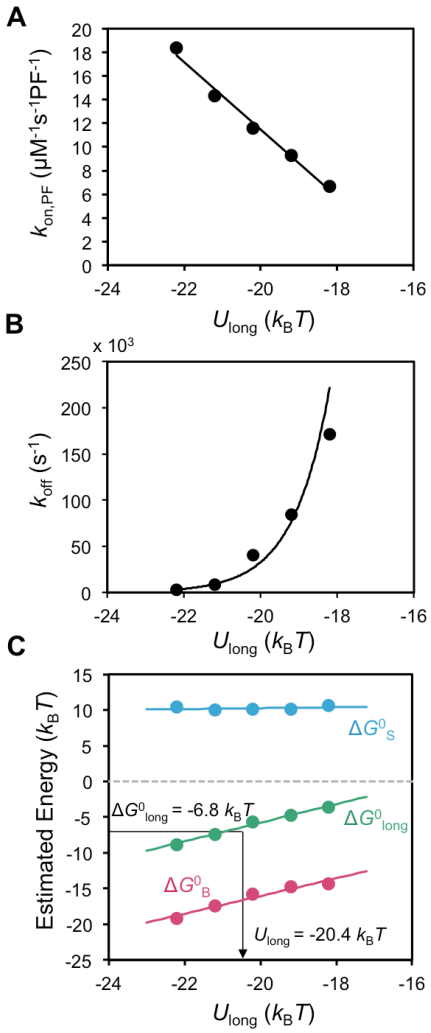

FIGURE 2.9 Extracting kinetics and thermodynamics from the model
The estimated on-rate constant (A) and off-rate (B) are dependent on the total bond energy (U_{long}) used to define the longitudinal bond and are calculated from the simulation. Trend line for k_{off} is best fit exponential. C) The standard Gibbs free energy (ΔG^0_{long}, green), intrinsic bond strength (ΔG^0_B, magenta) and entropic penalty of binding (ΔG^0_S, blue) are shown as a function of the total bond energy for the longitudinal bond. From the results in (A) and an estimate of the average ΔG^0_B within the simulation, ΔG^0_{long} and ΔG^0_S can be obtained. The total bond energy that best matched previous estimates of the longitudinal bond free energy (ΔG^0_{long}) was extracted from the resulting trend line. All trend lines are linear best fit, unless otherwise noted.

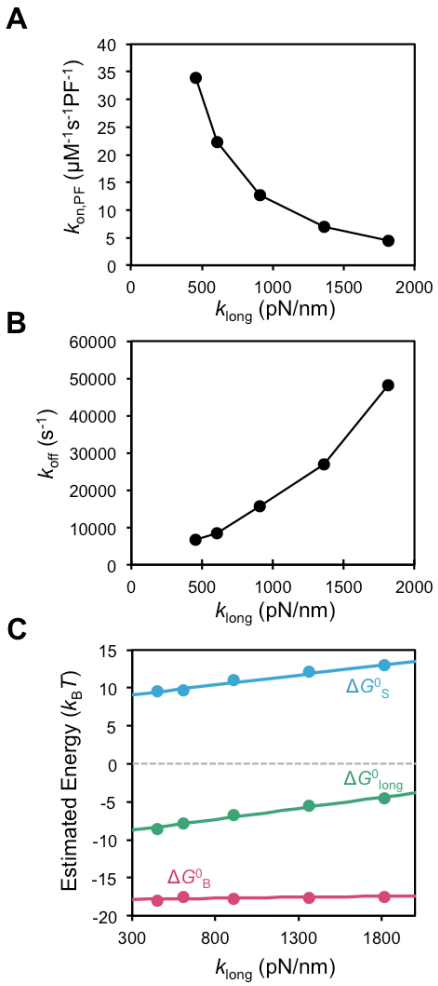

FIGURE 2.10 Kinetics and thermodynamic with varying bond stiffness
Kinetic and thermodynamic estimates for longitudinal bonds of varying stiffness are shown. Estimated on-rate constant (A) and off-rate (B) as a function of the stiffness of the longitudinal bond. All simulations are longitudinal bond only with constant total bond energy (U_{long} = -20.4 k_BT). C) The standard free energy (ΔG^0_{long}, green), intrinsic bond strength (ΔG^0_B, magenta) and entropic penalty of binding (ΔG^0_S, blue) are shown as a function of the longitudinal bond stiffness. All trend lines are linear best fit.

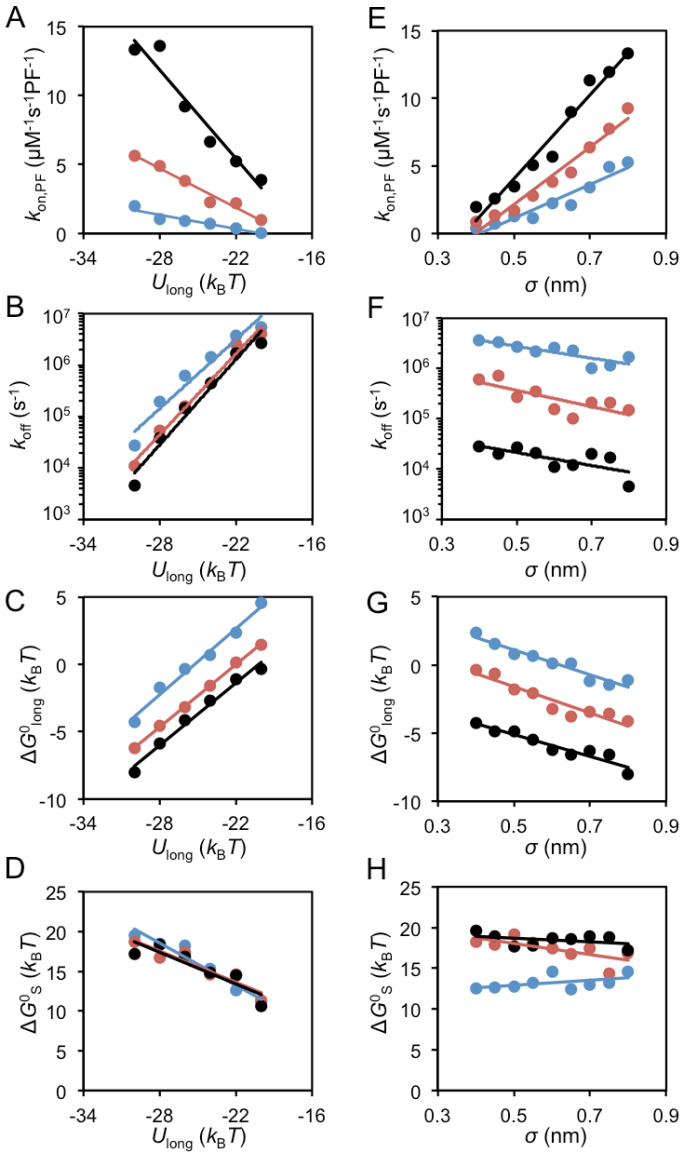

FIGURE 2.11 Kinetic and thermodynamic trends using a Lennard-Jones potential
Kinetic and thermodynamic trends with varying U_{long} (left) and σ (right) used to define the Lennard-Jones potential. For each condition 100,000 near-field binding runs and 10 unbinding runs were performed. A-D) For each value of U_{long}, σ = 0.4 nm (blue), 0.6 nm (red), or 0.8 nm (black). E-H) For each value of σ, U_{long} = -22 k_BT (blue), -26 k_BT (red), or -30 k_BT (black). We found that using U_{long} = -30 k_BT and σ = 0.6 nm resulted in $\Delta G^0_{long} \approx$ -6.8 k_BT, therefore these values were used to estimated $k_{on,PF}$ and the on-rate penalties for each local condition. All trend lines are linear best fit, except for k_{off} which is exponential.

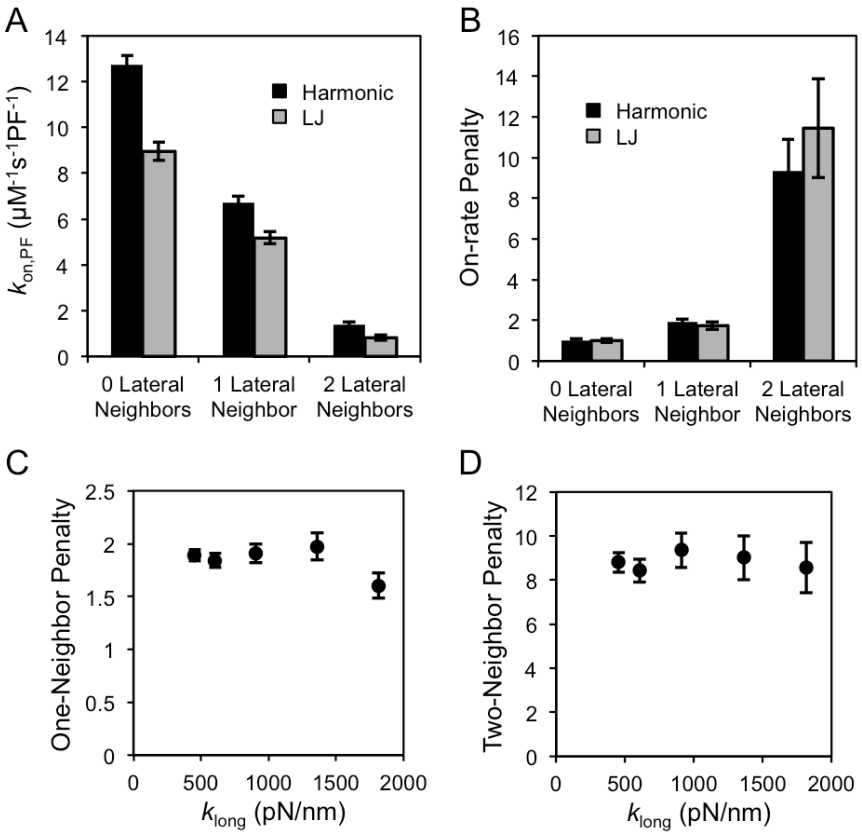

FIGURE 2.12 On-rate penalties are not sensitive to model parameters
A) Estimated on-rate constants in each local condition are shown when modeling the interaction potential as a harmonic or Lennard-Jones potential (LJ). Parameters for LJ potential were fit such that ΔG^0_{long} was equal to that using the harmonic. B) On-rate penalties for different potential shapes in each local condition. One-neighbor (C) and two-neighbor (D) on-rate penalties for a range of longitudinal bond stiffness values (harmonic spring constant). While the on-rate estimates are sensitive to the bond stiffness (Figure 2.10A and B), the on-rate penalties are independent of the bond stiffness. All error bars are 95% confidence interval.

CHAPTER 3

Requirements for dynamic instability and the mechanisms of microtubule-targeting agents

(Contributing Authors: Brian T. Castle, Louis S. Prahl, Jordan Bernens, and David J. Odde; *BTC performed all computational simulations and analysis, BTC and DJO designed experiments, while BTC, LSP, and JB collected and analyzed experimental data*)

3.1 Chapter Abstract

Dynamic instability, the characteristic self-assembly process in which microtubules alternate between extended periods of net assembly and disassembly, is essential for many cellular processes, including chromosome segregation during cell division. This essential role has prompted several decades of study of microtubule dynamics, yet the theoretical kinetic and thermodynamic requirements for the observation of dynamic instability remain to be described. Microtubule-targeting agents, which have been a widely successful treatment option for various types of cancer, bind directly to individual αβ-tubulin heterodimers, resulting in the loss of dynamic instability or "kinetic stabilization." Despite wide clinical use, the mechanisms of kinetic stabilization remain unclear and the proposed mechanisms have not theoretically been shown to in fact inhibit dynamic instability. In this study we integrate a computational model for microtubule assembly with nanometer-scale experimental measurements in living epithelial cells to identify the molecular kinetic and thermodynamic basis of kinetic stabilization by microtubule-targeting agents paclitaxel and vinblastine *in vivo*. In doing so, we identify the theoretical requirements for the existence of dynamic instability. We describe two mechanisms of kinetic stabilization that are consistent with *in vivo* experimental

observations, one that relies on true suppression of kinetics, and the other a 'pseudo' kinetic stabilization that results through thermodynamic convergence of the GTP and GDP states. Our analysis provides a theoretical foundation for the development of new microtubule-targeting agents as well as the improvement of existing ones.

3.2 Introduction

Microtubules are dynamic intracellular polymers that self-assemble from individual αβ-tubulin subunits aligned longitudinally to form protofilaments, and which interact laterally with each other to form a cylinder. Microtubules serve a crucial role in various cellular processes, including the segregation of replicated genomes during mitosis, which rely on the characteristic stochastic switching between extended periods of growth and shortening, termed dynamic instability [1]. Growth and shortening states are determined by the presence or absence, respectively, of a stabilizing cap of GTP, which is bound to the E-site of β-tubulin. As the GTP cap is lost, through hydrolysis and stochastic unbinding of GTP-tubulin, unstable GDP-tubulin subunits are exposed and the microtubule rapidly disassembles [3]. The process of switching from net growth to net shortening is termed "catastrophe," and the switching from net shortening back to net growth is termed "rescue." Various intracellular proteins as well as microtubule-targeting agents bind to the microtubule lattice and alter microtubule dynamic instability [14, 18]. The dynamics of growth and shortening as well as catastrophe and rescue are ultimately dictated by the underlying kinetics and thermodynamics of individual tubulin subunits. Therefore, to understand these microscale assembly dynamics and how they are altered, we must define the nanoscale requirements for dynamic instability at the level of individual subunits.

During mitosis, dynamic instability enables rapid and dynamic rearrangements of the microtubule array to find and mechanically couple to kinetochores, the specialized adaptor complex that links replicated chromatids to dynamic microtubule plus-ends. It is widely assumed that their central role in

mitosis has made microtubules one of the most common and successful targets for chemotherapeutic agents used to treat a wide variety of cancers including breast, prostate, and pancreatic cancer (see review from Dumontet and Jordan [18]). Due to their clinical relevance, there has been significant effort, using both structural and *in vitro* biochemical approaches, to understand microtubule-targeting agents' interactions with tubulin. For the most part, microtubule-targeting agents can be separated into two categories based on their binding site and effect on net microtubule polymer assembly. Disassembly promoters bind to either the colchicine domain, at the intradimer interface between α- and β-tubulin [25], or to the vinca domain, near the exchangeable GTP-binding site (E-site) on β-tubulin [26]. Assembly-promoters bind to the taxane pocket near the M-loop on β-tubulin, which is involved in establishing lateral contacts [11]. Despite having opposite effects on net microtubule assembly, the common phenotype of all microtubule-targeting agents is the dramatic attenuation of microtubule dynamic instability at nanomolar drug concentrations, often referred to as "kinetic stabilization," increasing the amount of time microtubules spend in a "paused" state [18]. It is interesting to consider how microtubule-targeting agents with opposite effects on microtubule polymer assembly ultimately lead to the same phenotype, kinetic stabilization, but an explanation has widely been ignored.

Despite years of intensive study, the molecular mechanisms of kinetic stabilization utilized by microtubule-targeting agents remain unclear. Due to the taxane site's proximity to the M-loop, it has been suggested that the assembly-promoter, paclitaxel, could stabilize lateral contacts [11, 27]. This hypothesis is supported by observed structural rearrangements of tubulin upon taxane site binding by assembly-promoters [82]. Alternatively, assembly-promoters, including paclitaxel, decrease the rigidity of microtubules [76–79, 87, 88], which will stabilize the microtubule from disassembly [34]. Still, others have argued paclitaxel most likely stabilizes microtubules via the longitudinal bond [89–91] or that paclitaxel promotes a GDP-tubulin conformation similar to that of GTP-tubulin [92].

Confounding results exist with regards to disassembly-promoters as well. In particular vinblastine, which binds to the vinca domain, disassembles microtubules yet increases tubulin-tubulin dimer affinity *in vitro* [93]. Due to vinblastine's binding location near the interdimer longitudinal interface, it could promote disassembly through steric hinderance of longitudinal contacts and displacement of lateral contacts as a result of inducing a curled orientation [26]. Vinblastine may increase dimer affinity by crosslinking adjacent tubulin dimers [26, 94], but this would have to override any potential steric hindrance induced by the presence of vinblastine.

While the proposed mechanisms are not mutually exclusive, much of the focus has been on the promotion of net polymer assembly or disassembly. It remains to be shown whether or not the proposed mechanisms will in fact lead to the observed universal phenotype of kinetic stabilization. Furthermore, it is difficult to connect the submolecular level effects of microtubule-targeting agents, measured by structural methods *in vitro*, to the tubulin subunit kinetics and thermodynamics [33], which dictate the microscale assembly dynamics. Finally, we ultimately seek to understand the mechanisms of kinetic stabilization in living cells, rather than with purified proteins *in vitro*. To address these issues, we examined the potential mechanisms of microtubule kinetic stabilization, at the level of individual tubulin subunit kinetics and thermodynamics, through the combination of a computational model and *in vivo* experimental observations. In doing so, we identify the theoretical requirements for the observation of dynamic instability with the goal of better understanding how microtubule-targeting agents can eliminate it. This theoretical examination of the mechanisms for kinetic stabilization by microtubule-targeting agents additionally provides a theoretical framework for the design and identification of new microtubule-directed drugs.

3.3 Results

3.3.1 Establishing the general requirements for the observation of dynamic instability

In order to understand the theoretical physical requirements underlying the microscale observation of dynamic instability, it is first necessary to define what is generally required. As originally described by Mitchison and Kirschner [1], dynamic instability is characterized by the stochastic switching between extended periods of two distinct states, one biased to net assembly (GTP-tubulin) and the other biased to net disassembly (GDP-tubulin). Therefore, the underlying kinetics and thermodynamics must establish an inherent difference between states as well as facilitate the transition between states. To examine the kinetic and thermodynamic requirements for establishing two states as well as the transition between them, we employed a computational model of microtubule self-assembly (Figure 3.1A) previously shown to reproduce dynamic instability that is based on earlier models for microtubule assembly [36, 95], and consistent with a range of experimental observations [33]. The current model was updated to include our recent estimates of kinetic heterogeneity in on-rate constants as a result of steric hindrance at the microtubule end (90; see also Chapter 2) (Methods). The benefit to using a model in this approach is that there are a limited number of free parameters (Table 3.1), which can each be examined independently for their effects on net assembly and dynamic instability.

To initially establish two distinct states, one biased to net assembly and one to net disassembly, we first simplified to a *single-state model* (setting $\Delta\Delta G^0 = 0 k_B T$), leaving only the longitudinal and lateral bond free energy (ΔG^0_{long} and ΔG^0_{lat}, respectively), the free tubulin concentration ([*Tub*]), and the individual protofilament on-rate constant ($k_{on,PF}$) as free parameters. Consistent with previous findings, the net-rate (v) increases in the regions with more negative bond free energy (Figure 3.1B; see also VanBuren et al. 2002 [33], Figure 1). This is because

net assembly is the small difference between a large number of addition and loss events [5]. Lower free energy reduces the rate of subunit loss, thus increasing the disparity between the number of additions and losses at the end of a growing microtubule. For a shortening microtubule, lower free energy will reduce the rate of shortening as a result of a reduced rate of subunit loss.

For one state to assemble and the other disassemble, each state energetically must lie on opposite sides of the region where the microtubule switches from net disassembly to net assembly (where v = 0nm/s). By finding those values of free energy along the v = 0 nm/s contour, we can see that there is a maximum total free energy where the assembly rate switches from net assembly to net disassembly ($\Delta G^0_{tot}(v = 0)$) . This contour is approximately linear with a slope equal to negative one, demonstrating that there is an equal trade off between lateral and longitudinal bond free energy for net assembly. To establish a reference point for the energetic states of GTP- and GDP-tubulin, we additionally fit contours to approximate experimental estimates for the rates of growth and rapid shortening *in vitro*. Despite the addition of on-rate penalties for lagging protofilaments, previously estimated values of the lateral and longitudinal bond free energy [33] lie on the growth contour, therefore we use this as the reference point for subsequent analysis. As established previously [33], the separation between the growth and shortening contour yields an estimate for the energy difference between the two states ($\Delta\Delta G^0$, Figure 3.1B). For the *in vitro* parameter set, we find that $\Delta\Delta G^0 = +3.3\ k_B T$ (Figure 3.1B), which is in line with our earlier estimate of +2.5-4.0 $k_B T$ [33].

The preferential assembly bias between GTP- and GDP-tubulin states must arise from an inherent energetic difference ($\Delta\Delta G^0$), such that the total standard Gibbs free energy change of binding (ΔG^0_{tot}) of GDP-tubulin is more positive (less stable) than that of GTP-tubulin for binding to an equivalent site. If the difference between states were due to the on-rate constant (i.e. GDP-tubulin subunits are slower or less efficient to incorporate into the lattice), it would not explain the delay in rapid disassembly after tubulin dilution [96, 97]. Therefore, the difference must

be due to the off-rate (i.e. GDP-tubulin subunits are less stable within the lattice), which is determined by the total interaction energy (Figure 3.1A). It has been proposed that the energy difference is due to lateral bond strain induced by the preferential curled orientation of GDP-tubulin compared to the straight orientation of GTP [3, 33, 34]. Recent evidence from x-ray scattering, however, suggests that GTP-tubulin also has a kinked or curled orientation prior to incorporating into the microtubule lattice [98]. This suggests a model in which the stabilizing effect of GTP tubulin is mediated through the longitudinal contact. Although, it is not clear that this apparent intradimer curling will perturb contacts to the same extent as the pronounced outward curling of protofilaments during disassembly [4, 9, 10]. Recent structural evidence comparing GMPCPP- and GDP-tubulin suggests that strain is induced at the longitudinal interface, rather than the lateral, due to residue compaction upon GTP hydrolysis [91]. In the model here we do not make any assumption about what leads to the energetic difference between GTP and GDP-tubulin, only assume that it exists. For simulation purposes, we place the positive $\Delta\Delta G^0$ on the lateral bond for two reasons. First, it most closely resembles the unfavorable energy contributions in similar models [33, 34]. And second, whether the energetic strain of constraining GDP-tubulin in a straight conformation is experienced through lateral or longitudinal contacts, the existence of the strain depends upon the establishment of lateral bonds. A GDP-tubulin subunit with no lateral bonds will be able to relax into its preferred orientation, thereby relieving strain placed on either the lateral or longitudinal contact. Therefore, placing $\Delta\Delta G^0$ on the lateral bond within the model enforces the lateral contact requirement for the existence of mechanical strain within the microtubule lattice.

3.3.2 Sensitivity of growth and shortening to the underlying kinetic rate constants

Multiple parameters in the model potentially influence the rate of growth and shortening, but it is not clear which, if any, will be the dominant effect. As two of

the defining parameters of dynamic instability, we wanted to examine the sensitivity of growth and shortening states to changes in the rate constant parameters. To see how the assembly surface map shown in Figure 3.1B changes with varying on-rate constant, we examined a horizontal cross-section (black line), through the reference GTP- and GDP-tubulin states, for a range of values. In the model, the off-rate is calculated through the equilibrium constant (K), therefore changes in the on-rate constant parameter value will produce corresponding changes in the off-rate, such that there is no net-effect on ΔG^0_{tot}.

$$K = \frac{k_{on,PF}}{k_{off,PF}} = \exp\left(\frac{-\Delta G^0_{tot}}{k_B T}\right) \tag{3.1}$$

By rearrangement of equation 3.1

$$k_{off,PF} = \frac{k_{on,PF}}{\exp\left(-\Delta G^0_{tot} / k_B T\right)}, \tag{3.2}$$

where

$$\Delta G^0_{tot} = \sum \Delta G^0_{long} + \sum \Delta G^0_{lat} \ . \tag{3.3}$$

For the condition in which the on-rate constant is altered independent of the off-rate (i.e. a capping protein), an x-fold change in the on-rate constant will induce a $\ln(x)$ effect to ΔG^0_{tot} (by equation 3.1 and 3.2). To simulate this case with varying $k_{\text{on,PF}}$, we included the $\ln(x)$ effect of ΔG^0_{tot} on the longitudinal bond such that $k_{\text{off,PF}}$ was maintained to be constant (Figure 3.1C; varying $k_{\text{on,PF}}$ only). Adding the energetic effect of changing $k_{\text{on, PF}}$ to ΔG^0_{long} ensured that it was applied to all subunits within the microtubule lattice. In this case, the rate of growth for microtubules in the growth state (cyan circle) increases for increasing values of $k_{\text{on,PF}}$. By contrast, the shortening rate in the shortening state (red circle) is largely unaffected by changing $k_{\text{on,PF}}$, (i.e. lies on the shortening contour for each value of $k_{\text{on,PF}}$; Figure 3.1C)). The fold-change in the rate of both the growing and shortening states is summarized for a range of values of $k_{\text{on,PF}}$ in Figure 3.1D (varying $k_{\text{on,PF}}$ only; circles). Reduction of $k_{\text{on,PF}}$ results in net disassembly of the reference GTP state, therefore these points do

not appear on the log-log plot in Figure 3.1D. The growth rate is rather sensitive to the on-rate constant such that the x-fold increase in $k_{on,PF}$ results in greater than an x-fold increase in the growth rate. Comparatively, shortening is minimally affected for all values of $k_{on,PF}$ (Figure 3.1D), despite the fact that the total free energy of binding (ΔG^0_{tot}) is changing with $k_{on,PF}$.

An alternative situation is one in which both the on-rate constant and the off-rate are changed coordinately such that ΔG^0_{tot} is maintained at a constant value. This could be accomplished by the induction or enhancement of an energetic barrier between the bound and unbound states [99]. The results of this case are obtained by examining the cross-section through the assembly surface in the absence of a corresponding adjustment to ΔG^0_{tot} (Figure 3.1C; varying $k_{on,PF}$ and $k_{off,PF}$). Here the growth and shortening contours move closer together for increasing values of $k_{on,PF}$, meaning that both the growth and shortening rates of the reference states are affected. As seen in Figure 3.1D (squares), the fold change in the net-rate v of both growth and shortening is linear with respect to the fold change in $k_{on,PF}$, despite a constant value of ΔG^0_{tot}.

Taken together, the above theoretical results show that the growth rate is sensitive to both $k_{on,PF}$ and $k_{off,PF}$, whereas the shortening rate is only sensitive to $k_{off,PF}$. This indicates that shortening is dominated by rapid loss events, which occur much faster than the addition of subunits from solution. Therefore, any microtubule-targeting agent that influences the shortening rate (such is the case for paclitaxel and vinblastine) must influence the energy of interaction at either the lateral or longitudinal interface to stabilize subunits within the lattice, thereby reducing the off-rate.

3.3.3 The free tubulin concentration is a strong predictor of changes to underlying parameters *in vivo*

In a closed system, such as a cell, where the total amount of tubulin is presumably fixed, the free concentration will respond to the changes in the polymer

mass [40, 100], potentially counteracting the effects of $k_{on,PF}$. Because of this, we additionally compared the effects of varying $k_{on,PF}$ to that of varying [*Tub*]. The total number of addition events per unit time is determined by the value of the pseudo-first-order on-rate constant, $k^*_{on,PF}$, where $k^*_{on,PF}$ (in units of $s^{-1}PF^{-1}$) is defined as

$$k^*_{on,PF} = k_{on,PF} \cdot [Tub] \tag{3.4}$$

In the case of varying $k_{on,PF}$ only, the effect of increasing $k_{on,PF}$ increases $k^*_{on,PF}$ independent of $k_{off,PF}$. Because of this, varying [*Tub*] in the model results in the same trends in the assembly surface (Figure 3.2), meaning that the observed trends when varying only $k_{on,PF}$ can be used to inform the trends when varying [*Tub*].

We find that as the value of $k_{on,PF}$ increases, the point at which the varying $k_{on,PF}$ only cross-section intersects with the $v = 0$ contour shifts to more positive values of ΔG^0_{lat} (Figure 3.1C). Because the $v = 0$ contour is linear with a slope of negative one, the shift in ΔG^0_{lat} is equal to the ln(x) adjustment of ΔG^0_{long} (due to the x-fold change in $k_{on,PF}$). This means that the free energy for net assembly ($\Delta G^0_{tot}(v = 0)$) is independent of the on-rate constant for a given value of [*Tub*] (Figure 3.1E; varying $k_{on,PF}$ only). Because varying $k_{on,PF}$ only and varying [*Tub*] result in similar trends, adjusting $k^*_{on,PF}$ via [*Tub*] (such that no adjustment of ΔG^0_{long} is necessary to maintain $k_{off,PF}$) results in an equivalent shift in the intersection with the $v = 0$ contour, meaning that $\Delta G^0_{tot}(v = 0)$ should be adjusted by ln(x). Indeed, we find the change in ΔG^0_{tot} exhibits a logarithmic relationship with respect to $k^*_{on,PF}$, or equivalently [*Tub*] (Figure 3.1E; varying [*Tub*]). Therefore, we can assume that

$$\left[\Delta G^0_{tot}(v = 0) - \Delta G^0_{tot}(v^0 = 0)\right] / k_B T = \ln\left([Tub]/[Tub]^0\right), \tag{3.5}$$

where $\Delta G^0_{tot}(v^0 = 0)$ is the total free energy for net assembly at the reference free tubulin concentration $[Tub]^0$. This relationship, along with the fact that varying $k_{on,PF}$ only and varying [*Tub*] result in equivalent effects to the assembly surface, indicates that changes in [*Tub*] in response to net polymer assembly or disassembly

will counteract any effects of $k_{on,PF}$ in the absence of corresponding effects to $k_{off,PF}$, potentially recovering the original assembly dynamics.

As noted above, the observation of dynamic instability is dependent on the presence of two *distinct* states. Thus, a simple way to eliminate dynamic instability would be to eliminate $\Delta\Delta G^0$ such that the microtubule becomes a single-state polymer, assembling or disassembling as dictated by the total free energy of the resulting single state. In a system with a fixed amount of tubulin, eliminating $\Delta\Delta G^0$ would drive assembly to $v = 0$ at equilibrium through mass action as [*Tub*] responds to the net assembly or disassembly of polymer mass, pushing the system to the critical concentration of the resulting single-state polymer. The predicted trends in the critical concentration with respect to the total free energy are characterized by examining the point where the microtubule switches from net disassembly to net assembly ($\Delta G^0_{tot}(v = 0)$) for each value of [*Tub*] (equation 3.5). From the relationship in equation 3.5, it can be shown that the critical concentration for net assembly is determined by the equilibrium constant for a single protofilament (Appendix A, equation A.4). We note that the critical concentration defined in equation 16 does not account for microtubule nucleation. For this reason, the same relationship may not apply for calculating the critical concentration of initiating growth in solution; however, it will apply to the initiation of growth from a nucleating seed (i.e. of GMPCPP-tubulin).

In the presence of two separate energetic states, $\Delta G^0_{tot}(v = 0)$ will lie somewhere between (e.g. black circle in Figure 3.1B). Elimination of $\Delta\Delta G^0$ and subsequent tubulin mass action towards a new steady state will shift $\Delta G^0_{tot}(v = 0)$ such that it lies on top of the resulting single energetic state. Using the reference points defined in Figure 3.1B as an example, if GDP-tubulin becomes energetically similar to GTP-tubulin, $\Delta G^0_{tot}(v = 0)$ would need to shift by -0.7 k_BT to drive the system to the critical concentration of the GTP-tubulin energetic state. From equation 3.5 and equation A.1, this will result in an exp(-0.7) change in [*Tub*] or ~2-fold reduction. As noted above, some stabilization of the GDP-tubulin state is

necessary to reduce the shortening rate, thus the loss of $\Delta\Delta G^0$ to promote polymer disassembly could be the convergence of the GTP- and GDP-tubulin free energies at a midpoint. This case would result in an exp(0.95) effect or 2.6-fold increase of [*Tub*]. Alternatively, by making GTP-tubulin, energetically identical to GDP-tubulin, there would be a change of $\Delta G^0_{tot}(v = 0)$ by +2.6 k_BT. This would result in an exp(2.6) change in [*Tub*] or ~14-fold increase. In the limit of assembly, it is possible for all tubulin to be in polymer form, such that the free concentration can decrease to near zero. By contrast, the extent of increase in the free concentration will be limited by the amount of polymer to begin with before addition of the perturbing agent (e.g. paclitaxel or vinblastine). Therefore, a 14-fold increase in [*Tub*] may not be possible. Overall, these results indicate that the resulting fold-change in the free concentration *in vivo* in the presence of microtubule-targeting agents provides a strong predictor of any underlying mechanism that results in making GTP- and GDP-tubulin energetically similar.

3.3.4 Dynamic instability is constrained to a narrow region of parameter space

Up until this point we have assumed that switching between states is maintained in order to examine the predicted assembly trends of each state; however, a microtubule will lose dynamic instability if switching between GTP- and GDP-tubulin states is lost. This ability to switch will depend upon the relative ratios of the growth velocity and the hydrolysis rate constant (k_{hyd}). Therefore, we next simulated microtubules with a defined k_{hyd} to determine the sensitivity of dynamic instability to varying model parameters. From the single-state analysis we set $\Delta\Delta G^0$ as the difference between growth and shortening contours (Figure 3.1B). For the parameters used in Figure 3.1B, $\Delta\Delta G^0$ = +3.3 k_BT. Using this value for $\Delta\Delta G^0$, we found that k_{hyd} = 0.2 s^{-1} resulted in dynamic instability (Figure 3.3A), consistent with recent estimates [6]. These base *in vitro* parameters for dynamic

instability are summarized in Table 3.1 and are very similar to those reported previously [6, 33, 34].

We first began by adjusting the bond free energies (ΔG^0_{lat} and ΔG^0_{long}), using the free energy of the GTP-tubulin state as the reference value, and examining the results with regards to the observation of dynamic instability. Before running any simulations, we already know that the region of parameter space where dynamic instability occurs will be subject to two constraints. First, because the GTP-tubulin state undergoes net assembly, its value of ΔG^0_{tot} must be more negative than the value required for net assembly (ΔG^0_{tot}; v = 0 nm/s contour from Figure 3.1B). Second, the value of ΔG^0_{lat} must be within $\Delta\Delta G^0$ of the v = 0 contour. If it is further away, then the value of $\Delta\Delta G^0$ will not permit switching to a state of net disassembly. Thus the reference GTP-tubulin point for dynamic instability will be constrained to a region of parameter space with a slope of negative one and width of $\Delta\Delta G^0$ (shaded region in Figure 3.3B). This fact reiterates the necessity of a non-zero $\Delta\Delta G^0$ for observing dynamic instability. After running the simulations for k_{hyd} = 0.2s^{-1} we see that dynamic instability is constrained even further. Small changes in either ΔG^0_{lat} or ΔG^0_{long} (<1 k_BT) are sufficient to eliminate dynamic instability (Figure 3.3B). In the region of more negative bond free energies (lower left), the microtubule grows continuously without catastrophe. Here, the GTP cap is too large for stochastic fluctuations in cap size to result in catastrophe. In the region of more positive bond free energies (upper right), the microtubule is unable to maintain a GTP cap and therefore cannot grow. Similarly, only small perturbations in k_{hyd} (± 0.2 s^{-1}) are necessary to eliminate dynamic instability at a given point in the 2D parameter space shown in Figure 3.3B. In the limit as k_{hyd} approaches 0s^{-1}, dynamic instability will be lost as the microtubule becomes a single-state polymer, which spends all of the time in the GTP-tubulin state. Additionally, we found that k_{hyd} = 2s^{-1} was sufficient to eliminate dynamic instability because the resulting GTP cap was too small to maintain growth in the region defined by the v = 0 contour and $\Delta\Delta G^0$ above. Since dynamic instability is tightly constrained to a small region of

parameter space, it shows that slightly affecting either bond free energy or k_{hyd} could, in principle, be a viable mechanism for microtubule-targeting agents to eliminate dynamic instability, as each results in the loss of ability to switch between states.

3.3.5 Two potential mechanisms of "kinetic stabilization" consistent with *in vitro* observations

As outlined above, the observation of dynamic instability is sensitive to several individual parameters in the model. Although, it is not clear how large of an effect is necessary and which, if any, will lead to a phenotype consistent with experimental observations. Other than k_{hyd}, the net-effect of each parameter can be summarized by an effect on the rate of association and dissociation of tubulin dimers. The number of association events will depend on the pseudo-first-order on-rate constant, $k^*_{on,PF}$, which is the product of $k_{on,PF}$ and [*Tub*] (equation 4), while dissociation is dictated by the total interaction energy. Although [*Tub*] is a free parameter in the model, we view [*Tub*] as a "reactionary" parameter that responds to changes in the total amount of polymer rather than a direct effect of the microtubule-targeting agent. Varying the [*Tub*] parameter value used in the model, however, is equivalent to varying $k_{on,PF}$ while $k_{off,PF}$ is maintained to be constant (Figure 3.2). Therefore, to adjust $k^*_{on,PF}$ and $k_{off,PF}$ independently, we adjusted the values of [*Tub*] and either ΔG^0_{tot} (via ΔG^0_{long}) or $\Delta\Delta G^0$ used in the simulation. In regions where k_{hyd} is either too fast to maintain a GTP cap or too slow to result in catastrophe, the microtubule will be locked in the GDP- or GTP-tubulin state, respectively. Because of this, the resulting assembly dynamics will be identical to that observed in the case of eliminating $\Delta\Delta G^0$. Therefore, we ignore varying k_{hyd} in subsequent analysis of the model predictions and use the results of varying $\Delta\Delta G^0$ to inform this scenario.

We find that dynamic instability is maintained when $k^*_{on,PF}$ and $k_{off,PF}$ are scaled approximately equal, up to ~10-fold change in both (Figure 3.3C). Larger

decreases result in a "true kinetic stabilization" where dynamic instability is lost and the kinetic rates are reduced by more than an order of magnitude. In regions where scaling factors for $k^*_{on,PF}$ and $k_{off,PF}$ are not equal, the microtubule either grows continuously without catastrophe or cannot maintain any period of growth and therefore rapidly disassembles (Figure 3.3C). Within these regions, growth and shortening obey the observations from the single-state model (Figure 3.1) in that increasing bond stability increases the rate of growth and decreases the rate of shortening. For the majority of observations *in vitro*, paclitaxel reduces the shortening rate with little to no effect on the growth rate in conditions where no net change in polymer mass is detected [84, 101, 102]. Therefore, if paclitaxel inhibits shortening by equally stabilizing both GTP- and GDP-tubulin it must also reduce the on-rate constant in the absence of mass action in order to maintain the growth rate. Vinblastine reduces both growth and shortening *in vitro* [101, 103, 104], therefore must inhibit $k_{on,PF}$ in addition to $k_{off,PF}$ by this true kinetic stabilization mechanism.

The energetic state of GDP-tubulin, and therefore the rate of disassembly, will also be affected by $\Delta\Delta G^0$ (Figure 3.1B). As seen in Figure 3.3D and E, the rate of disassembly is reduced for decreasing values of $\Delta\Delta G^0$, independent of $k^*_{on,PF}$. In both cases of $\Delta\Delta G^0$ minimization, assembly- and disassembly-promoting, regions of near-zero net assembly and loss of dynamic instability appear as $\Delta\Delta G^0$ approaches zero (Figure 3.3D and E). This region represents a "pseudo-kinetic stabilization" where dynamic instability is lost, but the kinetic rates remain comparable to the control values. In the case where GDP-tubulin converges to the energetic state of GTP-tubulin, the growth rate is unaffected by changes in $\Delta\Delta G^0$ for microtubules either exhibiting dynamic instability or growing persistently and the observation of dynamic instability is gradually lost as $\Delta\Delta G^0$ approaches zero (Figure 3.3D). These results are consistent with *in vitro* observations in the presence of paclitaxel and other assembly-promoters in that decreasing $\Delta\Delta G^0$ with constant $k^*_{on,PF}$ will reduce shortening rate and catastrophe frequency, with little effect on the growth rate [101].

In the case where the energetic states of GTP- and GDP-tubulin converge at a mid point (Figure 3.3E), decreasing $\Delta\Delta G^0$ reduces both the growth and shortening rate, a result of destabilization of the GTP-tubulin state and stabilization of the GDP-tubulin state (Figure 3.3E), consistent with experimental observations of vinblastine *in vitro*.

3.3.6 New steady state arises *in vivo* in the presence of paclitaxel and vinblastine

Results thus far have focused on comparing to *in vitro* results, but ultimately we want to understand the mechanisms of kinetic stabilization *in vivo*. To better characterize *in vivo* dynamics in the presence of microtubule-targeting agents we next examined multiple aspects of microtubule dynamics in LLC-PK1 cells stably expressing either EGFP-α-tubulin [105] or EB1-EGFP [106]. To confirm that paclitaxel and vinblastine induce a similar kinetic stabilization phenotype in these cells to that previously reported, we first analyzed the parameters of dynamic instability in the presence of each drug. Consistent with previous findings [85, 101, 107, 108], the addition of either assembly or disassembly promoting agents attenuated microtubule dynamics in both LLC-PK1 cell lines (i.e. induced a "paused" state, Figure 3.4A-C and Figure 3.5). Although, because microtubule-targeting agents increase the amount of time that microtubules spend in an attenuated state, defining growth and shortening, as well as catastrophe and rescue, becomes increasingly difficult and are likely biased towards the control values.

In order to avoid using arbitrary definitions of growth and shortening, we simply recorded the microtubule length displacements by tracking microtubules labeled with EGFP-α-tubulin as previously described [51, 52] for the full duration of imaging. By this analysis method rapid disassembly will give rise to large negative displacements, while growth will give rise to large positive displacements. Additionally, attenuation of dynamics, i.e. increasing time spent in a "paused" state, will increase the frequency of small displacements at the expense of large positive

and negative displacements. Consistent with the expectation of kinetic stabilization, the addition of both paclitaxel and vinblastine significantly reduces the frequency of large displacements, both positive and negative (Figure 3.4D). At 100nM paclitaxel, the length displacement distribution is nearly indistinguishable from fixed microtubules (Figure 3.4D), although kymographs indicate that some dynamics remain (Figure 3.4A-B and Figure 3.5). This is most likely an effect of microtubule-targeting agents promoting blunt microtubule tips compared to control cells (see section 3.3.9 below; Figure 3.9), which modestly increases microtubule tip tracking accuracy by this method [51]. For each treatment, the mean displacement was not different from zero meaning that microtubules, on average, are not biased to net assembly or disassembly *in vivo* (Figure 3.4D inset). This shows that microtubules have reached a new steady state after the addition of microtubule-targeting agents, due to a secondary response of [*Tub*] as a result of simple mass-action kinetics within a system of approximately fixed volume and number of tubulin subunits [40, 100]. Further, the probability of large displacements decreases proportionately for both large positive and large negative values, indicating that the new steady state *in vivo* is the result of effects on both $k^*_{on,PF}$ and $k_{off,PF}$. Therefore, we can focus on regions of near-zero net assembly as indicated in Figure 3.3C-E.

3.3.7 *In vivo* model predictions are consistent with *in vitro* predictions

Other factors such as microtubule-associated depolymerases and polymerases [14], as well as the cell edge can influence microtubule dynamics in a cellular environment, potentially influencing the regime of kinetic stabilization. Therefore, simulation predictions using the *in vitro* parameters do not necessarily reflect the *in vivo* case. For a more accurate comparison to *in vivo* experimental results, we wanted to see if the same *in vitro* model predictions held in a more realistic model for *in vivo* microtubule assembly dynamics as well as determine what parameter changes were necessary to reproduce the experimentally observed non-dynamic

steady state arising after the addition of paclitaxel and vinblastine (Figure 3.4). In order to capture the increased growth rate *in vivo* while maintaining catastrophe, we found it was necessary to add both a growth-promoting (e.g. XMAP215) and catastrophe-promoting effect (e.g. depolymerizing kinesin) to the model (see section 3.5.1), as has been shown for minimally reproducing *in vivo* dynamics in *in vitro* assays [16, 109]. Additionally, we added a compliant cell membrane as a simulation boundary, which could also influence the appearance of dynamic instability. We found that the base parameters shown in Table 3.2 reproduced dynamic instability with similar rates to that estimated experimentally (Figure 3.6A). Some instances of catastrophe away from the cell membrane can be seen (arrows in Figure 3.6A), however, the majority of microtubules grow continuously out to the edge. Once at the edge there are several instances where the microtubule goes through multiple shorter rounds of catastrophe and rescue before finally shortening back to the origin. This is very similar behavior to that observed in experimental microtubule life histories in mammalian cells [110], without implementing it as a constraint for the model. Thus, in the region where dynamic instability is observed, the model reproduces additional features of microtubule assembly *in vivo*.

Similar to the *in vitro* parameter set, the observation of dynamic instability is constrained in parameter space to a region that is narrower than that initially constrained by the $v = 0$ contour and $\Delta\Delta G^0$ (Figure 3.6B). Within this region microtubules with more negative ΔG^0_{long} (lower right) exhibited a higher growth rate compared to those with more negative ΔG^0_{lat} (upper left, Figure 3.6B). Although still tightly constrained, the region of dynamic instability *in vivo* is wider than that of the *in vitro* parameters (~1.5 k_BT versus < 1 k_BT), most likely due to catastrophe promotion by the added kinesins and the cell edge. In the region of more negative bond free energy (lower left), microtubules do not catastrophe and are constrained at the cell membrane. In the region of more positive bond free

energy (upper right), microtubules are unable to maintain growth, similar to the *in vitro* parameter set (Figure 3.3B).

We find that dynamic instability is robust to corresponding fold-decreases in $k^*_{on,PF}$ and $k_{off,PF}$, down to nearly a 100-fold decrease in $k_{off,PF}$. For smaller changes, tubulin mass action in response to polymer assembly or disassembly is predicted to rescue dynamic instability (Figure 3.6C). The number of microtubules and the distance to the cell membrane will limit the amount that the free concentration can respond to polymer assembly, while increasing free concentration will be limited by the amount of tubulin in polymer form in the control case. In regions where the free concentration is unable to recover dynamic instability, microtubules persistently grow against the cell edge or completely disassemble back to the nucleation point (i.e. centrosome), independent of whether the stabilization is applied to the longitudinal or lateral bond (Figure 3.6D). In these regions, microtubules are effectively stabilized and non-dynamic, but rely on the established boundaries. If microtubule-targeting agents rely on these boundaries to eliminate dynamic instability *in vivo*, we predict there should be a significant shift of microtubule plus-ends out to the cell edge or complete loss of microtubule polymer. Inconsistent with this prediction, attenuated dynamics are observed throughout the cell (Figure 3.7) and microtubule polymer remains in the presence of each drug, even at 100nM vinblastine (Figure 3.4A and Figure 3.5A).

To induce true kinetic stabilization using the *in vivo* parameters, greater than 100-fold decrease in $k_{off,PF}$ and 10-fold decrease in $k^*_{on,PF}$ is necessary, equivalent to that predicted using the *in vitro* parameters. The necessary fold-decrease of each is not equivalent because as $k^*_{on,PF}$ decreases relative to k_{hyd}, the microtubule is no longer able to maintain a GTP cap and remains in the less stable GDP-tubulin state (Figure 3.6C). Also consistent with *in vitro* model predictions, reducing the energetic difference between GTP- and GDP-tubulin combined with a modest change (less than an order of magnitude) in $k^*_{on,PF}$, results in a pseudo-kinetic stabilization of the microtubule polymer (Figure 3.6E and F). From equation 3.4 we

note that the fold-change in $k^*_{on,PF}$ in kinetic stabilization case, true and pseudo, could be either a direct effect on the on-rate constant or a result of tubulin mass action. Because microtubules arrive at a new steady state after the addition of microtubule-targeting agents (Figure 3.4), any changes in [*Tub*] should directly reflect the underlying mechanism of action. The model predicts that only a ~2-5-fold change in $k^*_{on,PF}$ is necessary by pseudo-kinetic stabilization (Figure 3.6E-F), while greater than 10-fold reduction is necessary for true kinetic stabilization (Figure 3.6C). If the free concentration change in the presence of paclitaxel or vinblastine is less than 10-fold, it is not sufficient to explain the true kinetic stabilization alone, and therefore the drug must have additional direct effects on the on-rate constant.

3.3.8 Microtubule-targeting agents moderately influence free tubulin and hydrolysis *in vivo*

So far we have described potential mechanisms for kinetic stabilization by paclitaxel and vinblastine, but ultimately we seek to use the model to constrain to a single functional mechanism. As described above, the fold-change in the free tubulin concentration provides an important constraint on the possible mechanism of kinetic stabilization. To estimate free tubulin concentration changes after the addition of microtubule-targeting agents *in vivo*, we bleached a zone containing both microtubule polymer and free tubulin, then measured the fast recovery fraction (within 3s) after bleaching (Figure 3.8A). Because recovery of fluorescence from microtubule polymer requires the microtubule to disassemble and subsequently reassemble through the bleached zone, recovery of polymer signal is very slow compared to the recovery of free tubulin signal by diffusion. Therefore, fast early recovery will be due almost exclusively to free tubulin rather than polymer. Experimentally, we found that the observed changes in [*Tub*] are consistent with paclitaxel and vinblastine's classifications as an assembly-promoter and disassembly-promoter, respectively. Paclitaxel increased the amount of polymer

signal at the expense the free tubulin, resulting in a 2-fold decrease of [*Tub*] at 100nM paclitaxel (Figure 3.8B, dark cyan). Conversely, the addition of vinblastine reduced the amount of microtubule polymer, resulting in an approximately 2-fold increase in [*Tub*] at both 10nM and 100nM (Figure 3.8B, magenta).

The experimentally observed 2-fold change in [*Tub*] in the presence of paclitaxel and vinblastine is quantitatively in agreement with the moderate change predicted in the case for a microtubule-targeting agent that minimizes $\Delta\Delta G^0$ (Figure 3.6D and E). While, in principle, the resulting point of convergence of GTP- and GDP-tubulin could be anywhere in the 2D parameter space with respect to ΔG^0_{long} and ΔG^0_{lat}, the resulting change in [*Tub*] suggests that the total energy of the resulting single state is within $\pm 1 k_B T$ of the maximum free energy for net assembly ($v = 0$ contour) in the control case. Experimental observations of [*Tub*] are not sufficient to explain the greater than 10-fold decrease of $k^*_{on,PF}$ necessary for true kinetic stabilization via uniform stabilization of GTP- and GDP-tubulin, particularly the observed increase in the presence of vinblastine (Figure 3.8B). Therefore, if paclitaxel and vinblastine do not eliminate $\Delta\Delta G^0$, they must directly influence the on-rate constant in addition to stabilizing lateral or longitudinal contacts. As noted above, eliminating $\Delta\Delta G^0$ would be phenotypically similar to increasing or decreasing k_{hyd} such that the growth and shortening states, respectively, cannot be maintained. Therefore, the results could also be consistent with either zero hydrolysis (in the case of paclitaxel) or rapid hydrolysis combined with stabilization of the GDP state (in the case of vinblastine).

To determine if either microtubule-targeting agent influences hydrolysis, we estimated the hydrolysis rate using EB1-EGFP as a reporter for GTP-tubulin, as previously described in these cells [42]. As shown in Figure 3.8C, there was very little effect of either paclitaxel or vinblastine on k_{hyd}. The only significant difference occurred in the presence of 100nM paclitaxel, where k_{hyd} *increased* from $0.8 s^{-1}$ to $1.2 s^{-1}$ (Figure 3.8C, dark cyan). This is the opposite effect predicted for an assembly-promoting agent. Increasing k_{hyd} should promote disassembly rather than

assembly of microtubule polymer, as was observed for 100nM paclitaxel (Figure 3.8B). While we could not detect EB1-EGFP comets in the presence of 100nM vinblastine, this is less likely an effect of hydrolysis as it is a direct consequence of kinetic stabilization and the lack of observable growth periods, as seen in EGFP-α-tubulin kymographs (Figure 3.4A and Figure 3.5A). Additionally, there was no detectable effect on k_{hyd} at either 10nM vinblastine or 10nM paclitaxel (Figure 3.8C), yet effects on dynamics were detectable (Figure 3.4), suggesting that hydrolysis does not play a significant role in kinetic stabilization. It is possible that microtubule-targeting agents inhibit the binding of EB1 to the microtubule lattice through allosteric effects [91]. Inhibition of EB1 binding would decrease the total EB1-EGFP signal at the microtubule end, however, would not influence the decay rate of that signal, which is dependent upon the loss of GTP-tubulin binding sites at the microtubule plus-end and not on the absolute signal level. Therefore, we conclude that the primary mechanism by which paclitaxel and vinblastine inhibit dynamic instability is not dependent upon influencing the GTP hydrolysis rate.

3.3.9 Assembly variance and microtubule tip structure further constrain the mechanisms of paclitaxel and vinblastine

Even though true and pseudo-kinetic stabilization lead to similar net-assembly tendencies, because the underlying kinetic rate constants are much higher in the pseudo-kinetic mechanism, we predict that assembly should be more variable compared to true kinetic stabilization [5]. Therefore, we next examined the variance of microtubule length displacements in time for each condition (Figure 3.9A and B) to attempt to further constrain the mechanisms of kinetic stabilization utilized by paclitaxel and vinblastine. If microtubule assembly is analyzed as diffusion with drift, then the displacement variance is simply the diffusion portion and proportional to the sum of the rates of addition and loss ($k_{on,MT}$ and $k_{off,MT}$, respectively) [5]. Because we did not separate growth and shortening phases in the analysis (in order to eliminate the definition problem mentioned above), switching between phases

will contribute additional variability such that extracting quantitative estimates of $k_{on,MT}$ and $k_{off,MT}$ (as in [5]), particularly in the control case, is difficult. The observed variability can still, however, be quantitatively compared to model predictions. We find that control microtubules are more variable compared to those in the presence of paclitaxel and vinblastine, and that this difference increases with increasing Δt (Figure 3.9A). Assembly variance is dramatically reduced in the presence of 100nM paclitaxel and vinblastine, although, dynamics are still detectable at longer time intervals (Figure 3.9B). Additionally, variability in the presence of paclitaxel rises above that in the presence of vinblastine at longer time intervals. As expected for a purely diffusive process, displacement variance at early time points increases approximately linearly in time. Therefore we fit a line to the first 10s of data for comparison to model predictions (Figure 3.9A and B).

By probing the assembly variance in regions where near-zero net assembly is observed in the model, we can see that only a narrow region of parameter space is consistent with the experimentally observed assembly variance in the presence of paclitaxel and vinblastine (Figure 3.9C-E). In each case, points where dynamic instability was observed exhibited the highest variability, consistent with the control case. Despite reduced kinetic rates, the model predicts there is a region in the true kinetic stabilization case consistent with the higher variability in the presence of paclitaxel compared to vinblastine (Figure 3.9C). For an assembly-promoter, the model predicts that some remaining energy difference between GTP- and GDP-tubulin of ~1k_BT is necessary to reproduce the assembly variance observed for paclitaxel (Figure 3.9D). This is consistent with the kymographs shown in Figure 3.4A and B (see also Figure 3.5), where some evidence for switching between distinguishable assembly states remains even in the presence of 100nM paclitaxel. The comparatively lower variability in the presence of vinblastine pushes the lower limit of that predicted for a pseudo-kinetic mechanism by a disassembly-promoter (Figure 3.9E), as the higher [*Tub*] results in even larger kinetic rates compared to the assembly-promoter case. We note that for both an assembly- and disassembly-

promoter, the predicted fold change of $k^*_{on,PF}$, or equivalently [*Tub*], within the regions that exhibit assembly variability consistent with experimental observations is ~2-fold, equivalent to that estimated experimentally by FRAP (Figure 3.8B).

In addition to assembly variance, higher kinetic rates are also predicted to lead to increased protofilament length variance [5]. We therefore next analyzed the model predicted distribution of individual protofilament lengths in the regions defined in Figure 3.9C-E for each microtubule-targeting agent. Surprisingly, microtubules stabilized by a pseudo-kinetic mechanism showed markedly more blunt tips compared to those stabilized by a true kinetic mechanism (Figure 3.9F), although, this result is specific to the placement of the stabilization effect (reducing $k_{off,PF}$) on the longitudinal bond. Microtubule tips are primarily blunt if the stabilization effect is placed on the lateral bond (Figure 3.9F). The assignment of the stabilization effect on the lateral or longitudinal bond does not significantly influence the net-rate or the assembly variance, however (Figure 3.10). While both paclitaxel and vinblastine promote blunt microtubule tips experimentally, tips remain more tapered in the presence vinblastine (Figure 3.9G). This is despite the fact that periods of microtubule growth, which should promote tapering [5, 6], were observed in the presence of paclitaxel but not vinblastine at 100nM (Figure 3.4). Experimental estimates of the protofilament distribution are greater than those predicted by the model, although are potentially increased by artifacts such as inhomogeneity of background fluorescence of free tubulin in the cytoplasm. Qualitatively, however, the model predicts that the only way for microtubule tips to be more tapered in the presence of vinblastine compared to paclitaxel is if vinblastine stabilizes the longitudinal bond in a true kinetic stabilization mechanism. Thus, paclitaxel is constrained to stabilize through a pseudo-kinetic mechanism or stabilize the lateral bond in a true kinetic stabilization mechanism.

3.4 Discussion

Results from the computational model for microtubule dynamic instability employed in this study indicate there are multiple pathways that can in principle lead to the loss of dynamic instability or kinetic stabilization. Of these, only two are consistent with *in vivo* experimental results. First, uniform stabilization of both GTP- and GDP-tubulin in the lattice combined with on-rate constant inhibition leads to a "true kinetic stabilization" where the kinetic rate constants are reduced by several orders of magnitude. Second, reduction of the energetic difference between GTP- and GDP-tubulin and subsequent mass action of free tubulin in response to net polymer assembly or disassembly induced by the primary effects of the microtubule-targeting agent leads to a "pseudo-kinetic stabilization" of the resulting single state polymer.

While these two mechanisms initially seem very different, the unifying factor is that they eliminate the inherent difference between the GTP- and GDP-tubulin states. Whereas pseudo-kinetic stabilization results from energetic or thermodynamic convergence between the two states, true kinetic stabilization is a result of convergence between the two states kinetically toward very low on-off rates. Thus, the answer to how microtubule-targeting agents with *opposite* effects on net polymer assembly lead to the *same* experimental phenotype is that they eliminate the detectable differences between GTP- and GDP-tubulin, thereby violating one of the defining characteristics of dynamic instability as outlined by Mitchison and Kirschner [1].

3.4.1 On the mechanisms of paclitaxel and vinblastine

While we cannot definitively rule out either mechanism for paclitaxel based solely on the experimental evidence provided here, previous findings indicate that paclitaxel most likely functions by pseudo-kinetic stabilization, i.e. it causes GDP-tubulin to be energetically similar to GTP-tubulin, leading to an approximately

single state polymer. First, the experimentally observed ~2-fold decrease of [*Tub*] in the presence of paclitaxel reported here (Figure 3.8B) is too small to kinetically stabilize the microtubule by a true kinetic stabilization mechanism. Therefore an additional decrease of the on-rate constant is necessary. This additional decrease of the on-rate constant should lead to a decrease in the growth rate *in vitro* (Figure 3.1), although could be maintained by unequal effects on $k_{on,PF}$ and $k_{off,PF}$ (Figure 3.3C). An effect on the growth rate *in vitro* is only observed at high concentrations of paclitaxel where polymer levels are increased [84]. When the mass action effects are minimized *in vitro* by using a large reservoir of free tubulin, paclitaxel does not influence the growth rate [101] suggesting that the kinetics and thermodynamics of the GTP-tubulin state are maintained in the presence of paclitaxel, as slight modification of either will have significant consequences on the rates of each state (Figure 3.1). Additionally, paclitaxel induces the *de novo* formation of microtubules from GDP-tubulin at a similar rate as the addition of GTP, suggesting that it induces an assembly-competent thermodynamic state of GDP-tubulin that is similar to GTP-tubulin [111]. Further, the pseudo kinetic stabilization mechanism is consistent with recent structural evidence that paclitaxel induces a GTP-like structure in GDP-tubulin [91]. It is still possible that paclitaxel or other assembly-promoting microtubule-targeting agents binding to the taxane site stabilize the lateral contacts between protofilaments [11, 27, 82], although, this stabilizing effect would have to be specific to GDP- over GTP-tubulin as stabilization of GTP-tubulin lateral contacts would increase the growth rate (Figure 3.1), which is not observed experimentally (Figure 3.4C). Therefore, we conclude that paclitaxel stabilizes microtubules through a pseudo-kinetic stabilization mechanism, making GDP-tubulin energetically similar to GTP-tubulin.

Because of its binding location near the longitudinal interface on β-tubulin [26], vinblastine and other vinca domain binders are particularly well suited to induce steric hindrance, thereby reducing the on-rate constant. Combined with the observation of increased tubulin self-association in the presence of vinblastine [93]

would result in a mechanism consistent with true kinetic stabilization. Structural evidence suggests that vinblastine may crosslink contacts at the interdimer longitudinal interface [26, 94], consistent with the longitudinal bond stabilization predicted by the model to produce the increased microtubule tip taper compared to paclitaxel (Figure 3.9G). Additionally, a true kinetic stabilization mechanism is supported by findings that subunit incorporation and dissociation are both reduced in the presence of vinblastine [112], although, the observed reductions are much smaller than we predict is necessary for this mechanism. Despite stabilization of the longitudinal bond, true kinetic stabilization would result in a reduced rate of both growth and shortening, as observed *in vitro* [101, 103, 104] and *in vivo* [101, 108] in the presence of vinblastine. Thus, the model-predicted true kinetic stabilization mechanism of vinblastine is consistent with previous experimental findings as well as the *in vivo* experimental results outlined in this study. Therefore, it is reasonable to conclude that vinblastine kinetically stabilizes microtubules by inhibiting subunit association and stabilizing the longitudinal bond.

3.4.2 Comparison to microtubule-associated proteins

Microtubule-targeting agents are successful chemotherapeutic agents due to their ability to attenuate microtubule dynamics. Microtubule-associated proteins (MAPs), on the other hand, typically enhance microtubule dynamics, such that the combination of MAPs can reproduce *in vivo*-like dynamics *in vitro* [16, 109]. As seen in Figure 3.3B and 3.6B, dynamic instability is maintained by the tradeoff between lateral and longitudinal bond free energy. Within this region of dynamic instability, microtubules with stronger longitudinal bonds relative to lateral bonds grow faster. Because of the stronger longitudinal bond and faster growth rates, microtubule ends are likely to taper more quickly, potentially resulting in a higher frequency of catastrophe [6]. Therefore, by altering the ratio of the bond strengths, MAPs could influence both the rate during periods of growth as well as the transition frequency between states. Alternatively, as we discussed above,

microtubule dynamics *in vivo* are predicted to be robust to small perturbations (± $2k_BT$) in the bond free energies due to mass action of tubulin between polymer and solution, although, the resulting steady state dynamics will almost certainly differ compared to the original state. Bond stabilization, with subsequent mass action recovering dynamic instability, should reduce dynamics due to the reduction of both $k^*_{on,PF}$ and $k_{off,PF}$, while bond destabilization would increase dynamics (Figure 3.6C). Compared to the mechanisms of kinetic stabilization, these potential MAP effects maintain the inherent difference between GTP- and GDP-tubulin and are relatively modest effects. Because of the rapid nature of addition and loss events at the microtubule end, even *in vitro*, a modest effect, particularly on the off-rate can have significant consequences for assembly dynamics (32; Figure 3.1).

3.4.3 Implications for treated cells and application to future drug design

If the cumulative and primary consequence of microtubule-targeting drugs is inhibition of cell proliferation, then it appears that a true kinetic stabilization mechanism would be more potent than pseudo-kinetic stabilization. Because the on-rate constant is significantly reduced in the true kinetic stabilization case, assembly of any form of a mitotic spindle would be slow and difficult, therefore reducing the chance that cells are ultimately able to complete division. Comparatively, spindle assembly would be retained in the pseudo-kinetic stabilization case, as net disassembly of microtubules at the onset of mitosis would increase the free tubulin concentration [113]. Despite retaining the ability to form a spindle in this case, the loss of dynamic instability would perturb spindle reorganization and correction of kinetochore attachment errors. Thus, utilization of a pseudo-kinetic mechanism could potentially explain the observation that paclitaxel treatment at low concentrations results in multipolar spindles and chromosome missegregation rather than mitotic arrest [114].

We note that there are, in principle, alternative mechanisms that are predicted to eliminate microtubule dynamic instability. For example, a large (greater than 10-fold) stabilization or destabilization effect, such that mass action is not able to recover dynamic instability, would result in persistent growth against the cell membrane or complete disassembly of microtubules (Figure 3.6C and D). As noted above, these scenarios will lead to a significant shift in the distribution of microtubule plus-ends in not only mitotic cells, but interphase cells as well. Therefore, it is reasonable to believe that this type of mechanism would result in greater toxicity to healthy cells compared to a mechanism in which the microtubule array is maintained in the absence of dynamic instability. Attenuation of dynamics without perturbing the plus-end distribution could be a potential way to specifically target mitotic cells, when untreated microtubules exhibit increased dynamics compared to interphase cells. Persistent microtubule growth may alternatively be desirable in additional applications for microtubule-targeting agents, for example in axon regeneration after injury [19, 20]. The observations and model predictions described in this study can be used as a guide to develop drug screening assays for the detection of microtubule-directed agents that utilize a specific mechanism that will be most potent for a given application.

3.5 Methods

3.5.1 Model description for *in vitro* and *in vivo* microtubule assembly dynamics

All simulations were run in MATLAB R2012b or R2013a (The MathWorks, Inc) using a pseudomechanical model for microtubule assembly as previously described [33], with added on-rate penalties of $\sigma_1 = 2$ and $\sigma_2 = 10$ to protofilaments where one or two neighboring protofilaments were longer by at least one dimer length, respectively [90]. This scaled on-rate constant was also used in calculation of the off-rate (equation 2), based on the type of site created by unbinding or

equivalently the number of lateral bonds, such that the equilibrium constant remained fixed. Microtubules were initialized with a length of 400 tubulin dimers and a GTP cap size of 4 dimer layers. After each event step, if a microtubule shortened to less than 100nm in length, it was reinitialized as 13 dimer layers of GTP-tubulin, thus serving as a seed to potentially initiate new microtubule growth. Base *in vitro* parameters for examining the effects of microtubule-targeting agents are listed in Table 3.1.

Modifications were made to the model for *in vivo* microtubule assembly (Figure 3.6A), based on the following arguments, to account for the cellular environment, increased growth rate *in vivo* compared to *in vitro*, and to promote catastrophe.

1. A 5-fold increase in the on-rate constant was included to account for the estimated effects of macromolecular crowding in a cellular environment [115].
2. Within the region where dynamic instability is observed, microtubules with stronger longitudinal bonds relative to lateral bonds grow faster (lower right, Figure 3.3B and Figure 3.6B). Thus, a stronger longitudinal (-0.8 k_BT) and weaker (+0.7 k_BT) lateral bond was used to achieve a growth rate closer to that estimated *in vivo*. This is a similar effect to that previously predicted for XMAP215 [34].
3. Because of the increased growth rate *in vivo*, microtubules have large caps compared to *in vitro* [42]. The experimentally estimated value of $k_{hyd} = 0.8s^{-1}$ reproduced this large cap, but catastrophe was no longer observed in the model. Increasing k_{hyd} to $2s^{-1}$ could reproduce catastrophe; however, caps were significantly reduced in size, closer to those observed with *in vitro* parameters (Figure 3.3C). It has been suggested that cells may use catastrophe factors to promote catastrophe at high growth rates [96]. Additionally, adding both a growth promoter and catastrophe promoter to *in vitro* assays reproduces *in vivo* like dynamics [16, 109]. Having already

accounted for a growth promoter (number 2 above), we added the effects of kinesin motors in order to reproduce catastrophe at the experimentally estimated value of k_{hyd}. Parameters for the kinesin motors can be found in Table 3.2. Individual motors were modeled similar to that previously described for a kinking motor [6]. Briefly, motors diffuse along the microtubule lattice, bound between the microtubule ends such that only motors determined to have detached could leave the lattice. GTP-tubulin subunits associated with a motor were treated as GDP-tubulin. If a motor was attached to a dissociating subunit, then the motor was moved to the adjacent, more proximal subunit (towards minus-end). Motor attachment, detachment, or step size of bound motors was calculated based on the event time after each tubulin event step (addition, loss, or hydrolysis). Only one motor was allowed to attach per time step.

4. A compliant barrier was added to capture the effects of the cell edge on resulting microtubule dynamics. Assembly against the cell membrane was implemented similar to assembly under load described in [41]. As the microtubule approaches the membrane, the probability (p_i) that a dimer can add to the end of the i^{th} protofilament depends on the distance from membrane and its compliance, such that

$$p_i = 1 - \int_{-\infty}^{L_{PF,i}+L_d} f(x)dx \,, \tag{3.6}$$

where $L_{PF,i}$ is the length of the i^{th} protofilament, L_d is the length of a single tubulin dimer (8 nm), and $f(x)$ is the probability density function for the position of the cell membrane. We assumed the membrane has a Gaussian probability density function with mean $\mu = x_{cell}$ and variance $\sigma^2 = k_B T/\kappa_{cell}$. The probability of addition is used to scale the pseudo-first-order on-rate constant ($k^*_{on,PF}$), such that

$$k^*_{on,i} = k_{on,i} \cdot [Tub] \cdot p_i \tag{3.7}$$

From this, the association event time for the i^{th} protofilament (t_i) is calculated as

$$t_i = \frac{-\ln(rand)}{k^*_{on,i}}, \tag{3.8}$$

where *rand* is a uniformly distributed random number between 0 and 1, and then handled as described in [33].

3.5.2 Analysis of simulation output

Single-state microtubule simulations were run for a total of 10,000 events (addition and loss). Net-rate was estimated by linear best fit to the mean protofilament length versus time, averaged across 10 microtubules. For all dual-state simulations the mean protofilament length was recorded every 10ms of simulation time for a total of either 6mins or 4mins for *in vitro* and *in vivo* parameter sets, respectively. Unless otherwise noted, only a single microtubule trajectory was simulated for each point in parameter space. Resulting length versus time model output was run through an automated analysis in order to determine if the microtubule exhibited dynamic instability, as well as calculate the growth and shortening rates. Length and time were sampled at fine and coarse intervals of 0.01s and 1 s, respectively. Directional changes were initially determined from the coarse samples as points where the length displacement between sample intervals switched from positive to negative, or vice versa. The resulting direction change instances were then further refined via fitting a line to 5s of fine sampled data before and after the instance in question. If the sign of the slope of each line (positive or negative) was equal, the instance was eliminated as a true direction change. If the signs were opposite, then the instance was retained as a directional change. Growth (positive) or shortening (negative) excursions were calculated as the microtubule length displacement between points of directional change. Dynamic instability was defined by the observation of at least one positive excursion greater than 500 nm and one negative excursion less than -500 nm.

Growth rates were calculated by fitting a line to the coarse sampled data within an individual excursion. Unless a microtubule exhibited dynamic instability, periods where the microtubule was within 500nm of the boundaries (either cell membrane or nucleating seed) were eliminated from analysis for both *in vitro* and *in vivo* parameter sets.

Protofilament length standard deviation (σ_{PF}) was calculated from the fine sampled model output. For each microtubule simulated, the protofilament length standard deviation was weighted by the duration of the time step according to

$$\left\langle \sigma_{PF} \right\rangle = \frac{\sum_{i=1}^{n-1} \sigma_{PF,i} \cdot \left(t_{i+1} - t_i \right)}{t_n}, \tag{3.9}$$

where n is the total number of sampled time points. The result was then averaged across 10 separate simulation trajectories. No weighting was performed in calculating the cumulative density of protofilament length standard deviations.

3.5.3 Cell culture and microtubule-targeting agent stocks solutions

LLC-PK1 cells stably expressing EGFP-α-tubulin (LLC-PK1α; [105]) or EB1-EGFP (EB1/GFP-3; [106]) were cultured in Gibco® Opti-MEM® media (Invitrogen Corporation, Carlsbad, CA, USA) containing 10% fetal bovine serum, and were frozen down and stored in cryovials in liquid nitrogen prior to plating. Cells were removed from cryovials, plated at 50,000 cells per dish in MatTek 35mm No. 1.5 dishes (MatTek Corporation, Ashland, MA, USA), and incubated at 37°C in 5% CO_2 approximately 24 hours prior to imaging. LLC-PK1α cells were fixed in PHEM buffer (60mM Pipes, 25mM HEPES, 5mM EGTA, and 1mM MgCl) containing 0.25% glutaraldehyde, 3.7% paraformaldehyde, 3.7% sucrose, and 0.1% Triton X-100, as previously described [39, 51].

Paclitaxel (Sigma-Aldrich Corporation, St. Louis, MO, USA) was stored as a 500 μM stock solution in dimethyl-sulfoxide (DMSO) at -20°C. Vinblastine sulfate (Sigma-Aldrich) was stored as a 100 μM stock solution in DMSO at -20°C. Drug

stocks were thawed and diluted to 2x working concentration in cell culture media, then heated to 37°C before media exchange. For exchange, half of the cell culture media in dishes was replaced with drug-containing media 30 minutes prior to the onset of imaging. In control experiments, an equivalent volume of DMSO was added to cell culture dishes. Final amount of DMSO did not exceed 1% in any conditions.

3.5.4 Microtubule dynamics measurements

Timelapse image sequences were acquired using a Nikon TE200 epifluorescence inverted microscope (Nikon Instruments Inc., Melville, NY, USA) equipped with a Ludl BioPrecision stage (Ludl Electronic Products, Ltd., Hawthorne, NY, USA) under control of MetaMorph v7.4 imaging software (Molecular Devices LLC, Sunnyvale, CA, USA). Images were acquired through a 60x 1.49 NA Plan Apo TIRF objective with a 2.5x intermediate projection lens (150x total magnification) using a Photometrics CoolSnap HQ^2 CCD camera (Photometrics, Tuscon, AZ, USA), giving a final image pixel size of 42 nm. A PhotoFluor II® metal halide light source (89 North, Burlington, VT, USA) and an ET-EGFP filter set (49002; Chroma Technology Corporation, Bellows Falls, VT, USA) were used for single-channel GFP imaging. Images for microtubule dynamics measurements were acquired at 1-second intervals for 1 minute with 100% illuminator power and 200ms exposure time. Images for estimating hydrolysis rate were acquired streaming at 100ms intervals for 20s. The stage and objective were heated to 37°C for the duration of imaging.

Microtubule growth rates and catastrophe frequencies were obtained from timelapse images of EB1/GFP-3 cells, using the MetaMorph kymograph tool to generate maximum intensity plots within a user-specified region of interest. Growth lengths, times, and velocities for individual microtubules were extracted by clicking on the pixel immediately in front of the brightest part of an EB1 comet in the first and last frames of each growth phase. Instances where the net growth length was

<500 nm were not counted, and instances where the EB1 comet disappeared and reappeared in subsequent frames without an apparent shortening event were counted as multiple growth events. Catastrophe frequency was calculated by dividing the total number of EB1 comets analyzed by the sum of the growth times.

Microtubule shortening rates and rescue frequencies were obtained from timelapse images of LLC-PK1α cells, using the MetaMorph kymograph tool, as described above. Shortening event lengths, times, and velocities for individual microtubules were extracted by clicking on the pixel immediately in front of the brightest pixel at the microtubule tip in the frame immediately preceding a shortening event and at the last frame of an event. Instances where the net shortening length was <500 nm were not counted. Rescue frequency was calculated by dividing the total number of microtubules analyzed by the sum of the shortening time. Microtubule length displacements and protofilament length standard deviation were estimated by error function fitting of the fluorescence intensity along the microtubule axis using the TipTracker software as described in [51, 52], without modification. Occasionally, transport (i.e. microtubule buckling or other net motion of the polymer lattice) was observed by motion of the fluorescent speckle pattern along the microtubule lattice, distal to the tip, as previously reported in these cells [116]. Events in which tip motion occurred concurrently with a transport event were not included in the analysis.

The hydrolysis rate was estimated as described previously [42], via fitting an exponential decay to function to the EB1-EGFP fluorescence intensity decay along the microtubule lattice. Fluorescence intensity values for fitting were selected from columns (along the time axis) of background subtracted EB1-EGFP kymographs and normalized to the maximum value. Points for fitting were initiated at the first pixel after the maximum and terminated at the time point of catastrophe or the end of acquisition. A minimum of 20 points (2s of data) was required for fitting.

3.5.5 Estimating tubulin monomer-to-polymer ratios

Fluorescence recovery after photobleaching (FRAP) experiments were performed in the LLC-PK1α cell line using a Zeiss LSM7 LIVE laser scanning swept-field confocal microscope (Carl Zeiss Microscopy, Jena, Germany) with an Alpha Plan-Fluar 100x/1.45 NA objective and a 12-bit linear CCD detector. Image stacks were acquired at 1.0x optovar magnification, using a 100 mW 488 nm diode laser line at 10% power with an acquisition rate of 33 ms per scan (47.4 μs pixel dwell time) for 120 frames. After the first 10 frames, a 25 pixel (1.58 μm) wide lane was bleached across the centrosome (identified by the brightest pixel) to the cell periphery using the 488 nm laser line at 100% power (0.493 s total bleach time), after which fluorescence signal was allowed to recover for the remaining 110 frames of imaging. The bleach region was continuously scanned during the bleach time in order to minimize diffusional recovery during the bleach period. The stage and objective were heated to 37°C for the duration of imaging.

Average GFP fluorescence signal within the bleached region was measured at each frame of the image stack using the ImageJ MultiMeasure tool. A 20-pixel tall rectangular region was drawn over the bleach area. The width of this region was dependent on the width of the cell, and was drawn such that it would not extend into the nucleus or cell edge. Signal intensities for frames 10-120 were then normalized to the signal in the 10th frame in the stack (the last frame prior to bleaching). These frames were chosen because GFP photobleaching curves in these frames approximate a linear decay, while a strong nonlinear fluorescence loss is noted in the first ~9 frames. To provide an experimental estimate of the fluorescence loss due to imaging, the experiment was repeated without the photobleaching event and normalized fluorescence intensities were recorded for similar regions in these cells. This ‘bleach correction factor’ was determined for each group, with 5 cells per analysis.

New normalized fluorescence intensities were determined for frames 10-120 by the following formula:

$$I_N(t) = \frac{I_{bleach}(t)}{I_{corr}(t)} \tag{3.10}$$

where $I_{bleach}(t)$ is the average normalized fluorescence intensity within the bleached lane at time t, $I_{corr}(t)$ is the average normalized bleach correction factor intensity at time t, and $I_N(t)$ is the new, corrected fluorescence intensity at time t. Monomer and polymer fraction were calculated as

$$F_{monomer} = \frac{I_N(t_{end}) - I_N(t_{post})}{I_N(t_{pre}) - I_N(t_{post})} \tag{3.11}$$

$$F_{polymer} = 1 - F_{monomer} \tag{3.12}$$

where I_N are corrected, normalized fluorescence intensities, t_{pre} is the last frame pre-bleach, t_{post} is the first frame post-bleach, and t_{end} is the final frame of the image sequence.

3.5.6 Statistical analysis

Comparisons between experimental conditions were performed by one-way ANOVA and Tukey-Kramer multiple comparisons method using the *anova1* and *multcompare* functions in MATLAB R2013a. Standard error of the microtubule length displacement statistics was estimated using a bootstrapping method. Briefly, a new distribution of equal size was sampled with replacement from the original for 1000 separate instances. Each statistic was calculated from the resulting resamples in order to construct a 95% confidence interval, from which the standard error was calculated assuming a normally distributed population.

3.6 Acknowledgements

The authors would like to thank Pat Wadsworth (University of Massachusetts Amherst) and Lynne Cassimeris (Lehigh University) for LLC-PK1 cell lines. Simulations were carried out in part through use of computing resources at the University of Minnesota Supercomputing Institute. BTC performed all

computational simulations and analysis. BTC and DJO designed experiments, while BTC, LSP, and JB collected and analyzed experimental data. BTC, LSP, and DJO wrote the manuscript. BTC was supported by NIH fellowship T32 EB008389. LSP was supported by a 3M Science & Technology Doctoral Fellowship through the University of Minnesota. The research was supported by R01 GM076177 and R01 GM071522 to DJO.

3.7 Tables and Figures

TABLE 3.1 *In vitro* simulation base parameters for dynamic instability

Symbol	Parameter	Value	Reference
ΔG^0_{lat}	Lateral bond free energy	-5.7 k_BT	[5, 6, 33, 34]
ΔG^0_{long}	Longitudinal bond free energy	-7.2 k_BT	[5, 6]
$\Delta\Delta G^0$	Energetic penalty of GDP-tubulin	+3.3 k_BT	Model fit
$[Tub]$	Free tubulin concentration	5.6 μM	[5, 41]
$k_{\text{on,PF}}$	On-rate constant	6 $s^{-1}\mu M^{-1}PF^{-1}$	[5]
k_{hyd}	Hydrolysis rate constant	0.2 s^{-1}	Model constrained; [6]
σ_1	One-neighbor on-rate penalty	2	[90]
σ_2	Two-neighbor on-rate penalty	10	[90]

TABLE 3.2 *In vivo* simulation base parameters for dynamic instability

Symbol	Parameter	Value	Reference
ΔG^0_{lat}	Lateral bond free energy	-5.0 k_BT	Fit to experimental data
ΔG^0_{long}	Longitudinal bond free energy	-8.0 k_BT	Fit to experimental data
$\Delta\Delta G^0$	Energetic penalty of GDP-tubulin	+3.6 k_BT	Model fit
$[Tub]$	Free tubulin concentration	7 μM	[42]
$k_{\text{on,PF}}$	On-rate constant	30 $s^{-1}\mu M^{-1}PF^{-1}$	Fit to experimental data
k_{hyd}	Hydrolysis rate constant	0.8 s^{-1}	Experimental estimate
σ_1	One-neighbor on-rate penalty	2	[90]
σ_2	Two-neighbor on-rate penalty	10	[90]
D_{k}	Kinesin motor diffusion coefficient	0.38 $\mu m^2 s^{-1}$	[6, 117]
$[Kin]$	Motor concentration	5 nM	
$k_{\text{on,k}}$	Kinesin on-rate constant	0.6 $\mu m^{-1} nM^{-1} s^{-1}$	[117]
$k_{\text{off,k}}$	Kinesin off-rate	2 s^{-1}	[117]
x_{cell}	Cell membrane mean position	10 μm	Experimental data
κ_{cell}	Cell membrane stiffness	500 pN/μm	[118]

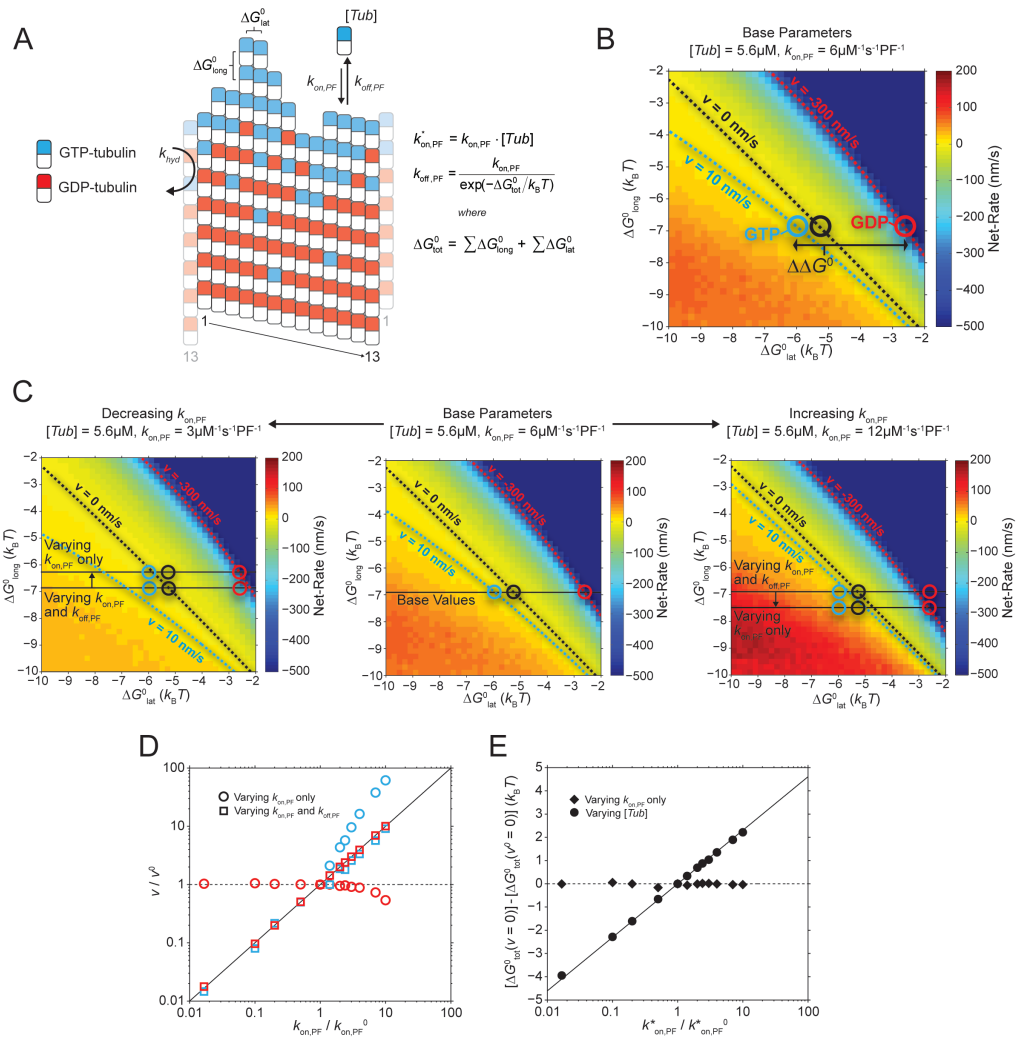

FIGURE 3.1 Establishing the general requirements of dynamic instability using a single-state model

A) Model for microtubule assembly. B) Microtubule net assembly rate for varying lateral (ΔG^0_{lat}) and longitudinal (ΔG^0_{long}) bond free energy ($k_{on,PF}$ = 6μM^{-1}s^{-1}PF^{-1} and [*Tub*] = 5.6μM; contours best-fit by a polynomial). Cyan, red, and black circles denote the reference points for GTP, GDP, and $\Delta G^0_{tot}(v = 0)$, respectively. C) Comparison of assembly heat maps for varying values of $k_{on,PF}$. Left: $k_{on,PF}$ = 3μM^{-1}s^{-1}PF^{-1}, Middle: $k_{on,PF}$ = 6μM^{-1}s^{-1}PF^{-1}, and Right: $k_{on,PF}$ = 12μM^{-1}s^{-1}PF^{-1}. Horizontal lines represent the cross-section used in analysis of both varying and constant $k_{off,PF}$. D) Fold-change in net-rate for the growth (cyan) and shortening states (red) versus the fold-change in $k_{on,PF}$, where $k_{off,PF}$ is held constant (circles) or varies with $k_{on,PF}$ (squares). Solid line is the diagonal with slope equal to one, where the fold-change in net-rate is equal to the fold-change in $k_{on,PF}$. Dotted line marks zero. E) Shift in the total bond free energy where the net-rate is zero ($\Delta G^0_{tot}(v$ = 0nm/s)) versus the fold-change in $k^*_{on,PF}$, implemented either via $k_{on,PF}$ or [*Tub*]. Solid line is $\ln(k^*_{on,PF}/k^*_{on,PF}{}^0)$ while dotted line marks zero. In both D and E, the values for normalization are from the base parameters stated in B.

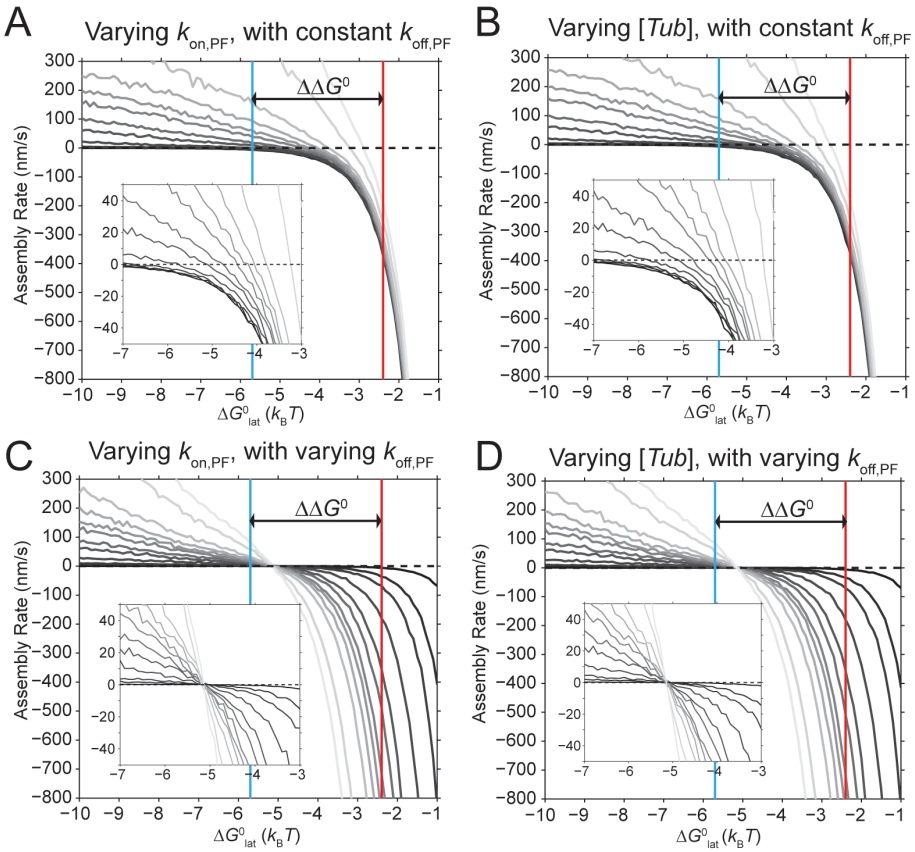

FIGURE 3.2 Comparing the methods of implementing on-rate constant effects with either constant or varying off-rate.
Horizontal cross-sections at $\Delta G^0_{long} = -6.8 k_B T$ of comparable heat maps to those shown in Figure 3.1C with varying values of $k^*_{on,PF}$ (0.5, 3.0, 6.0, 15, 30, 42, 60, 72, 90, 120, 210, and 300 $s^{-1}PF^{-1}$, in order of increasing brightness). In A and B the off-rate is held constant for varying values of the on-rate constant. In C and D the off-rate is adjusted equivalently to the on-rate constant. A) Implementation via $k_{on,PF}$ with additional adjustment to ΔG^0_{tot}. B) On-rate constant effect is implemented through [*Tub*] alone. C) Varying $k_{on,PF}$ in the absence of additional parameter adjustments. D) [*Tub*] is varied with a corresponding adjustment to ΔG^0_{tot} such that the off-rate is equally adjusted. Cyan and red lines represent the intersection with the growth and shortening contours shown in Figure 3.1B. Dotted line marks zero.

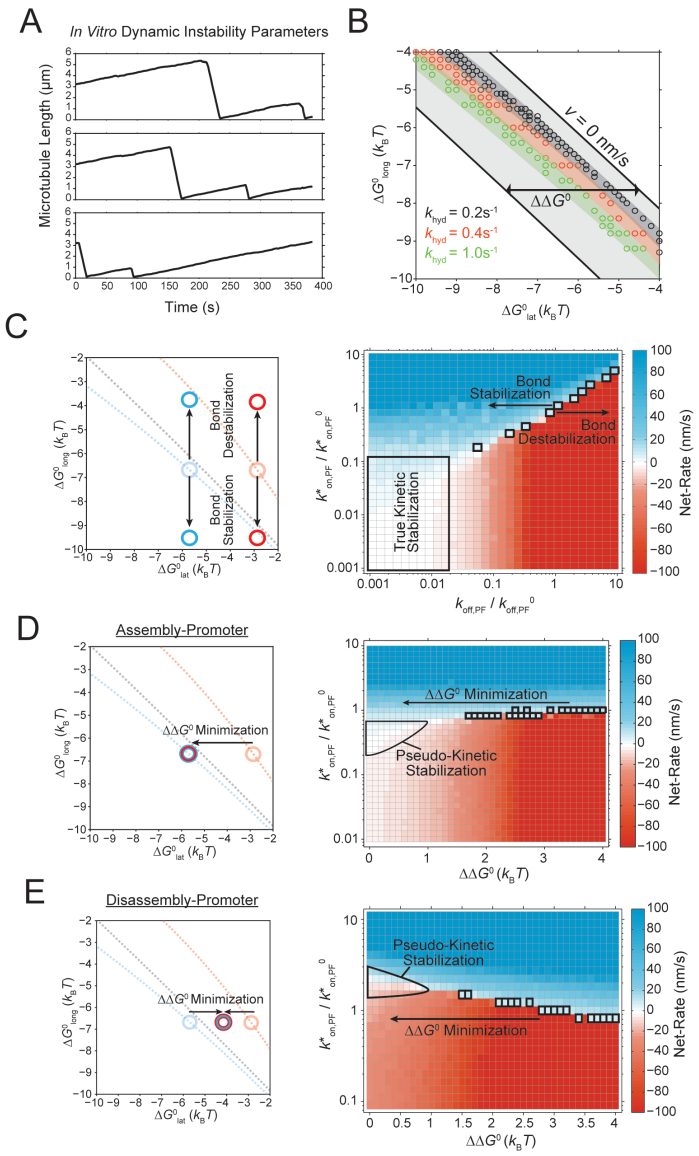

FIGURE 3.3 Dynamic instability is constrained to a narrow region of parameter space
A) Representative microtubule length versus time traces for the *in vitro* dynamic instability parameters listed in Table 3.1. B) Black, red, and green circles represent the GTP-tubulin energetic states from individual simulations where dynamic instability was observed for k_{hyd} = 0.2, 0.4, and 1.0s^{-1}, respectively. Colored areas represent a general fit to where dynamic instability was observed for each value of k_{hyd}. The region constrained by the v = 0 contour and $\Delta\Delta G^0$ is shaded in gray for reference. C) Stabilization and destabilization due to uniform effects on both GTP- and GDP-tubulin versus varying $k^*_{on,PF}$. D) Minimization of $\Delta\Delta G^0$ by an assembly-promoter versus varying $k^*_{on,PF}$. In this case, the energetic state of GDP-tubulin converges to the energetic state of GTP-tubulin. E) Minimization of $\Delta\Delta G^0$ by a disassembly-promoter versus $k^*_{on,PF}$. In this case, the energetic states of GTP- and GDP-tubulin converge to a midpoint between the two. Points where dynamic instability was observed are marked with a bold bounding box. For these points, the rate reported is the average growth rate during rounds of dynamic instability.

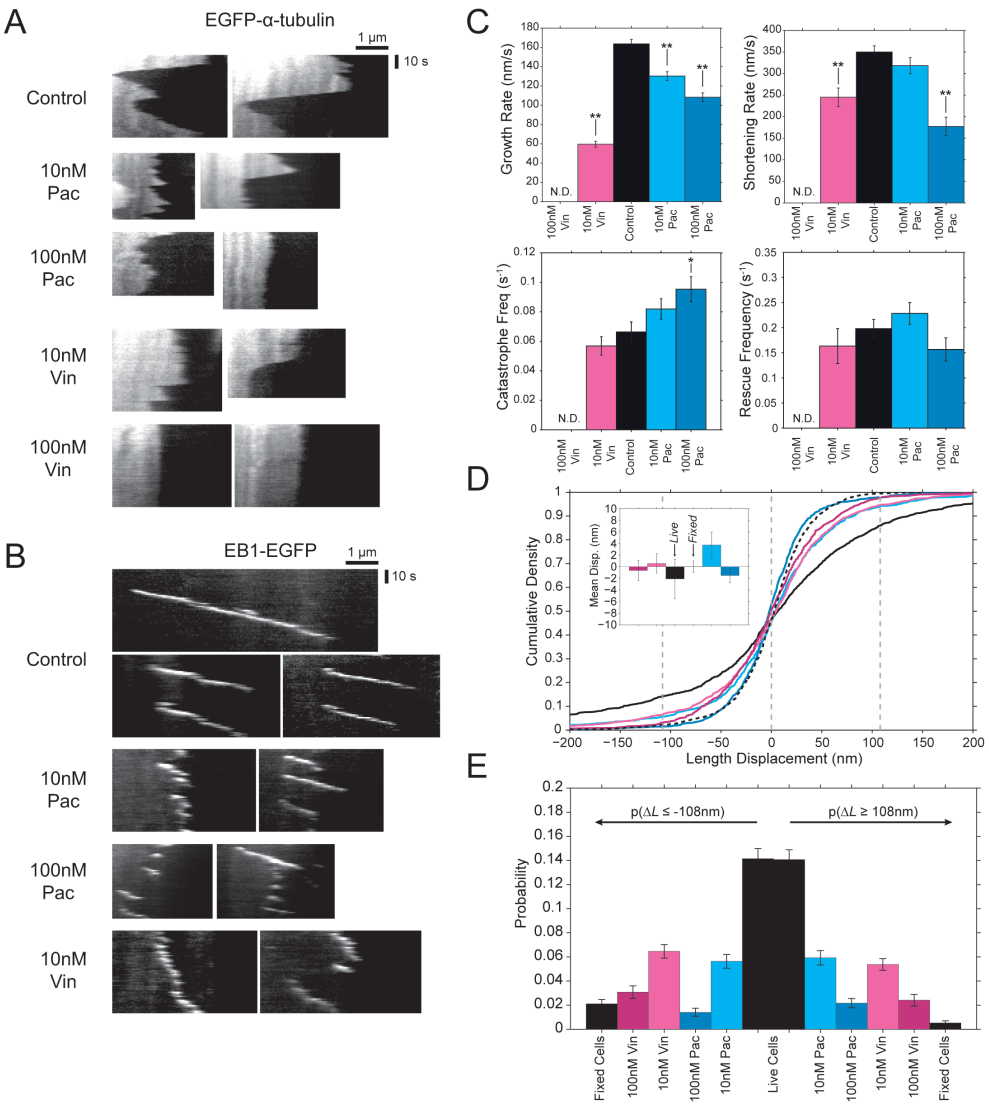

FIGURE 3.4 Microtubule-targeting agents induce new steady states with reduced microtubule dynamics in LLC-PK1 cells.
A-B) Representative kymographs of EGPF-α-tubulin (A) and EB1-EGFP (B) signal in LLC-PK1 cells treated with paclitaxel or vinblastine are shown. C) Estimated parameters of dynamic instability at 1s sample intervals (n>35 microtubules from >10 cells in each condition). N.D. = not determined due to the absence of detectable growth or shortening events. D) Microtubule length displacement cumulative distribution obtained by tracking EGFP-α-tubulin. Fixed cell displacements are indicated by the dotted line. Vertical dotted lines denote zero and the cutoff for the probability analysis in E. Inset shows the mean displacement for each condition. E) Probability of large displacements for each treatment condition. Large negative displacements are to the left of the control, while large positive displacements are to the right. In each plot, control values are shown in black, while paclitaxel and vinblastine are shown in cyan and magenta, respectively (light = 10nM and dark = 100nM). All error bars are ± SEM. * $p<0.05$, ** $p<0.01$ by multiple comparisons test.

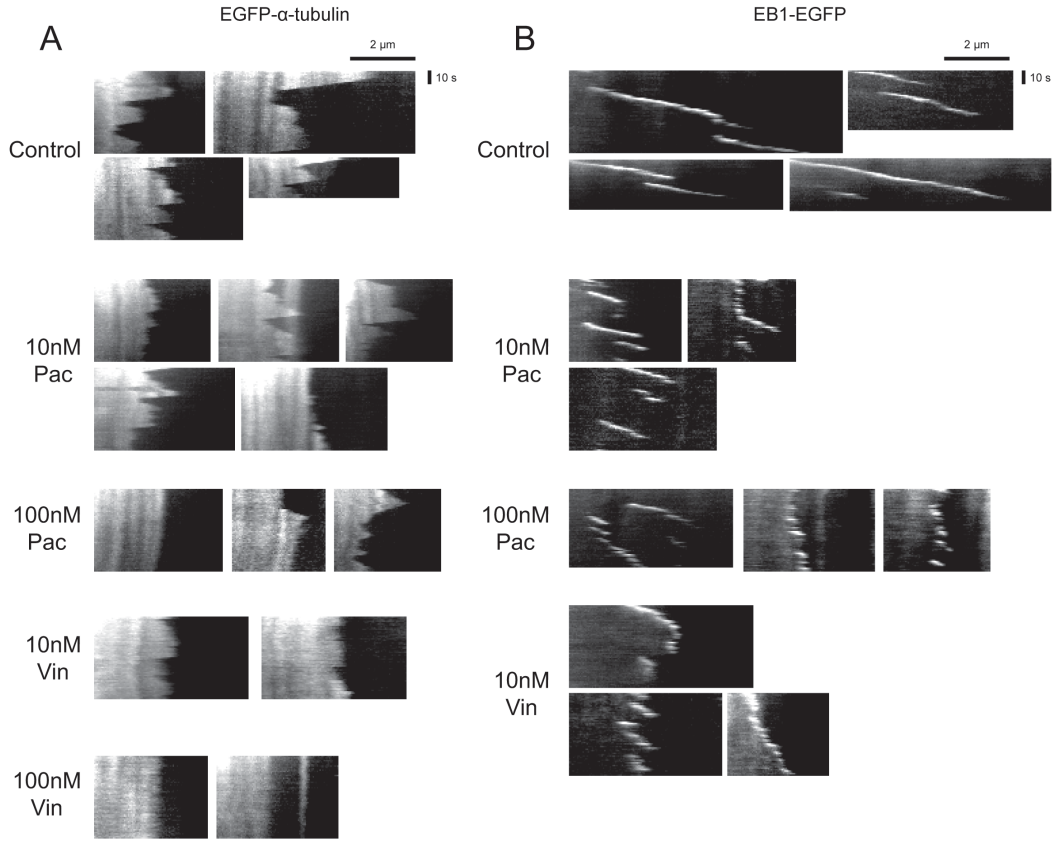

FIGURE 3.5 Microtubule dynamics are attenuated in the presence of paclitaxel and vinblastine

A) Example kymographs from LLC-PK1 cells stably expressing EGFP-α-tubulin. B) Example kymographs from LLC-PK1 cells stably expressing EB1-EGFP. Length and time scale bars apply to all included kymographs.

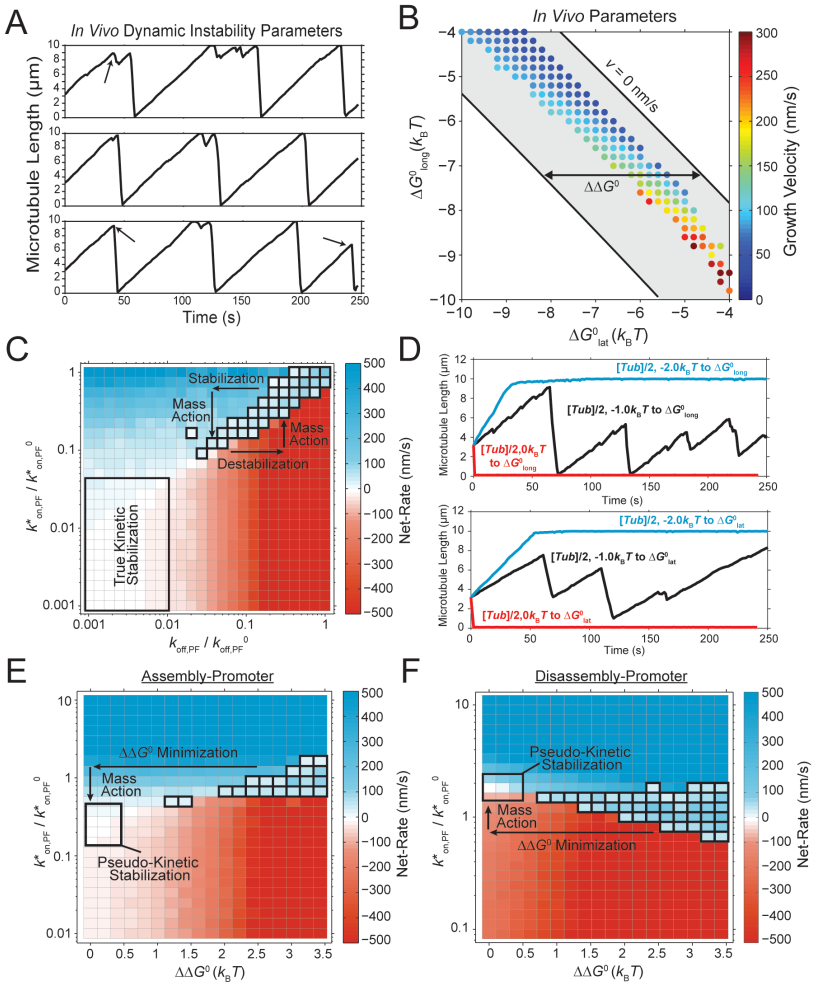

FIGURE 3.6 *In vivo* model makes similar predictions to the *in vitro* model with regards to dynamic instability and kinetic stabilization.
A) Representative microtubule length versus time traces for the *in vivo* dynamic instability parameters listed in Table 3.2. Arrows indicate points of catastrophe away from the cell edge. B) Colored dots indicate sample points where dynamic instability was observed with regards to the lateral and longitudinal bond free energy (ΔG^0_{lat} and ΔG^0_{long}, respectively). Color indicates the assembly rate during periods of growth. Shaded region is that constrained by the v = 0 nm/s contour and $\Delta\Delta G^0$. For each point, all parameters listed in Table 3.2 were held constant except the bond free energies. C) Bond stabilization of both GTP- and GDP-tubulin versus $k^*_{on,PF}$. D) Example length versus time plots for several points in the parameter space shown in C. In each case, [*Tub*] was decreased by twofold, while the longitudinal (top) or lateral (bottom) bond was stabilized by 0, -1, or -2k_BT. E) Decreasing energetic difference between GTP- and GDP-tubulin ($\Delta\Delta G^0$) versus the fold-change of $k^*_{on,PF}$ for an assembly-promoter. F) Decreasing energetic difference between GTP- and GDP-tubulin ($\Delta\Delta G^0$) versus the fold-change in $k^*_{on,PF}$ for a disassembly-promoter. In C-F, the bold boxes indicate points where dynamic instability was observed. The rate reported for points of dynamic instability is the average growth rate.

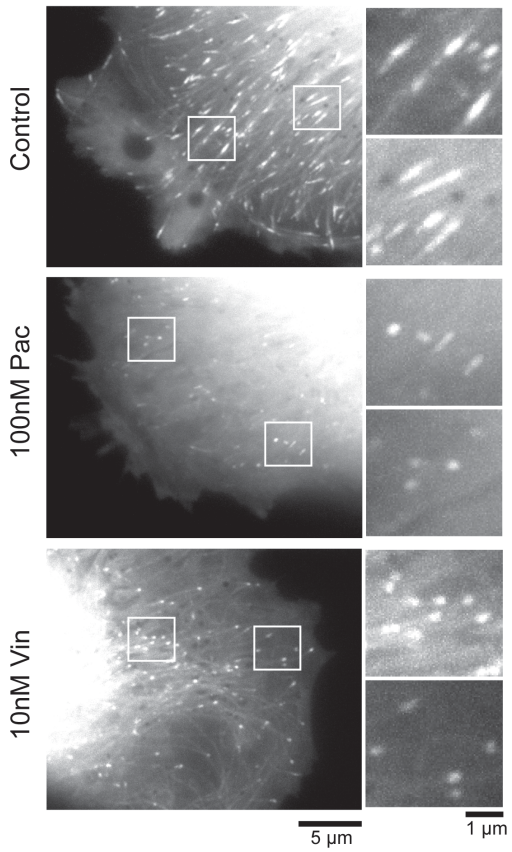

FIGURE 3.7 Microtubule-targeting agents do not affect the distribution of microtubule plus-ends in LLC-PK1 cells.
Maximum intensity projection of 20s time lapse of EB1-EGFP expressing LLC-PK1 cells treated with DMSO (control, top), 100nM paclitaxel (middle), and 10nM vinblastine (bottom). Regions within white squares are shown to the right. Scale bars of 5µm and 1µm apply to all conditions.

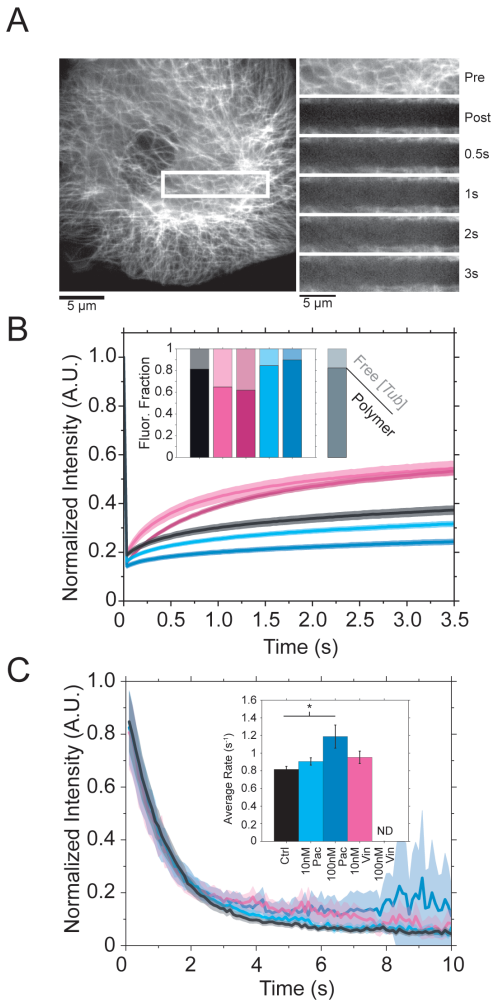

FIGURE 3.8 Estimation of free tubulin and hydrolysis effects in LLC-PK1 cells treated with paclitaxel and vinblastine.
A) An example control LLC-PK1 cell expressing EGFP-α-tubulin (LLC-PK1α) is shown. Regions containing both microtubule polymer and monomer (white box) were bleached and subsequently monitored for fast fluorescence recovery within the first 3s. The region within the white box is shown at multiple time points on the right. After 3s, no detectable polymer signal recovers. B) Fluorescence recovery curves for LLC-PK1α cells treated with paclitaxel (cyan; light = 10nM and dark = 100nM) and vinblastine (magenta; light = 10nM and dark = 100nM). Inset: fraction of fluorescence intensity contributed by polymer (bottom) and free tubulin (top). At least 12 FRAP events from individual cells were analyzed in each treatment condition. C) Decay of EB1-EGFP fluorescence along the microtubule lattice sampled at 100ms intervals (n>32 microtubules from >8 cells in each condition). Inset: best-fit exponential decay rate averaged across each cell for a given condition. Error bars are ± SEM. For each curve shown in B and C, the surrounding lighter area depicts the SEM of each time point. * $p<0.05$ by multiple comparisons test.

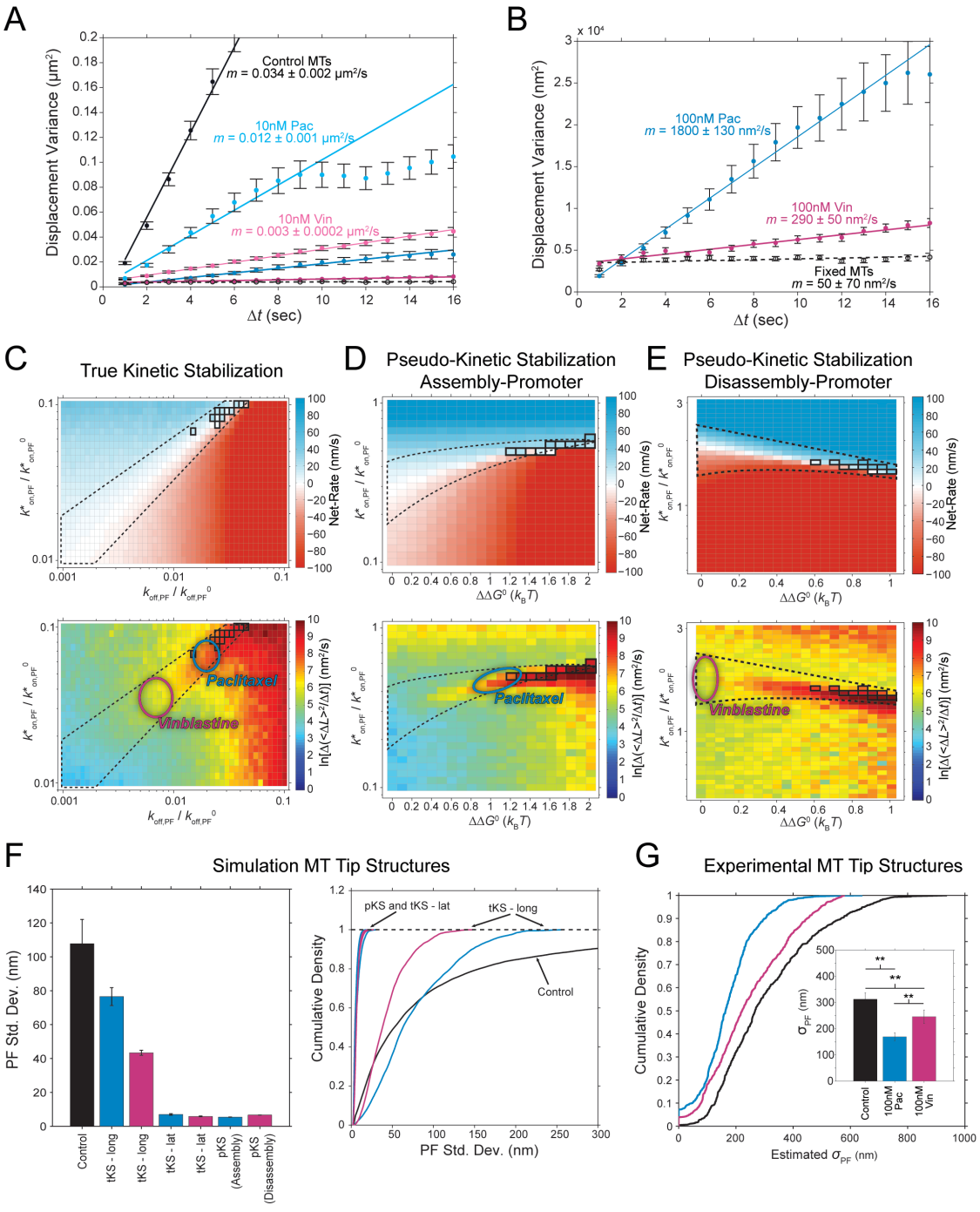
A
Displacement Variance (μm²)
Δt (sec)
Control MTs
m = 0.034 ± 0.002 μm²/s
10nM Pac
m = 0.012 ± 0.001 μm²/s
10nM Vin
m = 0.003 ± 0.0002 μm²/s
B
x 10⁴
Displacement Variance (nm²)
Δt (sec)
100nM Pac
m = 1800 ± 130 nm²/s
100nM Vin
m = 290 ± 50 nm²/s
Fixed MTs
m = 50 ± 70 nm²/s
C
True Kinetic Stabilization
D
Pseudo-Kinetic Stabilization
Assembly-Promoter
E
Pseudo-Kinetic Stabilization
Disassembly-Promoter
Net-Rate (nm/s)
Paclitaxel
Vinblastine
ΔΔG⁰ (k_BT)
F
Simulation MT Tip Structures
PF Std. Dev. (nm)
Control
tKS - long
tKS - lat
pKS (Assembly)
pKS (Disassembly)
pKS and tKS - lat
tKS - long
Control
Cumulative Density
G
Experimental MT Tip Structures
Estimated σ_PF (nm)
σ_PF (nm)
100nM Pac
100nM Vin

FIGURE 3.9 Microtubule assembly variance and tip structure in the presence of paclitaxel and vinblastine.
A-B) Variance of microtubule length displacements is plotted for increasing time intervals (Δt). Lines indicate the linear best fit to first 10s of data. Denoted linear slope for each treatment is the best fit ± 99% CI. Error bars for each point are SEM obtained by bootstrapping. C-E) Net-rate (top) of assembly as well as the average slope of linear best fit (bottom) to first 10s of simulated displacement variance versus time data is shown. The region defined by dotted black lines approximately indicates near zero net-rate for each case. The identical region is defined in the plot below. Ellipses indicate regions that are consistent with the experiment estimates of assembly variance in the presence of paclitaxel (cyan) or vinblastine (magenta) shown in B. F) Model predicted protofilament length standard deviation for each parameter set, averaged for ten separate microtubule trajectories (left) or cumulative for all microtubules (right). Control microtubules were simulated with the parameters listed in Table 3.2, while each kinetic stabilization case was sampled from the circled regions in C-E. tKS = true kinetic stabilization mechanism where the stabilization is applied either through the longitudinal (long) or lateral (lat) bond. pKS = pseudo-kinetic stabilization for an assembly- (D) or disassembly-promoter (E). G) Cumulative density of all experimentally estimated protofilament length standard deviations for control microtubules and in the presence of 100nM paclitaxel or 100nM vinblastine ($n>22$ microtubules from >10 cells in each condition). Inset: protofilament length standard deviation averaged across each microtubule. ** $p<0.01$ by multiple comparisons test. Error bars are ± SEM.

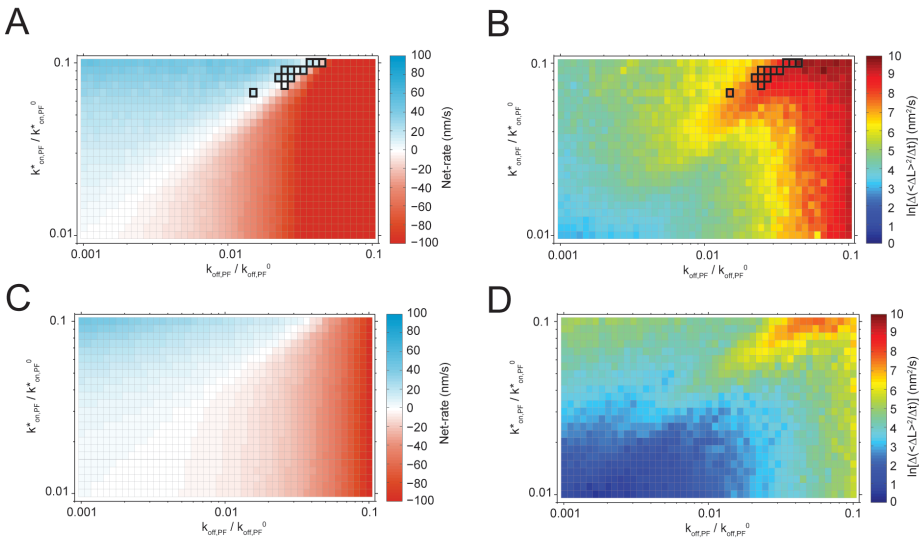

FIGURE 3.10 Simulation results of true kinetic stabilization are minimally affected by the implementation of the stabilizing effect.
A-B) Net-rate (A) and Assembly variance (B) as a function of varying $k^*_{on,PF}$ and $k_{off,PF}$ in the case where the stabilizing effect on $k_{off,PF}$ is implemented through the longitudinal bond. C-D) Net-rate (C) and Assembly variance (D) as a function of varying $k^*_{on,PF}$ and $k_{off,PF}$ in the case where the stabili0zing effect on $k_{off,PF}$ is implemented through the lateral bond.

CHAPTER 4

Summary and Conclusions

With the development of more advanced instrument capabilities as well as fluorescence imaging techniques the amount of quantitative data available in cell biology has become increasingly immense. The challenge for cell biologists is to use this information to extract meaningful conclusions about complex biological systems. Computational modeling provides a useful tool to integrate hypotheses and assumptions for the analysis and interpretation of experimental observations. The work presented in this dissertation utilizes the advantages of a computational approach for the study of microtubule self-assembly dynamics across multiple scales. This multiscale approach rigorously examines the theoretical processes underlying microtubule self-assembly from the submolecular scale of individual interdimer interactions, to the nanometer scale addition-loss of tubulin subunits, and finally to the microscale observation of microtubule dynamic instability.

In Chapter 2, a new computational model was developed for the association and dissociation of individual tubulin subunits, in which the individual interdimer interactions as well as the translational and rotational dynamics are simulated at the subnanometer length scale and picosecond timescale. This model represents the most detailed kinetic and thermodynamic model for tubulin-tubulin interactions at the microtubule plus-end to-date. Computational results reveal multiple aspects of microtubule assembly not previously appreciated. First, protofilaments of increased length, adjacent to tubulin binding sites, impose a steric penalty on subunit association, resulting in more than an order of magnitude effect in some cases. Therefore, the microscale microtubule on-rate constant should be considered an ensemble average of the nanometer scale on-rates of individual protofilaments that evolves in time. Second, this inhibition of subunit association influences the formation of tapered structures at the microtubule plus-end, consistent with those

observed experimentally. This suggests a feedback mechanism between subunit association and the formation of elongated end structures during assembly. Finally, perturbation of both the chemical or mechanical properties of the interdimer interactions has consequences for not only dissociation, but association of individual tubulin subunits as well.

The model described in Chapter 2 is the first, to our knowledge, to bridge the gap between molecular dynamics models and dimer-level stochastic models for self-assembly. Further, it is consistent with both experimental observations and theoretical predictions for microtubule self-assembly. Therefore, it serves as an ideal platform for future analysis of the actions of MAPs and microtubule-targeting agents that alter microscale assembly dynamics by altering the properties of interdimer interactions. In the future, it would also be interesting to apply the model in investigating the inherent differences between assembly dynamics at the minus-end versus the plus-end of the microtubule. Dynamics at the minus-end are diminished compared to the plus-end [44], yet it is not clear how interdimer interactions may differ from the plus-end. The orientation of subunits at the minus-end (α-tubulin facing out, compared to β-tubulin at the plus-end) obviates the potential for polymerization-driven hydrolysis, but it is not clear that this will result in the observed assembly differences. Assembly distinction is more likely due to a property of the subunit interactions, which could be revealed by the model.

In a year, more than 20% of all cancer patients receive chemotherapy as part of their treatment regimen. Several of the main and most successful chemotherapeutic drugs used clinically bind directly to αβ-tubulin heterodimers and inhibit microtubule self-assembly dynamics, promoting a "kinetically stable" state. Even with prominent clinical application, the mechanisms by which these microtubule-targeting agents induce "kinetic stabilization" have remained elusive. In Chapter 3, two stabilization mechanisms consistent with experimental evidence in the presence of the clinically relevant chemotherapeutic agents, paclitaxel and vinblastine, are described. The first mechanism is dependent on the combined

inhibition of association and dissociation of tubulin subunits. This mechanism is a "true kinetic stabilization" in which the kinetic rates are reduced by more than an order of magnitude. The second is a "pseudo-kinetic stabilization" that is the result of inducing an approximately single state polymer in the absence of significant kinetic inhibition. Additionally, the results in Chapter 3 indicate that uniform stabilization of the microtubule polymer is not consistent with experimental results and that rescue of dynamic instability *in vivo* is predicted for modest effects, an observation not previously appreciated. Further, computational results indicate that the observation of dynamic instability is constrained to a narrow region of parameter space. This is a surprising result considering not only the central importance of dynamic instability in many cellular processes but also the highly conserved nature of α- and β-tubulin.

In the future, the approach utilized in Chapter 3 could be used to investigate the mechanisms of additional microtubule-targeting agents, particularly those binding to the colchicine domain, which were not investigated in the work presented here. Mass action of tubulin dimers between polymer and solution is predicted to be an essential feature of the loss of dynamic instability by the pseudo-kinetic mechanism described. Therefore, iteratively comparing *in vitro* results, where the amount of tubulin in solution can be controlled, to *in vivo* results could provide an additive test to model predictions and further constrain the kinetic and thermodynamic effects of microtubule-targeting agents. As the model predicts that dynamic instability is constrained to a narrow region of parameter space, it is interesting to consider how MAPs evolved to enhance dynamic instability rather than resulting in a similar phenotype to microtubule-targeting agents. While already providing some insight, the model results and predictions described in Chapter 3 can be used as a framework for further analyzing the action of MAPs on assembly dynamics.

In conclusion, the work presented in this dissertation highlights the power of integrating computational models that are based on fundamental physical principles

with experimental observations in understanding complex biological systems. The insight gained in this study increases our knowledge of the biophysics of multistranded polymer self-assembly at multiple scales, using microtubules as a specific example. This work provides a framework for future analysis of microtubule dynamics and, ideally, will inform the development and screening of new and improved chemotherapeutic agents that bind to tubulin.

Appendices

Appendix A: Derivation of the model-predicted critical concentration

In order to derive the model-predicted critical concentration for net assembly, we started with the relationship described by equation 3.5. For a given ΔG^0_{tot} and $k_{\text{on,PF}}$, the value of $[Tub]$ where $v = 0$ is the critical concentration. Therefore, by rearrangement of equation 3.5 we can see

$$C_c \big/ C_c(0) = \exp\left([\Delta G^0_{tot} - \Delta G^0_{tot}(0)] / k_B T \right), \tag{A.1}$$

where (0) designates the reference energetic state. In this case $C_c(0) = 5.6\mu M$ for $\Delta G^0_{\text{tot}}(0) = -11.8 k_B T$ (black circle in Figure 3.1B). By rearrangement of equation A.1

$$\frac{C_c}{C_c(0)} = \frac{\exp\left(\Delta G^0_{tot} / k_B T \right)}{\exp\left(\Delta G^0_{tot}(0) / k_B T \right)}. \tag{A.2}$$

Thus, for each state with a given ΔG^0_{tot}

$$C_c = \exp\left(\Delta G^0_{tot} / k_B T \right). \tag{A.3}$$

By substituting in equation 3.1 and 3.2 we have

$$C_c = \exp\left(\Delta G^0_{tot} / k_B T \right) = \frac{k_{off,PF}}{k_{on,PF}} = K_D. \tag{A.4}$$

Appendix B: Expansion and optimization of *in vivo* microtubule tip tracking

Portions of this appendix are reprinted with permission from *Current Biology*: [42] and *Methods in Enzymology*: [52]
Contributing authors: Brian T. Castle, Louis S. Prahl, and David J. Odde

Introduction

With the development of more sensitive digital cameras and advanced image processing techniques, the classic definition of spatial resolution by optical approaches (Rayleigh criterion or the diffraction limit) no longer applies. This is most readily demonstrated by the development of recent "super-resolution" microscope systems in which image processing techniques are seamlessly integrated into the acquisition. Function fitting to digital image signal in particular can provide a simple way to obtain sub-pixel spatial information. Fitting accuracy will depend on several aspects of image acquisition, including the total magnification (spatial sampling) and signal-to-noise ratio, which should be considered, although, the optimization of some aspects may require tradeoff with others. Therefore, it is important to optimize the experimental setup in order to maximize the accuracy of image processing techniques including function fitting approaches. In this section we describe an improved method for semi-automated tracking of microtubule plu-end position during periods of growth, taking advantage the comparatively high signal level of EB1-EGFP compared to EGFP-α-tubulin. This procedure was implemented as an add-on option to the recently developed tip tracking algorithm software [51]. Additionally, we examine multiple experimental setup considerations in maximizing the accuracy of tracking microtubule tip position using the function fitting approach.

Expanding microtubule tip tracking algorithm for tracking EB1-EGFP signal

Microtubule tip tracking of EB1-EGFP signal was performed as described in Demchouk et al. [51], with a couple modifications to account for the EB1-EGFP signal as compared to EGFP-α-tubulin signal. First, to find the microtubule backbone, rather than designating the microtubule in each individual frame [51], all frames of EB1-EGFP movies were averaged together, such that comets appear as streaks or lines in the direction of microtubule growth (Figure B.1). Averaging across each frame is necessary to find the microtubule backbone in the EB1-EGFP movies due to the low labeling density of EB1 along the length of the microtubule away from the comet. Averaging across each frame also reduces the background noise due to freely diffusing EB1-EGFP in the cytoplasm, increasing the accuracy of fitting the microtubule backbone.

The user then clicks at the beginning and end of the streak to define the direction of growth, as well as the region within which the microtubule backbone is fit. The algorithm fits the microtubule backbone between the two user clicks by Gaussian fitting of transverse scans across the comet path (similar to [51]). These points (red line, inset Figure B.1A) are then used to fit a linear microtubule growth axis (blue line, inset Figure B.1A). Because the fit of the microtubule axis is from a composite of all frames in the movie, the same line is used to extract the EB1-EGFP fluorescence profile in every individual frame (Figure B.1A, right).

In [51], the fluorescence profile along the microtubule axis is extracted and fit by a Gaussian survival function, which determines the microtubule tip position in each frame. However, because EB1 labels only the tip of growing microtubules, the survival function is not a reliable fit to the EB1-EGFP fluorescence profile (green dots, Figure B.1B). Because we know that there is microtubule structure underlying the comet fluorescence decay, we can build that structure in the EB1-EGFP fluorescence profile by increasing the fluorescence intensity within the

comet, thus ensuring a more accurate and reliable fit of the Gaussian survival function. Therefore, in each frame, after the algorithm extracts the fluorescence profile along the microtubule growth axis (blue line, Figure B.1B), the maximum intensity from the EB1-EGFP fluorescence profile is assigned to each of the preceding points (towards the minus end) along the microtubule (red dots, Figure B.1B). As in described by Demchouk et al. [51], the mean of the Gaussian survival function is taken to be the microtubule tip position (cyan dot, Figure B.1B).

As seen in Figure B.1C, when the microtubule is growing (i.e. when a EB1-EGFP comet is detectable), the length versus time output is in good agreement with the corresponding kymograph. When the microtubule is shortening (EB1-EGFP comet disappears), length versus time output is very noisy, due to the noise of fitting maximum values of the low EB1-EGFP signal along microtubule lattice, and therefore has been omitted from the Figure B.1C. For applications where tracking the microtubule tip position during periods of shortening is not necessary, this loss of accuracy will not impact the analysis. Additionally, the presence of EB1-EGFP signal, or similarly the accuracy of tracking, can be used to distinguish periods of growth from shortening.

In order to obtain estimates of the EB1 tracking algorithm accuracy during periods of growth (high EB1-EGFP signal), we fixed LLCPK1 cells stably expressing EB1-EGFP by exposure to -20°C methanol for 10 minutes. As noted by Demchouk et al. [51], fixation of stably expressing cells resulted in ~2-fold loss of EGFP signal. Therefore, fixed cells were exposed for 2-fold longer than live cells in order to obtain similar image statistics (i.e. ratio of mean comet signal to cell background noise) between the two cases. In addition, imaged regions of fixed cells tend to bleach at a faster rate than live cells, likely due to the lack of rapid EB1-EGFP turnover at the microtubule tip. Therefore, only those frames maintaining comparable statistics to live cells were used for analysis of accuracy (50 frames for 200 ms exposure, 25 frames for 400 ms exposure).

For each fixed microtubule, the average tip position as determined by the EB1 tracking algorithm, was subtracted from the other tip positions to give delta tip (Δ_{tip}) for each time point. The standard deviation in Δ_{tip} for all microtubules (44 microtubules from 19 cells for 200 ms exposure, 44 microtubules from 17 cells for 400 ms exposure) was then calculated to estimate the single time point accuracy of EB1-EGFP tracking (Figure B.1D). For both acquisition settings, single time point accuracy was sub-pixel (Figure B.1D). This estimate of the single time point accuracy of EB1-EGFP tracking is 2- to 3-fold better than that estimated for EGFP-α-tubulin *in vivo* at similar exposures [51] and comparable to estimates for *in vitro* tubulin tracking [5]. Because EB1-EGFP more densely labels growing microtubule plus ends, as compared to EGFP-α-tubulin (50% for EB1 [106] versus 17% labeling density for α-tubulin [105]), more photons are collected on the detector per unit time, thus allowing for faster imaging frame rates while maintaining optimal signal-to-noise and spatial accuracy.

Optimizing experimental condition for microtubule tip tracking accuracy

Experimental Setup Considerations

Noise, background and signal intensity are all important considerations when obtaining quantitative measurements from digital fluorescence images, as they affect the accuracy and precision of these measurements [119]. In general, one would like to maximize signal while minimizing background and noise. This means that imaging parameters, such as exposure time, fluorophore brightness, and spatial sampling must be considered for each application. The optimization of some parameters requires a trade-off with others. For example, finer spatial sampling and/or increased temporal resolution reduce the signal intensity per pixel. Therefore, the optimal settings will depend on the individual application. To guide users in optimal code performance, tip tracking accuracy has been evaluated on simulated

images obtained by model convolution [51, 120] with an eye towards 1) signal intensity above background and 2) spatial sampling.

Signal Above Background

Fluorescence signal intensity is an important factor in determining tracking accuracy. Pixel intensity values along the microtubule are determined in part by the quantity of labeled tubulin subunits (labeling fraction). Figure B.2A shows that, for spatial sampling of 40 or 100 nm/pixel, as the labeled fraction of total tubulin in the microtubule lattice increases, resolution reaches a maximum (~50% labeling). In the LLC-PK1α cells we use, labeling fraction is fixed at ~17% [105], but *in vitro*, the labeling fraction is controllable. At low average signal above background, the noise is dominated by photon counting noise, yielding a less accurate measurement, while at higher values (>40 A.U. above background) the measurement reaches a maximal accuracy (Figure B.2B). This maximal accuracy is independent of spatial sampling for either pixel size evaluated (40 or 100 nm/pixel). These simulations were run on tapered tips comparable to those estimated *in vivo*, so the accuracy converges to ~36 nm, but blunt tips have higher accuracy, to ~15 nm [51]. On average, tips are more tapered *in vivo* compared to *in vitro* [5, 51], therefore we expect accuracy closer to 15 nm *in vitro*. For very low fraction labeled (less than 0.1), the cell is in the so-called "speckle" regime [121], which, while optimal for imaging microtubule transport, yields poor estimation of tip position. Figure B.2 plots were generated from running the tip tracking algorithm on simulated microtubule images obtained via model convolution, constructed using a 2 nm x 2 nm 'fine grid' and binned to appropriate pixel sizes [51, 120].

Spatial Sampling

Spatial sampling refers to the size of individual pixels that comprise a digital image, and is determined by the pixel size of the CCD camera and the magnification power of the optics. For example, our Nikon TE200 microscope is equipped with a

Photometrics CoolSnap HQ^2 CCD camera (6.45 μm/pixel) and 60x lens, giving spatial sampling of 105 nm/pixel, or 42 nm/pixel with an intermediate 2.5x projection lens (150x total magnification). Larger pixels may collect more photons and give higher signal, but smaller pixels contain more positional information and improve function fitting. Evaluating tip tracking accuracy on model convolved microtubule images over a range of spatial sampling (Figure B.2C), we show that tip tracking accuracy plateaus at ~36 nm for tapered tips for pixel sizes below ~100 nm/pixel. Tracking precision below this threshold is relatively insensitive to signal above background (20 or 40 A.U.). However, accuracy precipitously declines for spatial sampling greater than this value. The explanation lies in using a Gaussian to fit the imaging system PSF. With increasing pixel size, fewer pixels are available to fit σ_{PSF}, resulting in information loss about the microtubule tip position. In particular, around the so-called optical resolution of the system (defined by the Abbe diffraction limit, ~200-250 nm), the fit becomes unreliable, because essentially the entire PSF is contained in 1-2 pixels used to fit the 1D Gaussian (Figure B.2D). In general, when measuring features such as microtubule tips from digital images, larger pixels (at or near the diffraction limit) may contribute errors to function fits. Therefore, using a projection lens (or optovar) to reduce pixel size to less than 100 nm/pixel is recommended. Pixel binning (either pre-processing, or via the *bin* function) is a viable strategy to increase signal, so long as binned pixels stay below ~100 nm/pixel.

Optimization Using Fixed Cells

While model convolution (as employed above) provides a convenient way to test algorithm accuracy, it may be easiest to optimize the experimental setup for tracking accuracy on fixed cells using established protocols for tubulin fixation and immunostaining [39, 51, 122]. Since the tip position does not change between frames, deviations from the mean microtubule length (ΔLE) are due to experimental noise. Thus, the standard deviation of ΔLE (σ_{LE}) is an estimate of the tracking

accuracy. To demonstrate the effects of frame integration, we took 200 ms streaming videos of microtubules in the periphery of fixed LLC-PK1α cells (N = 54 microtubules) using our previously described microscope setup, integrated frames (1x, 2x and 3x frame integration, effective exposure times of 200, 400 and 600 ms), and measured deviations from the mean length (Figure B.3A). Frame integration effectively captures the expected effects of increasing frame exposure time and signal-to-noise. Increasing exposure time increases tracking accuracy, reducing the standard deviation of length elements (σ_{LE}). It is important to note that GFP brightness is reduced ~2x by cell fixation, therefore users should measure the loss for each specific application [51].

Pixel binning is commonly employed in digital image processing to boost signal by summing intensities for a region of several pixels into a single pixel, both during acquisition and as a post-processing technique. To estimate the effects of binning on tip tracking accuracy, we took the same fixed cell images and recorded ΔLE values for binned pixel sizes (1x1, 2x2 and 4x4 binning). Tip tracking accuracy decreased with higher binning (Figure B.3B), especially in the case of 4x4 binning for the previously described system (168 nm/pixel). Note that this spatial sampling is near the Rayleigh criterion for the system, where it was determined that the fit to σ_{PSF} breaks down (Figure B.2D), resulting in a less accurate estimate of tip position. As previously suggested, binning should be employed with caution, keeping pixels under ~100 nm to avoid contributing significant function fitting errors.

Tables and Figures

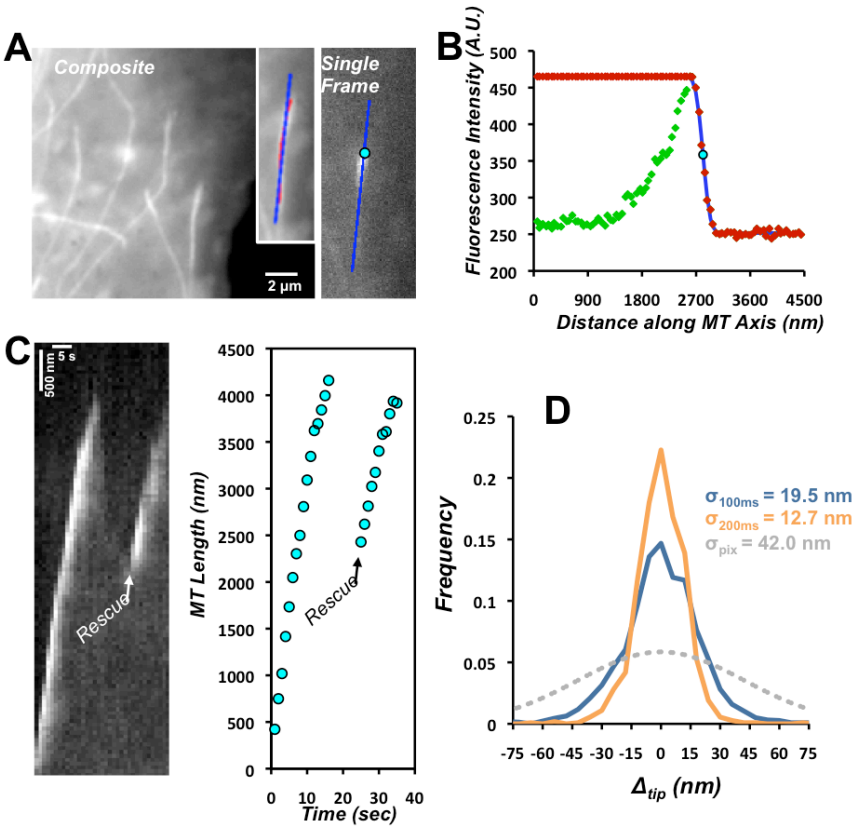

FIGURE B.1 Microtubule tip tracking using EB1-EGFP.
A) In order to fit the MT axis, all frames are averaged to create a composite image where comet paths appear as streaks. The fit of the composite MT axis (blue line, insert) is then used in each single frame (blue line, right) to extract the EB1 comet fluorescence profile. B) Example fluorescence profile along the MT axis shown in (A, right). The original fluorescence profile (green dots) is compared to the modified profile (red dots) where the maximum value is assigned to each preceding point (toward the minus end). Similar to Demchouk et al. (2011), a Gaussian survival function (blue line) is fit to the modified fluorescence profile and the MT tip position is determined by the mean (cyan dot) of the survival function. C) Kymograph (left) of the MT shown in A-B and the corresponding tip-tracking results (right). D) Deviations from the mean tip position (Δ_{tip}) determined by tracking cold-methanol-fixed EB1-EGFP comets for two different exposure times. Gray dotted line shows normal PDF with $\mu = 0$ nm and $\sigma = 42$ nm (equal to the final image pixel size). Single time point accuracy of EB1-EGFP tracking with 100-200 ms exposures is sub-pixel (10-20 nm) and improves with greater signal-to-noise (increased exposure times).

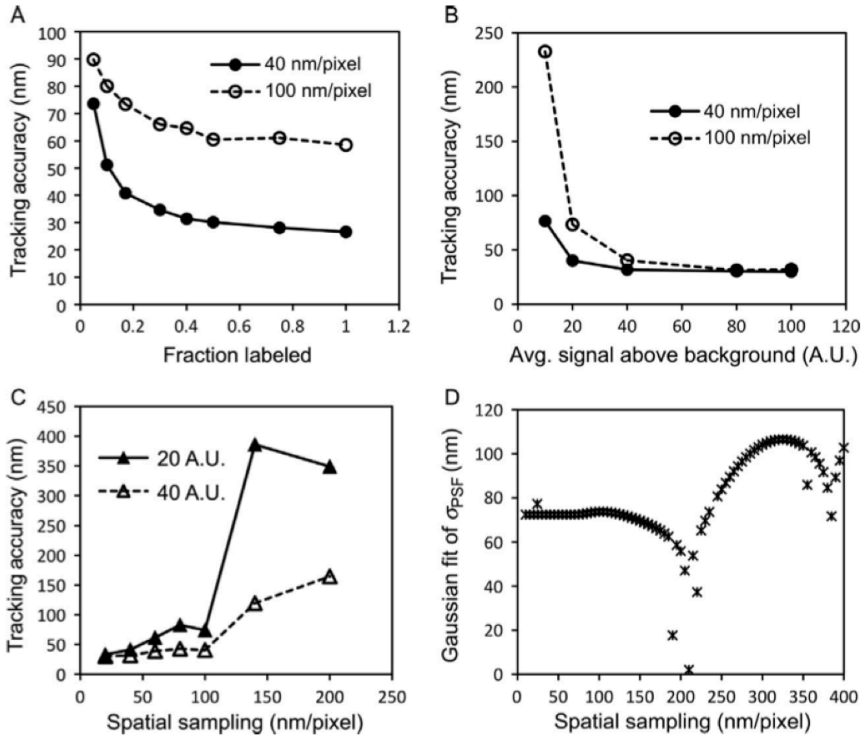

FIGURE B.2 Accuracy dependence on fluorescence signal and spatial sampling from analysis of model-convolved microtubule images.
A) Tip tracking accuracy (nm) plotted as a function of fraction labeled (percentage of labeled tubulin) and B) as a function of average signal counts above background (A.U.). Both fraction labeled and accuracy were evaluated at spatial sampling 40 and 100 nm/pixel. All points in A assume 20 A.U. above background. C) Accuracy plotted as a function of spatial sampling, for signal values of 20 and 40 A.U. above background. All points in B and C assume 20% tubulin labeling. D) Gaussian estimates of the point spread function standard deviation σ_{PSF} (nm) as a function of spatial sampling (at 40 A.U. above background).

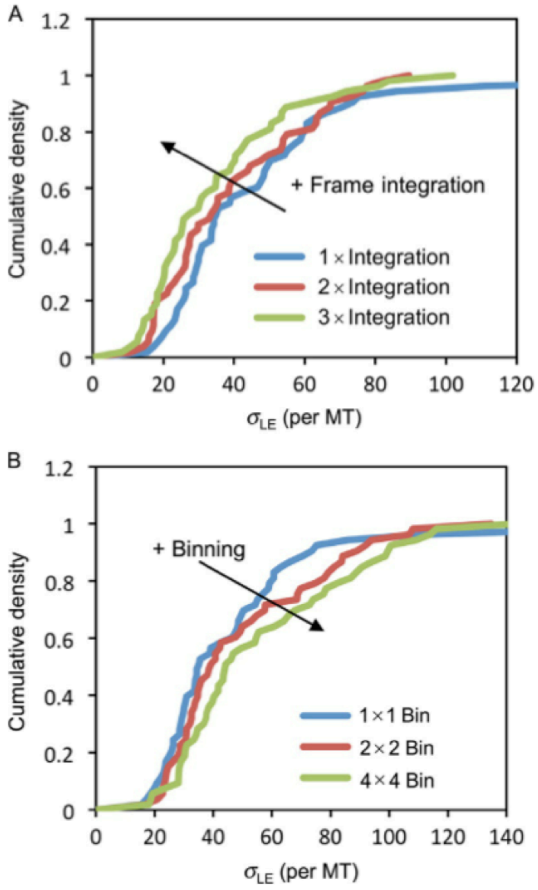

FIGURE B.3 Effects of binning and frame integration on tip tracking analysis on fixed cells *in vivo*.

Image stacks of fixed microtubules in the periphery of LLC-PK1α cells (n = 54 microtubules) were analyzed using the tip tracking algorithm. Images were acquired at 150x (42 nm/pixel) with 200 ms streaming acquisition. A) Effects of integrating multiple frames (1x, 2x and 3x integration, effective exposure times of 200, 400 and 600 ms) on standard deviation of length changes (σ_{LE}). B) Effects of increasing bin size (1x1, 2x2 and 4x4 binning, effective pixel sizes of 42, 84 and 168 nm/pixel) on σ_{LE}.

References

1. Mitchison, T., and M. Kirschner. 1984. Dynamic instability of microtubule growth. *Nature*. 312: 237–242.

2. Erickson, H.P., and E.T. O'Brien. 1992. Microtubule dynamic instability and GTP hydrolysis. *Annu. Rev. Biophys. Biomol. Struct.* 21: 145–66.

3. Desai, A., and T.J. Mitchison. 1997. Microtubule polymerization dynamics. *Annu. Rev. Cell Dev. Biol.* 13: 83–117.

4. Chrétien, D., S.D. Fuller, and E. Karsenti. 1995. Structure of growing microtubule ends: two-dimensional sheets close into tubes at variable rates. *J. Cell Biol.* 129: 1311–28.

5. Gardner, M.K., B.D. Charlebois, I.M. Jánosi, J. Howard, A.J. Hunt, and D.J. Odde. 2011. Rapid microtubule self-assembly kinetics. *Cell*. 146: 582–92.

6. Coombes, C.E., A. Yamamoto, M.R. Kenzie, D.J. Odde, and M.K. Gardner. 2013. Evolving Tip Structures Can Explain Age-Dependent Microtubule Catastrophe. *Curr. Biol.* 23: 1342–1348.

7. Gardner, M.K., M. Zanic, C. Gell, V. Bormuth, and J. Howard. 2011. Depolymerizing kinesins Kip3 and MCAK shape cellular microtubule architecture by differential control of catastrophe. *Cell*. 147: 1092–103.

8. Odde, D.J., L. Cassimeris, and H.M. Buettner. 1995. Kinetics of microtubule catastrophe assessed by probabilistic analysis. *Biophys. J.* 69: 796–802.

9. Mandelkow, E.M., E. Mandelkow, and R.A. Milligan. 1991. Microtubule dynamics and microtubule caps: a time-resolved cryo-electron microscopy study. *J. Cell Biol.* 114: 977–91.

10. Tran, P.T., P. Joshi, and E.D. Salmon. 1997. How tubulin subunits are lost from the shortening ends of microtubules. *J. Struct. Biol.* 118: 107–18.

11. Nogales, E., M. Whittaker, R.A. Milligan, and K.H. Downing. 1999. High-resolution model of the microtubule. *Cell*. 96: 79–88.

12. Löwe, J., H. Li, K.H. Downing, and E. Nogales. 2001. Refined structure of alpha beta-tubulin at 3.5 A resolution. *J. Mol. Biol.* 313: 1045–57.

13. Nogales, E., S.G. Wolf, and K.H. Downing. 1998. Structure of the alpha beta tubulin dimer by electron crystallography. *Nature*. 391: 199–203.

14. Howard, J., and A.A. Hyman. 2007. Microtubule polymerases and depolymerases. *Curr. Opin. Cell Biol.* 19: 31–5.

15. Brouhard, G.J., J.H. Stear, T.L. Noetzel, J. Al-Bassam, K. Kinoshita, S.C. Harrison, J. Howard, and A.A. Hyman. 2008. XMAP215 is a processive microtubule polymerase. *Cell*. 132: 79–88.

16. Zanic, M., P.O. Widlund, A.A. Hyman, and J. Howard. 2013. Synergy between XMAP215 and EB1 increases microtubule growth rates to physiological levels. *Nat. Cell Biol.* 15: 688–93.

17. Drechsel, D.N., A.A. Hyman, M.H. Cobb, and M.W. Kirschner. 1992. Modulation of the dynamic instability of tubulin assembly by the microtubule-associated protein tau. *Mol. Biol. Cell*. 3: 1141–54.

18. Dumontet, C., and M.A. Jordan. 2010. Microtubule-binding agents: a dynamic field of cancer therapeutics. *Nat. Rev. Drug Discov.* 9: 790–803.

19. Hellal, F., A. Hurtado, J. Ruschel, K.C. Flynn, C.J. Laskowski, M. Umlauf, L.C. Kapitein, D. Strikis, V. Lemmon, J. Bixby, C.C. Hoogenraad, and F. Bradke. 2011. Microtubule stabilization reduces scarring and causes axon regeneration after spinal cord injury. *Science*. 331: 928–31.

20. Sengottuvel, V., M. Leibinger, M. Pfreimer, A. Andreadaki, and D. Fischer. 2011. Taxol facilitates axon regeneration in the mature CNS. *J. Neurosci.* 31: 2688–99.

21. Ballatore, C., K.R. Brunden, D.M. Huryn, J.Q. Trojanowski, V.M.-Y. Lee, and A.B. Smith. 2012. Microtubule stabilizing agents as potential treatment for Alzheimer's disease and related neurodegenerative tauopathies. *J. Med. Chem.* 55: 8979–96.

22. Lee, J.J., and S.M. Swain. 2006. Peripheral neuropathy induced by microtubule-stabilizing agents. *J. Clin. Oncol.* 24: 1633–42.

23. Carlson, K., and A.J. Ocean. 2011. Peripheral neuropathy with microtubule-targeting agents: occurrence and management approach. *Clin. Breast Cancer*. 11: 73–81.

24. Markman, M. 2003. Managing taxane toxicities. *Support. Care Cancer*. 11: 144–7.

25. Dorléans, A., B. Gigant, R.B.G. Ravelli, P. Mailliet, V. Mikol, and M. Knossow. 2009. Variations in the colchicine-binding domain provide insight into the structural switch of tubulin. *Proc. Natl. Acad. Sci. U. S. A.* 106: 13775–9.

26. Gigant, B., C. Wang, R.B.G. Ravelli, F. Roussi, M.O. Steinmetz, P.A. Curmi, A. Sobel, and M. Knossow. 2005. Structural basis for the regulation of tubulin by vinblastine. *Nature*. 435: 519–22.

27. Li, H., D.J. DeRosier, W. V. Nicholson, E. Nogales, and K.H. Downing. 2002. Microtubule Structure at 8 Å Resolution. *Structure*. 10: 1317–1328.

28. Mitra, A., and D. Sept. 2008. Taxol allosterically alters the dynamics of the tubulin dimer and increases the flexibility of microtubules. *Biophys. J.* 95: 3252–8.

29. André, J.R., M.-J. Clément, E. Adjadj, F. Toma, P. a Curmi, and P. Manivet. 2012. The state of the guanosine nucleotide allosterically affects the interfaces of tubulin in protofilament. *J. Comput. Aided. Mol. Des.* 26: 397–407.

30. Sept, D., N. Baker, and J. McCammon. 2003. The physical basis of microtubule structure and stability. *Protein Sci.* : 2257–2261.

31. Grafmüller, A., E.G. Noya, and G.A. Voth. 2013. Nucleotide-dependent lateral and longitudinal interactions in microtubules. *J. Mol. Biol.* 425: 2232–46.

32. Wells, D.B., and A. Aksimentiev. 2010. Mechanical properties of a complete microtubule revealed through molecular dynamics simulation. *Biophys. J.* 99: 629–37.

33. VanBuren, V., D.J. Odde, and L. Cassimeris. 2002. Estimates of lateral and longitudinal bond energies within the microtubule lattice. *Proc. Natl. Acad. Sci. U. S. A.* 99: 6035–40.

34. VanBuren, V., L. Cassimeris, and D.J. Odde. 2005. Mechanochemical model of microtubule structure and self-assembly kinetics. *Biophys. J.* 89: 2911–26.

35. Margolin, G., I. V Gregoretti, T.M. Cickovski, C. Li, W. Shi, M.S. Alber, and H. V Goodson. 2012. The mechanisms of microtubule catastrophe and rescue: implications from analysis of a dimer-scale computational model. *Mol. Biol. Cell*. 23: 642–56.

36. Chen, Y.D., and T.L. Hill. 1985. Monte Carlo study of the GTP cap in a five-start helix model of a microtubule. *Proc. Natl. Acad. Sci. U. S. A.* 82: 1131–5.

37. Bayley, P., M. Schilstra, and S. Martin. 1989. A lateral cap model of microtubule dynamic instability. *FEBS Lett.* 259: 181–4.

38. Flyvbjerg, H., T. Holy, and S. Leibler. 1996. Microtubule dynamics: Caps, catastrophes, and coupled hydrolysis. *Phys. Rev. E*. 54: 5538–5560.

39. Seetapun, D., and D.J. Odde. 2010. Cell-length-dependent microtubule accumulation during polarization. *Curr. Biol.* 20: 979–88.

40. Gregoretti, I. V, G. Margolin, M.S. Alber, and H. V Goodson. 2006. Insights into cytoskeletal behavior from computational modeling of dynamic microtubules in a cell-like environment. *J. Cell Sci.* 119: 4781–8.

41. Schek, H.T., M.K. Gardner, J. Cheng, D.J. Odde, and A.J. Hunt. 2007. Microtubule assembly dynamics at the nanoscale. *Curr. Biol.* 17: 1445–55.

42. Seetapun, D., B.T. Castle, A.J. McIntyre, P.T. Tran, and D.J. Odde. 2012. Estimating the microtubule GTP cap size in vivo. *Curr. Biol.* 22: 1681–7.

43. Oosawa, F., and S. Asakura. 1975. Thermodynamics of the polymerization of protein. *New York*: *Academic Press*.

44. Walker, R.A., E.T. O'Brien, N.K. Pryer, M.F. Soboeiro, W.A. Voter, H.P. Erickson, and E.D. Salmon. 1988. Dynamic instability of individual microtubules analyzed by video light microscopy: rate constants and transition frequencies. *J. Cell Biol.* 107: 1437–48.

45. Hyman, A., S. Salser, D. Drechsel, N. Unwin, and T. Mitchison. 1992. Role of GTP hydrolysis in microtubule dynamics: information from a slowly hydrolyzable analogue, GMPCPP. *Mol. Biol. Cell*. 3: 1155–1167.

46. Gard, D.L., and M.W. Kirschner. 1987. A microtubule-associated protein from Xenopus eggs that specifically promotes assembly at the plus-end. *J. Cell Biol.* 105: 2203–15.

47. Cassimeris, L., N.K. Pryer, and E.D. Salmon. 1988. Real-time observations of microtubule dynamic instability in living cells. *J. Cell Biol.* 107: 2223–31.

48. Gildersleeve, R.F., A.R. Cross, K.E. Cullen, A.P. Fagen, and R.C.J. Williams. 1992. Microtubules grow and shorten at intrinsically variable rates. *J. Biol. Chem.* 267: 7995–8006.

49. Odde, D.J., H.M. Buettner, and L. Cassimeris. 1996. Spectral analysis of microtubule assembly dynamics. *AIChE J.* 42: 1434–1442.

50. Kerssemakers, J.W.J., E.L. Munteanu, L. Laan, T.L. Noetzel, M.E. Janson, and M. Dogterom. 2006. Assembly dynamics of microtubules at molecular resolution. *Nature*. 442: 709–12.

51. Demchouk, A.O., M.K. Gardner, and D.J. Odde. 2011. Microtubule Tip Tracking and Tip Structures at the Nanometer Scale Using Digital Fluorescence Microscopy. *Cell. Mol. Bioeng.* 4: 192–204.

52. Prahl, L.S., B.T. Castle, M.K. Gardner, and D.J. Odde. 2014. Quantitative analysis of microtubule self-assembly kinetics and tip structure. *Methods Enzymol.* 540: 35–52.

53. Pollard, T.D. 1986. Rate constants for the reactions of ATP- and ADP-actin with the ends of actin filaments. *J. Cell Biol.* 103: 2747–54.

54. Hill, T.L. 1986. Effect of fluctuating surface structure and free energy on the growth of linear tubular aggregates. *Biophys. J.* 49: 1017–31.

55. Northrup, S.H., and H.P. Erickson. 1992. Kinetics of protein-protein association explained by Brownian dynamics computer simulation. *Proc. Natl. Acad. Sci. U. S. A.* 89: 3338–42.

56. Metropolis, N., A.W. Rosenbluth, M.N. Rosenbluth, A.H. Teller, and E. Teller. 1953. Equation of State Calculations by Fast Computing Machines. *J. Chem. Phys.* 21: 1087.

57. Erickson, H.P., and D. Pantaloni. 1981. The role of subunit entropy in cooperative assembly. Nucleation of microtubules and other two-dimensional polymers. *Biophys. J.* 34: 293–309.

58. De La Cruz, E.M., J. Roland, B.R. McCullough, L. Blanchoin, and J.-L. Martiel. 2010. Origin of twist-bend coupling in actin filaments. *Biophys. J.* 99: 1852–60.

59. Fujii, T., A.H. Iwane, T. Yanagida, and K. Namba. 2010. Direct visualization of secondary structures of F-actin by electron cryomicroscopy. *Nature*. 467: 724–8.

60. Erickson, H.P. 1989. Co-operativity in protein-protein association. The structure and stability of the actin filament. *J. Mol. Biol.* 206: 465–74.

61. Doi, M., and S.F. Edwards. 1986. The Theory of Polymer Dynamics. *New York*: *Oxford University Press*.

62. Fernandes, M.X., and J.G. de la Torre. 2002. Brownian dynamics simulation of rigid particles of arbitrary shape in external fields. *Biophys. J.* 83: 3039–48.

63. Kikuchi, K., M. Yoshida, T. Maekawa, and H. Watanabe. 1991. Metropolis Monte Carlo method as a numerical technique to solve the Fokker—Planck equation. *Chem. Phys. Lett.* 185: 335–338.

64. Tiana, G., L. Sutto, and R.A. Broglia. 2007. Use of the Metropolis algorithm to simulate the dynamics of protein chains. *Phys. A Stat. Mech. its Appl.* 380: 241–249.

65. Andrews, S.S., and D. Bray. 2004. Stochastic simulation of chemical reactions with spatial resolution and single molecule detail. *Phys. Biol.* 1: 137–51.

66. Uhlenbeck, G., and L. Ornstein. 1930. On the Theory of the Brownian Motion. *Phys. Rev.* 36: 823–841.

67. Ermak, D., and J. McCammon. 1978. Brownian dynamics with hydrodynamic interactions. *J. Chem. Phys.* 69: 1352.

68. Horton, N., and M. Lewis. 1992. Calculation of the free energy of association for protein complexes. *Protein Sci.* 1: 169–81.

69. Howell, B., D.J. Odde, and L. Cassimeris. 1997. Kinase and phosphatase inhibitors cause rapid alterations in microtubule dynamic instability in living cells. *Cell Motil. Cytoskeleton*. 38: 201–14.

70. Brun, L., B. Rupp, J.J. Ward, and F. Nédélec. 2009. A theory of microtubule catastrophes and their regulation. *Proc. Natl. Acad. Sci. U. S. A.* 106: 21173–8.

71. Brenner, H. 1961. The slow motion of a sphere through a viscous fluid towards a plane surface. *Chem. Eng. Sci.* 16: 242–251.

72. Wolynes, P.G., and J.A. McCammon. 1977. Hydrodynamic Effect on the Coagulation of Porous Biopolymers. *Macromolecules*. 10: 86–87.

73. Wolynes, P.G. 1976. Slip boundary conditions and the hydrodynamic effect on diffusion controlled reactions. *J. Chem. Phys.* 65: 450.

74. Jencks, W. 1981. On the attribution and additivity of binding energies. *Proc. Natl. Acad. Sci. U. S. A.* 78: 4046–4050.

75. Howard, J. 2001. Mechanics of motor proteins and the cytoskeleton. *Sunderland, MA*: *Sinauer Associates*.

76. Dye, R.B., S.P. Fink, and R.C. Williams. 1993. Taxol-induced flexibility of microtubules and its reversal by MAP-2 and Tau. *J. Biol. Chem.* 268: 6847–50.

77. Felgner, H., R. Frank, and M. Schliwa. 1996. Flexural rigidity of microtubules measured with the use of optical tweezers. *J. Cell Sci.* 109 (Pt 2: 509–16.

78. Kurachi, M., M. Hoshi, and H. Tashiro. 1995. Buckling of a single microtubule by optical trapping forces: direct measurement of microtubule rigidity. *Cell Motil. Cytoskeleton*. 30: 221–8.

79. Venier, P., A.C. Maggs, M.F. Carlier, and D. Pantaloni. 1994. Analysis of microtubule rigidity using hydrodynamic flow and thermal fluctuations. *J. Biol. Chem.* 269: 13353–60.

80. Kawaguchi, K., and A. Yamaguchi. 2010. Temperature dependence rigidity of non-taxol stabilized single microtubules. *Biochem. Biophys. Res. Commun.* 402: 66–9.

81. Mickey, B., and J. Howard. 1995. Rigidity of microtubules is increased by stabilizing agents. *J. Cell Biol.* 130: 909–17.

82. Prota, A.E., K. Bargsten, D. Zurwerra, J.J. Field, J.F. Díaz, K.-H. Altmann, and M.O. Steinmetz. 2013. Molecular mechanism of action of microtubule-stabilizing anticancer agents. *Science (80-.).* 339: 587–90.

83. Needleman, D.J., M.A. Ojeda-Lopez, U. Raviv, K. Ewert, H.P. Miller, L. Wilson, and C.R. Safinya. 2005. Radial compression of microtubules and the mechanism of action of taxol and associated proteins. *Biophys. J.* 89: 3410–23.

84. Derry, W.B., L. Wilson, and M.A. Jordan. 1995. Substoichiometric binding of taxol suppresses microtubule dynamics. *Biochemistry*. 34: 2203–11.

85. Jordan, M.A., R.J. Toso, D. Thrower, and L. Wilson. 1993. Mechanism of mitotic block and inhibition of cell proliferation by taxol at low concentrations. *Proc. Natl. Acad. Sci. U. S. A.* 90: 9552–6.

86. Odde, D.J., and H.M. Buettner. 1998. Autocorrelation function and power spectrum of two-state random processes used in neurite guidance. *Biophys. J.* 75: 1189–96.

87. Kawaguchi, K., S. Ishiwata, and T. Yamashita. 2008. Temperature dependence of the flexural rigidity of single microtubules. *Biochem. Biophys. Res. Commun.* 366: 637–42.

88. Yu, D., V. Pessino, S. Kuei, and M.T. Valentine. 2013. Mechanical and functional properties of epothilone-stabilized microtubules. *Cytoskeleton (Hoboken)*. 70: 74–84.

89. Amos, L.A., and J. Löwe. 1999. How Taxol stabilises microtubule structure. *Chem. Biol.* 6: R65–9.

90. Castle, B.T., and D.J. Odde. 2013. Brownian dynamics of subunit addition-loss kinetics and thermodynamics in linear polymer self-assembly. *Biophys. J.* 105: 2528–40.

91. Alushin, G.M., G.C. Lander, E.H. Kellogg, R. Zhang, D. Baker, and E. Nogales. 2014. High-Resolution Microtubule Structures Reveal the Structural Transitions in αβ-Tubulin upon GTP Hydrolysis. *Cell*. 157: 1117–1129.

92. Elie-Caille, C., F. Severin, J. Helenius, J. Howard, D.J. Muller, and a a Hyman. 2007. Straight GDP-tubulin protofilaments form in the presence of taxol. *Curr. Biol.* 17: 1765–70.

93. Na, G.C., and S.N. Timasheff. 1980. Thermodynamic linkage between tubulin self-association and the binding of vinblastine. *Biochemistry*. 19: 1355–65.

94. Rendine, S., S. Pieraccini, and M. Sironi. 2010. Vinblastine perturbation of tubulin protofilament structure: a computational insight. *Phys. Chem. Chem. Phys.* 12: 15530–6.

95. Bayley, P., M. Schilstra, and S. Martin. 1990. Microtubule dynamic instability: numerical simulation of microtubule transition properties using a Lateral Cap model. *J. Cell Sci.* 95: 33–48.

96. Walker, R.A., N.K. Pryer, and E.D. Salmon. 1991. Dilution of individual microtubules observed in real time in vitro: evidence that cap size is small and independent of elongation rate. *J. Cell Biol.* 114: 73–81.

97. Voter, W.A., E.T. O'Brien, and H.P. Erickson. 1991. Dilution-induced disassembly of microtubules: relation to dynamic instability and the GTP cap. *Cell Motil. Cytoskeleton*. 18: 55–62.

98. Rice, L.M., E. a Montabana, and D. a Agard. 2008. The lattice as allosteric effector: structural studies of alphabeta- and gamma-tubulin clarify the role of GTP in microtubule assembly. *Proc. Natl. Acad. Sci. U. S. A.* 105: 5378–83.

99. Hunyadi, V., and I.M. Jánosi. 2007. Metastability of microtubules induced by competing internal forces. *Biophys. J.* 92: 3092–7.

100. Mitchison, T.J., and M.W. Kirschner. 1987. Some thoughts on the partitioning of tubulin between monomer and polymer under conditions of dynamic instability. *Cell Biophys.* 11: 35–55.

101. Mohan, R., E.A. Katrukha, H. Doodhi, I. Smal, E. Meijering, L.C. Kapitein, M.O. Steinmetz, and A. Akhmanova. 2013. End-binding proteins sensitize microtubules to the action of microtubule-targeting agents. *Proc. Natl. Acad. Sci. U. S. A.* 110: 8900–5.

102. Derry, W.B., L. Wilson, I.A. Khan, R.F. Luduena, and M.A. Jordan. 1997. Taxol differentially modulates the dynamics of microtubules assembled from unfractionated and purified beta-tubulin isotypes. *Biochemistry*. 36: 3554–62.

103. Panda, D., M.A. Jordan, K.C. Chu, and L. Wilson. 1996. Differential effects of vinblastine on polymerization and dynamics at opposite microtubule ends. *J. Biol. Chem.* 271: 29807–12.

104. Toso, R.J., M.A. Jordan, K.W. Farrell, B. Matsumoto, and L. Wilson. 1993. Kinetic stabilization of microtubule dynamic instability in vitro by vinblastine. *Biochemistry*. 32: 1285–93.

105. Rusan, N.M., C.J. Fagerstrom, a M. Yvon, and P. Wadsworth. 2001. Cell cycle-dependent changes in microtubule dynamics in living cells expressing green fluorescent protein-alpha tubulin. *Mol. Biol. Cell*. 12: 971–80.

106. Piehl, M., and L. Cassimeris. 2003. Organization and dynamics of growing microtubule plus ends during early mitosis. *Mol. Biol. Cell*. 14: 916–25.

107. Yvon, A.M., P. Wadsworth, and M.A. Jordan. 1999. Taxol suppresses dynamics of individual microtubules in living human tumor cells. *Mol. Biol. Cell*. 10: 947–59.

108. Dhamodharan, R., M.A. Jordan, D. Thrower, L. Wilson, and P. Wadsworth. 1995. Vinblastine suppresses dynamics of individual microtubules in living interphase cells. *Mol. Biol. Cell*. 6: 1215–29.

109. Kinoshita, K., I. Arnal, A. Desai, D.N. Drechsel, and A.A. Hyman. 2001. Reconstitution of physiological microtubule dynamics using purified components. *Science*. 294: 1340–3.

110. Komarova, Y.A., I.A. Vorobjev, and G.G. Borisy. 2002. Life cycle of MTs: persistent growth in the cell interior, asymmetric transition frequencies and effects of the cell boundary. *J. Cell Sci.* 115: 3527–39.

111. Diaz, J.F., and J.M. Andreu. 1993. Assembly of purified GDP-tubulin into microtubules induced by taxol and taxotere: Reversibility, ligand stoichiometry, and competition. *Biochemistry*. 32: 2747–2755.

112. Jordan, M.A., and L. Wilson. 1990. Kinetic analysis of tubulin exchange at microtubule ends at low vinblastine concentrations. *Biochemistry*. 29: 2730–9.

113. Gliksman, N.R., R. V Skibbens, and E.D. Salmon. 1993. How the transition frequencies of microtubule dynamic instability (nucleation, catastrophe, and rescue) regulate microtubule dynamics in interphase and mitosis: analysis using a Monte Carlo computer simulation. *Mol. Biol. Cell*. 4: 1035–50.

114. Zasadil, L.M., K.A. Andersen, D. Yeum, G.B. Rocque, L.G. Wilke, A.J. Tevaarwerk, R.T. Raines, M.E. Burkard, and B.A. Weaver. 2014. Cytotoxicity of paclitaxel in breast cancer is due to chromosome missegregation on multipolar spindles. *Sci. Transl. Med.* 6: 229ra43.

115. Wieczorek, M., S. Chaaban, and G.J. Brouhard. 2013. Macromolecular Crowding Pushes Catalyzed Microtubule Growth to Near the Theoretical Limit. *Cell. Mol. Bioeng.* 6: 383–392.

116. Bicek, A.D., E. Tüzel, A. Demtchouk, M. Uppalapati, W.O. Hancock, D.M. Kroll, and D.J. Odde. 2009. Anterograde microtubule transport drives microtubule bending in LLC-PK1 epithelial cells. *Mol. Biol. Cell*. 20: 2943–53.

117. Helenius, J., G. Brouhard, Y. Kalaidzidis, S. Diez, and J. Howard. 2006. The depolymerizing kinesin MCAK uses lattice diffusion to rapidly target microtubule ends. *Nature*. 441: 115–9.

118. Tinevez, J.-Y., U. Schulze, G. Salbreux, J. Roensch, J.-F. Joanny, and E. Paluch. 2009. Role of cortical tension in bleb growth. *Proc. Natl. Acad. Sci. U. S. A.* 106: 18581–6.

119. Waters, J.C. 2009. Accuracy and precision in quantitative fluorescence microscopy. *J. Cell Biol.* 185: 1135–48.

120. Gardner, M.K., B.L. Sprague, C.G. Pearson, B.D. Cosgrove, A.D. Bicek, K. Bloom, E.D. Salmon, and D.J. Odde. 2010. Model Convolution: A Computational Approach to Digital Image Interpretation. *Cell. Mol. Bioeng.* 3: 163–170.

121. Waterman-Storer, C.M., and E.D. Salmon. 1998. How microtubules get fluorescent speckles. *Biophys. J.* 75: 2059–69.

122. Witte, H., D. Neukirchen, and F. Bradke. 2008. Microtubule stabilization specifies initial neuronal polarization. *J. Cell Biol.* 180: 619–32.